Institut fur Geowissenschaften
Mathematisch-Naturwissenschaftliche Fakultät
Universität Potsdam

The South Chilean Subduction Zone between 41° and 43.5°S: Seismicity, Structure and State of Stress

Dissertation
zur Erlangung des akademischen Grades
Doktor der Naturwissenschaften (Dr. rer. nat.)
in der Wissenschaftsdisziplin Geophysik

eingereicht an der
Mathematisch-Naturwissenschaftlichen Fakultät
der Universität Potsdam

von
Dietrich Lange

Potsdam, Mai 2008

Abstract

While the northern and central part of the South American subduction zone has been intensively studied, the southern part has attracted less attention, which may be due to its difficult accessibility and lower seismic activity. However, the southern part exhibits strong seismic and tsunamogenic potential with the prominent example of the M_w=9.5 May 22, 1960 Valdivia earthquake. In this study data from an amphibious seismic array (Project TIPTEQ) is presented. The network reached from the trench to the active magmatic arc incorporating the Island of Chiloé and the north-south trending Liquiñe-Ofqui fault zone (LOFZ). 364 local events were observed in an 11-month period from November 2004 until October 2005. The observed seismicity allows to constrain for the first time the current state of stress of the subducting plate and magmatic arc, as well as the local seismic velocity structure.

The downgoing Benioff zone is readily identifiable as an eastward dipping plane with an inclination of $\sim$30°. Main seismic activity occurred predominantly in a belt parallel to the coast of Chiloé Island in a depth range of 12–30 km, which is presumably related to the plate interface. The down-dip termination of abundant intermediate depth seismicity at approximately 70 km depth seems to be related to the young age (and high temperature) of the oceanic plate. A high-quality subset of events was inverted for a 2-D velocity model. The v_p model resolves the sedimentary basins and the downgoing slab. Increased velocities below the longitudinal valley and the eastern part of Chiloé Island suggest the existence of a mantle bulge.

Apart from the events in the Benioff Zone, shallow crustal events were observed mainly in different clusters along the magmatic arc. These crustal clusters of seismicity are related to the LOFZ, as well as to the volcanoes Chaitén, Michinmahuida and Corcovado. Seismic activity up to a magnitude of 3.8 M_w reveals the recent activity of the fault zone. Focal mechanisms for the events along the LOFZ were calculated using a moment tensor inversion of amplitude spectra for body waves which mostly yield strike-slip mechanisms indicating a SW-NE striking of σ_1 for the LOFZ. Focal mechanism stress inversion indicates a strike-slip regime along the arc and a thrust regime in the Benioff zone. The observed deformation – which is also revealed by teleseismic observations – suggests a confirmation for the proposed northward movement of a forearc sliver acting as a detached continental micro-plate.

Zusammenfassung

Die stärksten Erdbeben treten an Subduktionszonen auf, so z.B. das stärkste instrumentell jemals gemessene Erdbeben vom 22. Mai 1960 mit einer Magnitude von 9,5 M_w in Süd Chile. In dieser Arbeit werden lokal gewonnene seismologische Daten aus dem zentralen Bereich des 1960er-Bebens vorgestellt. Das seismologische Netzwerk umfasste den chilenischen Forearc zwischen Tiefseegraben und den vulkanischen Bogen zwischen 41,5°–43,5°S und überdeckte sowohl die Insel Chiloé als auch die Nord-Süd-streichende Liquiñe-Ofqui Störungszone (LOFZ). Zwischen November 2004 und Oktober 2005 konnten 364 lokale Ereignisse registriert werden. Die gewonnen Aufzeichnungen erlauben Aussagen sowohl über das aktuelle Spannungsfeld im Forearc als auch über das lokale Geschwindigkeitsmodell und die Geometrie der subduzierten Benioff-Zone.

Mit einer Auswahl von P- und S-Laufzeiten von gut lokalisierbaren Erdbeben wurden ein Minimum 1-D Geschwindigkeitsmodell, Stationsresiduen und die Hypozentralparameter invertiert. Dieses Geschwindigkeitsmodell diente als Startmodell für die 2-D Tomographie. Das 2-D v_p-Modell zeigt eine Zone erhöhter Geschwindigkeiten unterhalb des Längstals und des östlichen Bereiches der Insel Chiloé, die als Mantelaufwölbung interpretiert werden kann. Die Benioff-Zone wird als eine mit ~30° ostwärts einfallende Struktur abgebildet. Die seismische Hauptaktivität findet parallel zur Küste der Insel Chiloé in Tiefen zwischen 12 und 30 km statt; es handelt sich um Beben, die wahrscheinlich auf der Plattengrenzfläche stattfinden. In Tiefen über 70 km lässt die Seismizität bereits stark nach, die tiefsten Beben wurden in 120 km Tiefe registriert. Die Abwesenheit tieferer Seismizität wird auf das junge Alter (und eine damit verbundene hohe Temperatur) der ozeanischen Platte zurückgeführt.

Neben der Seismizität in der Benioff-Zone treten flache, krustale Beben in verschiedenen Häufungen entlang des magmatischen Bogens auf. Diese Bereiche erhöhter Seismizität sind räumlich mit der LOFZ und den Vulkanen Chaitén, Michinmahuida und Corcovado verknüpft. Beben bis zu einer Magnitude von 3,8 M_w zeigen die gegenwärtige Aktivität der LOFZ. Herdflächen entlang der LOFZ wurden aus Momententensor-Inversion anhand von Amplitudenspektren von Raumwellen gewonnen. Ergebnisse einer Spannungsfeldinversion zeigen ein Blattverschiebungsregime für den magmatischen Bogen und ein Überschiebungsregime für Beben in der Benioff-Zone auf. Die hier gemachten seismologischen Beobachtungen, zusammen mit teleseismischen Erdbeben und geologischen Befunden, unterstützen die Modellvorstellung eines sich nordwärts bewegenden kontinentalen Forearc-Blocks für Süd Chile.

Resumen

A diferencia de los ampliamente estudiados sectores septentrional y central de la Zona de Subducción Chilena, la parte meridional ha recibido menos atención, posiblemente debido a su inaccesibilidad y a una menor actividad sísmica. Sin embargo, este sector meridional presenta un enorme potencial sismogénico y de generación de tsunamis, como lo confirma por ejemplo el terremoto M_w=9.5 de Valdivia en Mayo 22 de 1960. En este trabajo, se presentan datos de un red sísmica anfibia (Proyecto TIPTEQ), localizado entre la fosa y el arco magmático activo entre 41.5 y 43.5°S, incluyendo la Isla de Chiloé y, hacia el arco magmático, el sistema de fallas de Liquiñe-Ofqui (LOFZ). 364 eventos con magnitudes entre 0.5 y 5.1 fueron localizados en un periodo de 11 meses, desde Noviembre de 2004 hasta Octubre de 2005. El patrón de sismicidad observado permite por primera vez determinar el régimen actual de esfuerzos tanto en la placa subducente como en el arco magmático, así como establecer la estructura local de las velocidades sísmicas en esta región. Los datos obtenidos ilustran claramente la zona de Benioff como un plano con buzamiento entre 29° y 33° hacia el oriente. La principal actividad sísmica ocurre predominantemente a lo largo de un cinturón paralelo a la Isla de Chiloé, a una profundidad de entre 12 y 30 km, probablemente relacionada con el límite entre la placa oceánica y la corteza continental. A lo largo de esta zona, la desaparición de la abundante sismicidad de profundidad intermedia a una profundidad de 70 km parece estar relacionada con la edad juvenil y la alta temperatura de la placa oceánica. Una submuestra de eventos de alta calidad se invirtió para construir un modelo bidimensional de velocidades. El modelo resultante de la velocidad de ondas P (v_p) sugiere la existencia de un abombamiento del manto subyaciendo la parte oriental de la Isla de Chiloé. Además de los eventos observados en la Zona de Benioff, eventos corticales más someros fueron también localizados. Estos eventos se observaron principalmente agrupados en clusters a lo largo del arco magmático y están relacionados principalmente con el sistema de fallas de Liquiné-Ofqui (LOFZ) y los volcanes de Chaitén, Michinmahuida y Corcovado. La actividad sísmica con magnitudes de hasta 3.8 M_w refleja la actividad reciente del sistema de fallas. Solución de mecanismos focales para los eventos a lo largo de la LOFZ se calculó por medio de inversión del tensor del momento sísmico con espectro de amplitudes. Los resultados muestran mayormente mecanismos correspondientes a desplazamiento de rumbo, lo cual indica una dirección SW-NE para el esfuerzo principalmente el área de la LOFZ para esta latitud. Cálculo del régimen de esfuerzos mediante inversion de mecanismos focales indica la presencia de un régimen por desplazamiento a lo largo del rumbo en el arco magmático, y de un regimen de cabalgamiento en la Zona de Benioff. Se sugiere que la deformación observada en la LOFZ, combinada con observaciones telesísmicas confirma modelos tectónicos existentes que consideran al antearco como una mircoplaca independiente que se desplaza hacia el norte con respecto a la Placa Suramericana.

Contents

Chapter 1

Introduction

Most of the largest earthquakes that occur are generated at the plate interface in subduction zones (e. g. RUFF & KANAMORI, 1988). These large shallow earthquakes are related to the underthrusting of one lithospheric plate beneath another (OLESKEVICH et al., 1999), and have strong tsunamogenic potential (e. g. BILEK & LAY, 2002). More than 95% of the world-wide moment release is produced by shallow plate-boundary earthquakes (SCHOLZ, 2002). Due to this hazard potential the shallow structure of subduction zones is of particular scientific interest.

The western South American margin is an outstanding example of a large-scale ocean-continent collision zone (e. g. GANSSER, 1973, RAMOS & ALEMAN, 2000), which allows to study the mechanisms of earthquakes in a subduction zone. The oceanic Nazca plate subducts beneath the South American continent, beginning at the Chile Triple junction at 46°S and ending at the Cocos-Nazca spreading centre at ∼4°N. Several structural and physical parameters change over the ∼5400 km long, north-south trending margin and lead to a different geometry, behaviour and different coupling characteristics of the subduction zone.

While in the last decade the northern and central part of this subduction zone has been intensively studied, the southern part has attracted less attention, which may be due to its difficult accessibility and lower seismic background activity. However, the southern part exhibits strong seismic and tsunamogenic potential (e. g. CIFUENTES & SILVER, 1989, CISTERNAS et al., 2005) with the M_w=9.5 May 22, 1960 Valdivia earthquake being the prominent example (PLAFKER & SAVAGE, 1970). This earthquake sequence released a quarter of the worldwide seismic energy in the last century (SCHOLZ, 2002). The rupture length of this earthquake was approximately 900 km (BARRIENTOS & WARD, 1990), starting at 38.2°S and ending at 46.5°S, where the active Chile Rise is currently subducting beneath the South American plate (e. g. HERRON et al., 1981, MURDIE et al., 1993, LAGABRIELLE et al., 2004).

The nucleation area of the 1960 Valdivia earthquake (∼38.2°S) has recently been studied

by using local seismicity data (BOHM et al., 2002, RIETBROCK et al., 2005, HABERLAND et al., 2006) and seismic refraction and refraction profiles (LÜTH et al., 2003, KRAWCZYK et al., 2003, 2006, SCHERWATH et al., 2006, GROSS et al., 2007). However, little or nothing was known about the microseismicity and deeper structure of the forearc farther to the South. In this study new data from an amphibious seismic array is presented, located between 41.5–43.5°S, reaching from the trench to the active magmatic arc incorporating the Island of Chiloé (Figure 1.1). The observed seismicity allows us to constrain the geometry and state of stress of the subducting Nazca plate, as well as seismogenic processes in the central part of the rupture area of the 1960 Valdivia earthquake. In the study area the age of the presently subducting Nazca plate is 18 Ma (MÜLLER et al., 1997). The subducting Nazca plate in the study area is young, hot and buoyant close to the Chile Triple junction, thus it was assumed to possibly subduct at low angles.

The tectonic setting and seismicity of the southern Andes is described in section 2. The data acquisition and preprocessing, including event detection and arrival time determination, is described in Chapter 3. Using the data from this network, for the first time local seismicity is presented, which reveals the structure and geometry of the forearc in southern Chile (section 5.3). The distribution (depth and frequency) of seismicity is discussed with regard to the controlling parameters (age and therefore density of incoming crust). Additionally, the relations of the results with subduction zone models and the concept of the seismogenic zone is discussed in section 7.2. The seismicity distribution and the 1-D minimum velocity model were published in Geophysical Research Letters (LANGE et al., 2007).

A high-quality subset of arrival time onsets were inverted with local earthquake tomography (THURBER, 1983) for 2-D velocity models (section 5.4). The v_p model reveals further structural information of the subsurface suggesting the depth-location of the continental mantle and showing the shallow sedimentary basins. The 2-D velocity model and accurate hypocentre locations, along with focal mechanisms of first-motion polarities (section 6.2), result in an integrated picture of the Benioff zone for the subduction zone segment under investigation.

Large mega-earthquakes seem to be regularly related to strike-slip faults, which are situated in the volcanic arc due to partitioning of stress/strain of the incoming plate. The strongest three earthquakes during the last century all possess a prominent strike-slip fault in the magmatic arc, e. g. Chile 1960 (M_w=9.5) (PLAFKER & SAVAGE, 1970), Alaska 1964 (M_w=9.2) (PLAFKER, 1972) and Northern Sumatra 2004 (M_w=9.1) (MCCAFFREY et al., 2000). Apart from seismicity related to the slab, crustal seismicity is found below the magmatic arc where the continental part of the study area is crossed by the 1000 km long north-south trending Liquiñe-Ofqui fault zone (LOFZ) which is a transpressional dextral intra-arc shear zone (CEMBRANO et al., 2002). Structural data documents that the
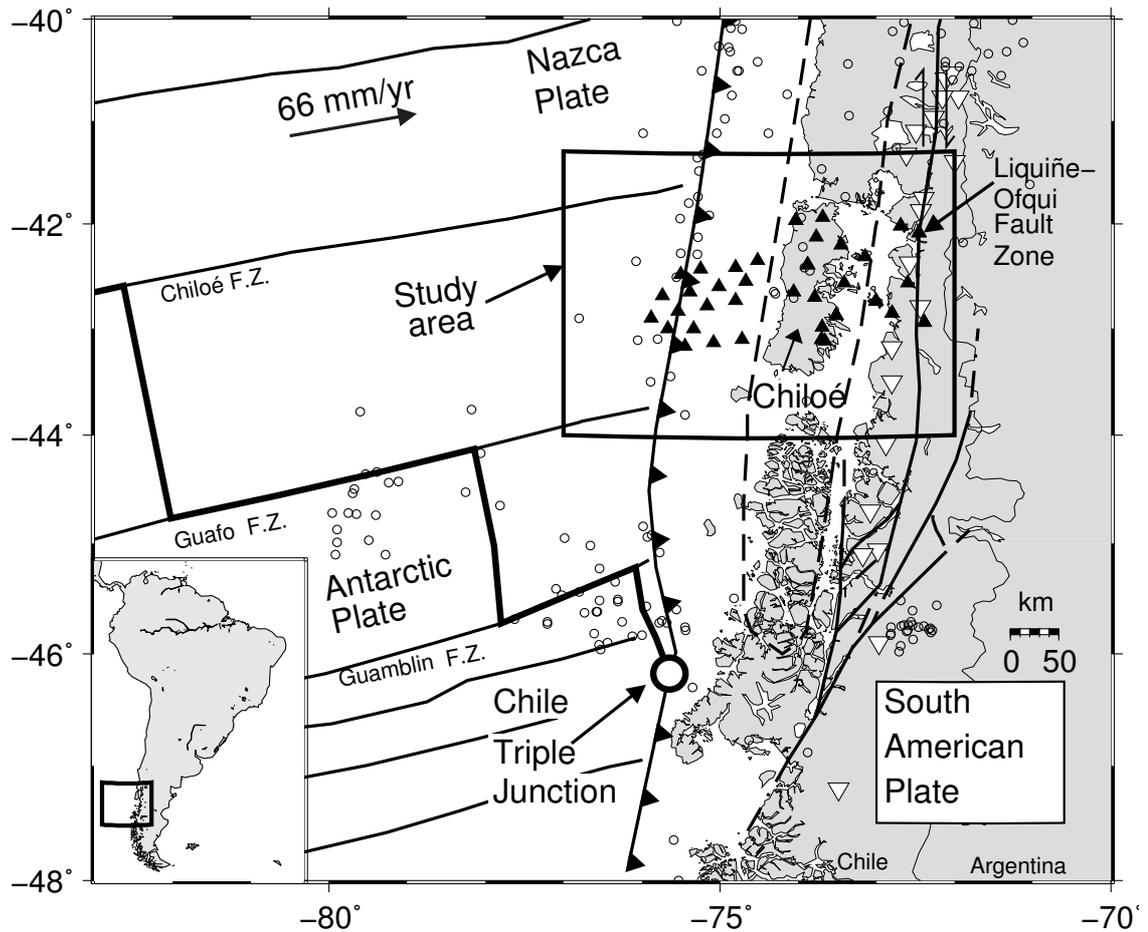
Figure 1.1: Tectonic map of the southeast Pacific and southern Chile close to the Chile triple junction, modified after THOMSON (2002) and LANGE et al. (2007). Seismic stations and earthquake locations from the NEIC-PDE Catalogue (1990–2006) are indicated by black triangles and open circles, respectively. The dashed line indicates the extent of subsidence associated with the 1960 Chile earthquake according to PLAFKER & SAVAGE (1970). Volcanoes are indicated by inverted white triangles. The Nazca–South American plate convergence rate is shown after ANGERMANN et al. (1999).

LOFZ (Figure 1.1) in the Patagonian Cordillera has accommodated concomitant strike-slip, oblique-slip and reverse-slip ductile to brittle deformation over the last 6 Ma (HERVÉ et al., 1994, LAVENU & CEMBRANO, 1999). However, the current deformation state of the arc and the fault zone is still poorly known because of the lack of systematic seismic studies in this remote area of the Andes. In order to obtain focal mechanisms, moment tensor inversion of amplitude spectra for body waves was carried out (DAHM et al., 1999, CESCA et al., 2006). The crustal hypocentres are presented along with the focal mechanisms in section 6.1, where for the first time substantial shallow seismicity along a 130 km long segment the Liquiñe-Ofqui fault zone (LOFZ) is presented. I show in this work the detailed relation of the measured seismicity to the LOFZ, active volcanoes and secondary faults. Furthermore, the findings are complemented by the background seismicity and previously published long-term structural measurements (CEMBRANO et al., 2000). The focal mechanisms help to constrain the current stress field along the Liquiñe-Ofqui fault zone. The model invoked in the explanation of this seismicity is similar to FITCH's (1972) explanation for the Sumatra fault. Part of this work covering the seismicity and state of stress along the LOFZ was published in Tectonophysics (LANGE et al., 2008).

Chapter 2

Tectonic Setting and Seismicity of the Southern Andes

2.1 Tectonic Setting of the Andes

Subduction of oceanic crust below continental lithosphere along the South American margin since the Mesozoic (CORVALÁN, 1990) formed a mountain belt with active volcanism and high mountain ranges rising up to 6900 m (DEWEY & LAMB, 1992). The Nazca plate is actively subducting beneath South America along much of the length of the Andes (Figure 2.1). South of the Chile triple junction the Antarctic plate is subducting beneath South America (HERRON et al., 1981, CANDE & LESLIE, 1986). The southern Chilean Andes provide a natural laboratory for examining the nature of long-term and short-term transpressional deformation across an obliquely convergent continental margin because of its very well-constrained plate kinematic history (TEBBENS & CANDE, 1997). This shows steady right-lateral oblique subduction of the Nazca plate beneath South America since 48 Ma with the exception of nearly orthogonal convergence between 26 to 20 Ma (PARDO-CASAS & MOLNAR, 1987, SOMOZA, 1998). At present, the angle of obliquity of the Nazca-South America plate convergence vector, with respect to the trench normal is 18° for southern Chile (ANGERMANN et al., 1999, HOFFMANN-ROTHE et al., 2006).

The along-strike structure of the Andes shows extraordinary variations, e. g. the highest topography elevations are found in the central Andes with 6900 m (JAILLARD et al., 2000), while the highest volcanoes in the southern Andes are less than 2400 m (Figure 2.2(a)). Hence, several authors have drawn their attention to the segmented character of the Andes as a whole (e.g. GANSSER, 1973, BARAZANGI & ISACKS, 1976, TASSARA et al., 2006, HACKNEY et al., 2006). DEWEY & LAMB (1992) described segments based on active deformation, MPODOZIS & RAMOS (1990) investigate the tectonic evolution of the orogen, and LÓPEZ-ESCOBAR et al. (1993, 1995), as well as NARANJO & STERN
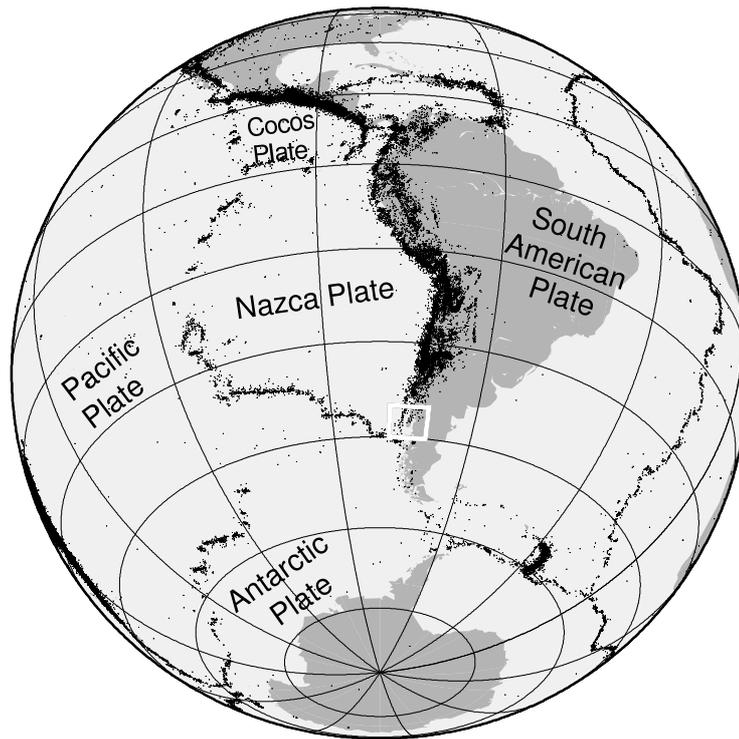
Figure 2.1: Plate-tectonic setting of the South American continent. The background seismicity (NEIC catalogue, 1973–2007, $M \geq 4$) reveals the plate boundaries. The location of the study area is outlined by a white rectangle.

(2004) classify the margin by using distinctive Quaternary provinces. BARAZANGI & ISACKS (1976) segmented the Andes by using the distribution of seismicity in the subducting Nazca plate and distinguished segments based on alternating flat and steep subduction style, which correlate well with the existence of Quaternary volcanism along the magmatic arc (Figure 2.2(c)). The area under investigation belongs to the "southern Chile segment" (BARAZANGI & ISACKS, 1976).

2.2 Benioff Zone Seismicity of the Southern Andes

While velocity and obliquity are relatively stable from north to south, the age (and therefore temperature and density) of the subducting Nazca plate decreases drastically from 45 Ma at 20°S to virtually 0 Ma at 46°S (Figure 2.2(b)), where the Chile Rise is currently subducting. Frequency and magnitudes of events along the South American margin listed in the NEIC-PDE catalogue decrease substantially in direction toward the triple junction (Figure 2.3). Earthquakes listed in the teleseismic catalogues (WWW-PDE, 2007, WWWCMT, 2007) at latitudes south of 38°S are rarely deeper than 100 km. The region between Chiloé Island and the triple junction is characterised by a virtual absence of teleseismically observed seismicity (Figure 2.3). Due to the lack of local networks and a low level of seismicity, inclination and structure of the subducted slab south of 39°S has remained so far unknown. Lower background seismicity and a successive decreasing of the maximal depths of seismicity (Figure 2.2(c)) in direction toward the triple junction (in southern Chile) are ascribed to the successive subduction of younger oceanic plate age

Figure 2.2: Overview plots of the central and southern Andes between 7°S and 53°S with seafloor ages (MÜLLER et al., 1997), contours of the top of the subducted slab of the Nazca plate according to GUDMUNDSSON & SAMBRIDGE (1998), topography and bathymetry after WWW-NGDC (2007), seismicity after WWW-PDE (2007). The black box indicates the location of the seismic network. Velocity of the Nazca plate after ANGERMANN et al. (1999). Volcanoes plotted as upright red triangles (SIEBERT & SIMKIN, 2002).
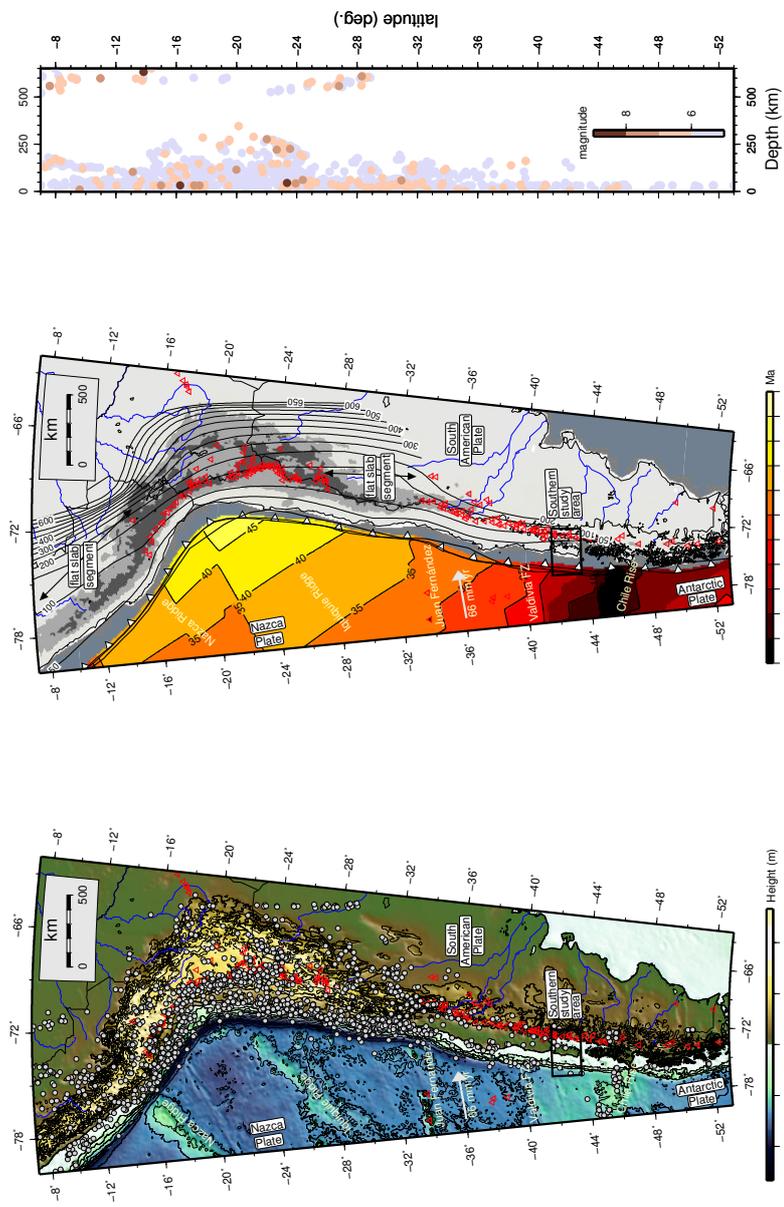
(a) Topography and bathymetry of the central and southern Andes from WWW-NGDC (2007). Earthquake locations from the NEIC catalogue (1973–2007, $M \geq 5$) are indicated by grey circles.

(b) Seafloor ages (MÜLLER et al., 1997) with oceanic features and contours indicating the top of the subducted slab of the Nazca plate (GUDMUNDSSON & SAMBRIDGE, 1998). Areas with low inclination of the Benioff zone ("flat slab" segments) correlated with missing volcanism in the magmatic arc (BARAZANGI & ISACKS, 1976).

(c) North-south depth distribution of Nazca plate seismicity. (NEIC catalogue, 1973–2007, $M \geq 5$)

and therefore higher heat flow towards the south (KIRBY et al., 1996). The southernmost local network was deployed by MURDIE et al. (1993) in the forearc near the subducted Chile Rise spreading centre at the Taitao Peninsula, where mainly very shallow seismicity was reported.

In contrast to the low level of seismicity in the PDE catalogue, southern Chile was affected by the largest earthquake instrumentally recorded (e. g. TILLOTSON, 1962, CIFUENTES, 1989, CISTERNAS et al., 2005). The southern Chilean (Valdivia) earthquake of May, 22 1960 (19:11 UTC) caused around 3.000 deaths in southern Chile (LOMNITZ, 2004). The mainshock was preceded by a series of foreshocks that started on May, 21 1960 with an M_w 8.1 event (CIFUENTES, 1989). The foreshocks and the initiation of the 1960 main shock occurred within the rupture area of the first event in the foreshock sequence. Fifteen minutes before the mainshock, there was another event of magnitude 7.9 (CIFUENTES, 1989). The M_w 9.5 mainshock (CIFUENTES & SILVER, 1989) initiated at the Arauco peninsula at 38.2°S and progressed 900 km southwards until the rupture terminated near the intersection of the Chile Rise with the Chilean trench near 46.5°S. This north-south trending rupture produced remarkable changes in land levels (PLAFKER & SAVAGE, 1970). Extreme coseismic changes ranging from 5.70 m of uplift at Guamblín Island to 2.7 m of subsidence at Valdivia were observed (BARRIENTOS et al., 1992). The southern Chilean margin was uplifted in the offshore area while subsiding onshore. The ensuing tsunami affected southern Chile, Hawaii, Japan, the Philippines, eastern New Zealand and the Aleutian Islands in Alaska, causing damage in all these places. The tsunami waves were up to 10–15 m high in Chile, maximum heights of 10 m in Hawaii and 6 m in Japan were reported (CISTERNAS et al., 2005). Estimates for the width of the rupture plane of the 1960 earthquake range between 125 and 150 km (BARRIENTOS & WARD, 1990, PLAFKER & SAVAGE, 1970). Slip inversion of the land-level changes inferred to have accompanied the mainshock (PLAFKER & SAVAGE, 1970) estimate either a uniform slip of 17 m on a 850 km long and 130 km wide fault, or variable slip up to 40 m (BARRIENTOS & WARD, 1990). The working area is located midway along the 1960 rupture of the Valdivia earthquake and is shown in Figure 2.3 together with the subsided area of the 1960 earthquake.

Recently, the nucleation area (Arauco Peninsula ∼38.2°S) of the 1960 earthquake has been studied by using local seismicity data (BOHM et al., 2002, RIETBROCK et al., 2005, HABERLAND et al., 2006) and seismic reflection and refraction profiles (LÜTH et al., 2003, KRAWCZYK et al., 2003, 2006, GROSS et al., 2007). The oceanic plate subducts with an angle of 30° under the continental plate and seismicity can be traced down to a depth of 150 km. Crustal event on transverse faults in the forearc are suggested to accomplish differential lateral stresses between subduction zone segments (HABERLAND et al., 2006).
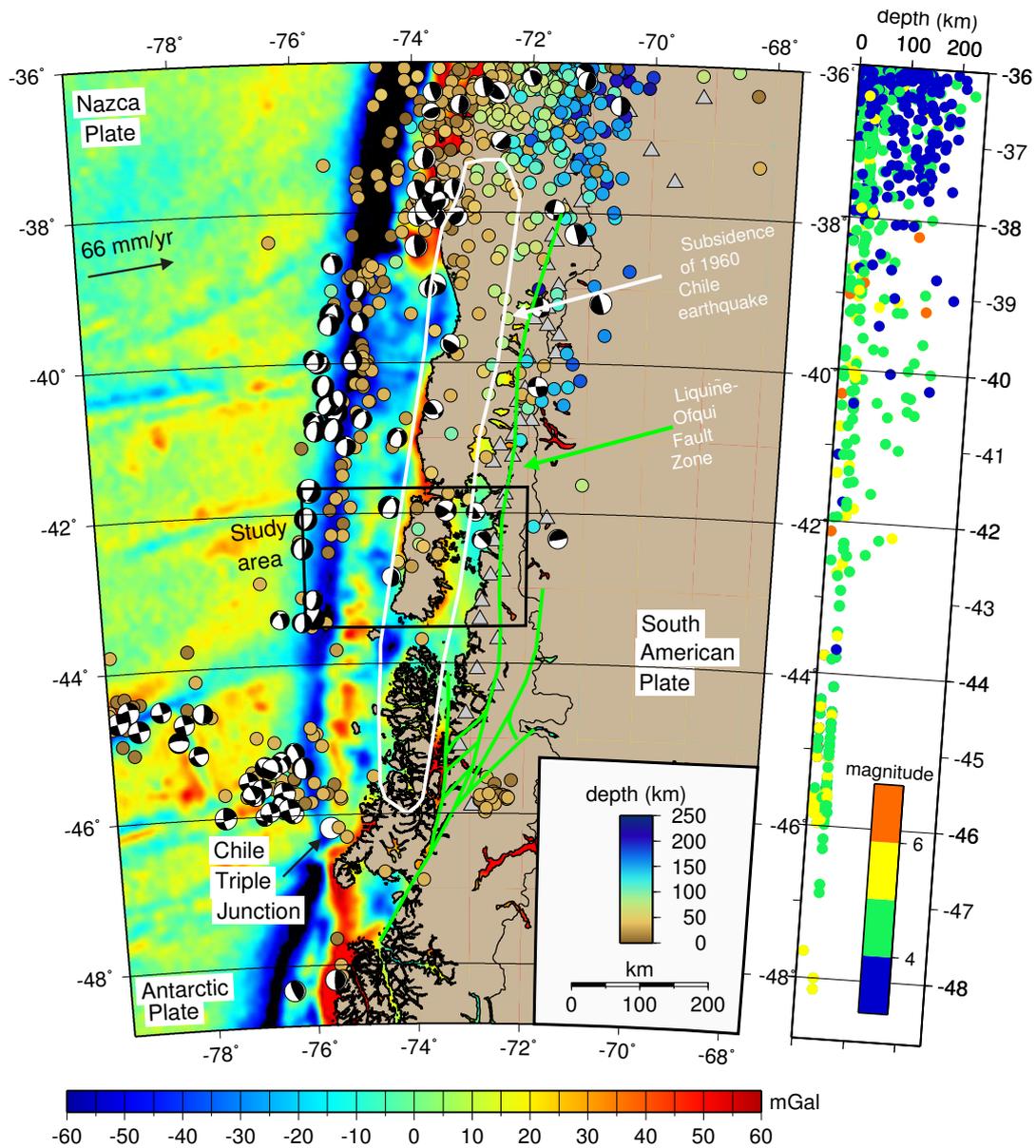
Figure 2.3: Map of the southeast Pacific and southern Chile with background seismicity. Left: Earthquake locations plotted from the CMT (1976-2007, lower hemisphere plot) and PDF (1990-2007) catalogue, magnitude range is between 3.9 and 7.6. Direction and velocity of the Nazca plate relative to the South American continent is shown according to ANGERMANN et al. (1999). The dashed line indicates the extent of subsidence associated with the 1960 Chile earthquake (PLAFKER & SAVAGE, 1970). Free Air anomaly from SANDWELL & SMITH (1997). Right: Hypocentres projected onto a N-S vertical cross-section clearly show a decrease of seismic events towards the South. The amount of teleseismic observations is too low to determine the structure (e. g. inclination) of the Benioff zone.

Apart from the May 1960 mega-earthquake, other strong events between 39°S and 42°S occurred in the years 1575, 1737 and 1837 but the focal parameters are not well constrained (LOMNITZ, 1970, 2004). CISTERNAS et al. (2005) suggest from estuary sediments (Río Maullín) that much of the fault dislocation that occurred in 1960 stemmed from a release of energy that had accumulated since 1575, and was only partly decomposed from the minor events which occurred 1737 and 1837. Hence, they propose a recurrence interval for mega-earthquakes to be approximately 375 years for southern Chile.

2.3 Intra-arc Liquiñe-Ofqui Fault Zone (LOFZ) and its Previous Seismic Data

Bulk transpressional deformation is expected at continental margins where the convergence vector is oblique with respect to the plate boundary zone (e. g. SANDERSON & MARCHINI, 1984, DEWEY et al., 1998, FOSSEN & TIKOFF, 1998). Kinematic models show that transpressional deformation arising from oblique convergence is accommodated by distinctive structural styles along and across different plate boundaries, which mostly depends on the angle of obliquity defined as the angle between the convergence vector and the normal to the trench (e. g. JARRARD, 1986a, MCCAFFREY, 1992). For small angles of obliquity, transpression is homogeneously distributed as in the case of the Australian-Pacific plate boundary in New Zealand (TEYSSIER et al., 1995). For large angles of obliquity, complete partition of transpression is expected. This is the case of the Pacific-North America plate boundary of the western US, where the San Andreas Fault takes up most of the simple shear components (TEYSSIER et al., 1995). The general case will be that of heterogeneous transpression in which discrete domains across the plate boundary accommodate wrench-dominated or pure-shear dominated transpression (e. g. FITCH, 1972, FOSSEN et al., 1994, TIKOFF & GREENE, 1997). However, the nature and degree of deformation partitioning will not only depend on the angle of obliquity. For instance, thermally weak intra-arc shear zones can accommodate a significant part of the bulk transpressional deformation arising from oblique convergence and affecting the predictions of kinematic models (e. g. DE SAINT BLANQUAT et al., 1998). The southern Chilean Andes provide a natural laboratory for examining the nature of long-term and short-term transpressional deformation across an obliquely convergent continental margin because of its well constrained plate kinematic history. This shows steady right-lateral oblique subduction of the Nazca plate beneath South America since 48 Ma with the exception of nearly orthogonal convergence from 26 to 20 Ma (PARDO-CASAS & MOLNAR, 1987, SOMOZA, 1998). At present, the angle of obliquity of the Nazca-South America plate convergence vector is, with respect to the orthogonal to the trench normal, approximately

18° for southern Chile (ANGERMANN et al., 1999, KENDRICK et al., 2003, HOFFMANN-ROTHE et al., 2006). The inclination of the Wadati-Benioff zone is 30° (HABERLAND et al., 2006) and the age of the subducting Nazca plate decreases from 30 Ma at 38°S to virtually 0 Ma at 46°S (MÜLLER et al., 1997), where the Chile ridge is currently subducting (HERRON et al., 1981, FORSYTHE & NELSON, 1985, CANDE & LESLIE, 1986, MURDIE et al., 1993, BOURGOIS et al., 1996, RAMOS, 2005). Available structural and thermo-chronological data documents that the intra-arc Liquiñe-Ofqui fault zone (LOFZ) in the Patagonian Cordillera has accommodated concomitant strike-slip, oblique-slip and reverse-slip ductile to brittle deformation over the last 6 Ma (HERVÉ et al., 1994, LAVENU & CEMBRANO, 1999). However, the current deformation state of the arc and the fault zone is still poorly known because of the lack of systematic seismic studies in this remote area of the Andes. A recent event on April, 21 2007 with M_w 6.2 Aysén (45.2°S) earthquake shows that the LOFZ is also capable of producing large magnitude earthquakes and therefore imposes a significant seismic hazard to this region. In this work the first local seismological study of a 130 km long segment of the Liquiñe-Ofqui fault zone is presented (Section 6.1).

The working area (box in Figure 2.4) is located in the southern part of the Southern Volcanic-Zone (SSVZ) segment (LÓPEZ-ESCOBAR et al., 1995, NARANJO & STERN, 2004). The magmatic arc exhibits volcanic activity during the Quaternary (CASERTANO, 1963, SIEBERT & SIMKIN, 2002) which coincides with the location of the intra-arc shear zone LOFZ (CEMBRANO et al., 1996). It was suggested that the LOFZ controls the location of the larger strato-volcanoes (STERN, 2004). This segment of the Andes was part of the proto-Pacific margin of Gondwana and consists of low grade sediments, meta-basites, and granitoids which belong to the Patagonian batholith (PANKHURST et al., 1992). The eastern side of the LOFZ had been uplifted and exhumed faster compared to the western side (ADRIASOLA et al., 2006). These kind of margin-parallel strike-slip faults located in magmatic arcs have also been found in other subduction zones with oblique subduction (e. g. BECK JR., 1983, JARRARD, 1986b, MCCAFFREY et al., 2000). The LOFZ seems to be the eastern border of a detached continental sliver which moves northward relative to the continent (BECK JR., 1983, NELSON et al., 1994, BECK JR. et al., 2000, WANG et al., 2007). Evidence for movement of the LOFZ since the Pliocene (CEMBRANO et al., 1996, LAVENU & CEMBRANO, 1999) is well established. Between 40°S and 42°S latitude, complete partitioning of oblique convergence into a margin-normal component (accommodated by the mega-thrust) and a margin-parallel strike-slip component (along the LOFZ) has been proposed by ROSENAU et al. (2006).

While crustal seismicity below the magmatic arc is regularly observed in central Chile at 34°S (BARRIENTOS et al., 2004) it is not common for the southern part of the Andes (BOHM et al., 2002, FOLGUERA et al., 2004, ROSENAU et al., 2006). Only five shal-
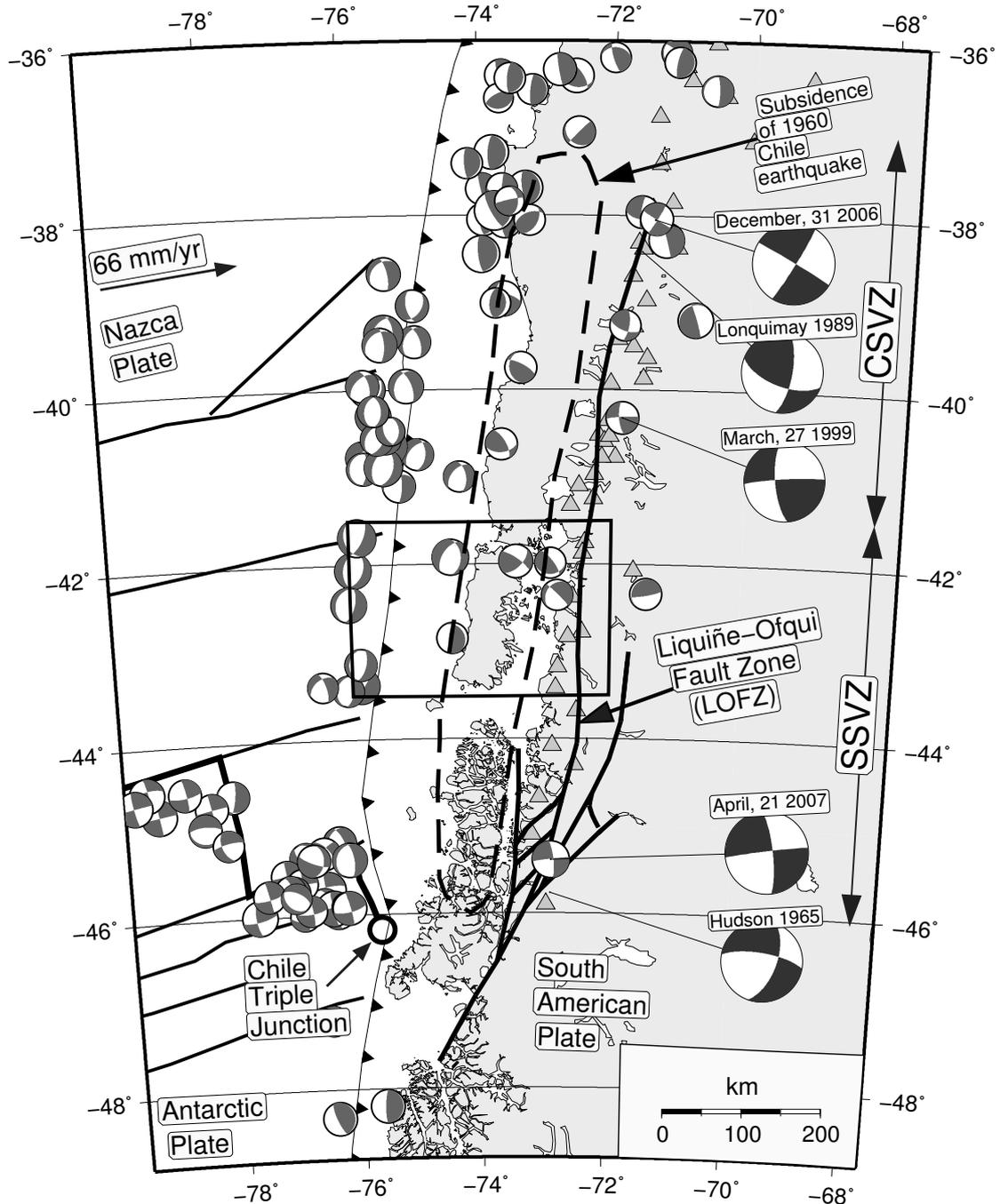
Figure 2.4: The southern Andes between 36° and 49°S with LOFZ, oceanic features and historical focal mechanisms (Global CMT catalogue). Crustal focal mechanisms attributed to the LOFZ (CHINN & ISACKS, 1983, DZIEWONSKI et al., 1990, 2000b) plotted with big focal mechanisms. All these teleseismic fault plane solutions show strike-slip movements. The box indicates the location of the seismic network. LOFZ according to CEMBRANO et al. (2000), subsidence of 1960 earthquake from PLAFKER & SAVAGE (1970), plate convergence after ANGERMANN et al. (1999). Volcanoes plotted as grey triangles (SIEBERT & SIMKIN, 2002). Petrographic provinces of the Southern Volcanic Zone from LÓPEZ-ESCOBAR et al. (1993, 1995) (SSVZ=South Southern Volcanic Zone, CSVZ=Central Southern Volcanic Zone). Modified after LANGE et al. (2008)

Table 2.1: Summary of historical fault plane solutions for shallow earthquakes along the LOFZ derived from teleseismic observations (CHINN & ISACKS, 1983, DZIEWONSKI et al., 1990, 2000a) and global CMT catalogue.

Nr.	Date/ Time	Lat/ Lon	Depth [km] NEIC/CMT	Strike/Dip Rake	Magnitude (M_w)	Reference
1	1965-11-28 03:56	45.77°S 72.90°W	– 33	20/60 -160	M_s 6.0 –	CHINN & ISACKS(1983)
2	1989-02-24 12:36 48.0	39.26°S 71.83°W	– 15	110/62 23	5.2 –	DZIEWONSKI et al.(1990) event 129
3	1999-03-27 11:13 35.6	40.32°S 71.85°W	33 15	174/72 174	5.4 –	DZIEWONSKI et al.(2000) event 229
4	2006-12-31 14:55 06.6	38.04°S 71.40°W	33 12	031/86 178	5.5 –	CMT –
5	2007-04-21 17:53 48.5	45.39°S 72.89°W	44 12	353/78 177	6.2 –	Quick CMT –

low events along the whole LOFZ have been teleseismically observed so far (Figure 2.4). However, these earthquake locations have only limited depth accuracy so that the seismicity cannot clearly be assigned to the shallower crust. The fault plane solution from CHINN & ISACKS (1983) is a M_s 6.0 event which was attributed to an eruption of the Hudson volcano in the year 1965 at 46°S (ROSENAU et al., 2006). The other fault plane solution (M_w=5.2) from DZIEWONSKI et al. (1990) had been associated with the 1989 eruption of the Lonquimay strato-volcano (BARRIENTOS & ACEVEDO-ARANGUIZ, 1992). As recently as April 21, 2007, a strong event (M_w=6.2) occurred near Aysén (45.2°S, Figure 2.4). A summary of all teleseismic fault plane solutions possibly related to the LOFZ is shown in Table 2.1. The teleseismic events are mainly distributed at the northern and southern end of the LOFZ, while for the central segment of the LOFZ no fault plane solution is so far available. All teleseismic fault plane solutions (big focal mechanisms in Figure 2.4) show strike-slip movements in line with the expected movement along the LOFZ. North of 38°S, the LOFZ descends in the Antiñir-Copahue fault zone for which FOLGUERA et al. (2004) showed the existence of Neogene faulting. At Lonquimay volcano (38°S) BARRIENTOS & ACEVEDO-ARANGUIZ (1992) observed local seismicity after the eruption of Lonquimay volcano on December 25, 1988. The events were located beneath the crater of the Lonquimay volcano and did not exceed depths of 10 km. Other local networks along the LOFZ have so far not observed events directly located at the LOFZ (MURDIE et al., 1993, MURDIE & RUSSO, 1999, BOHM et al., 2002) or reported only minor seismicity along the LOFZ (HABERLAND et al., 2006).

2.4 Morphotectonic Units of the Southern Andes

Different north-south striking morphotectonic units along the southern Andean margin have developed (also GANSSER, 1973, ZEIL, 1986, MELNICK & ECHTLER, 2006). The units are introduced from west to east following the subducting Nazca plate (Figure 2.5):

Outer rise

The outer rise is a broad up-warping of the oceanic lithosphere just before it descends into the trench at the subduction zone. As part of the TIPTEQ project two temporal OBS/OBH networks were installed at the outer rise at 43°S and 44.5°S (SCHERWATH et al., 2006, TILMANN et al., 2007). The outer rise shows repeated earthquakes with mostly shallow (<10 km) hypocentres which are aligned along the preexisting (ridge generated) seafloor fabric (TILMANN et al., 2007). By using wide-angle data, CONTRERAS-REYES et al. (2007) observed a 5.3 km thick oceanic crust and a v_p velocity with 8.3 km/s for the upper mantle beneath the outer rise. Velocities decrease to abnormally low values in direction of the trench which suggests fracturing and hydration of oceanic crust and uppermost mantle due to bending mechanisms (CONTRERAS-REYES et al., 2007). In contrast to central Chile, basement rocks in the outer rise east of the area under investigation frequently pierce the sedimentary blanket.
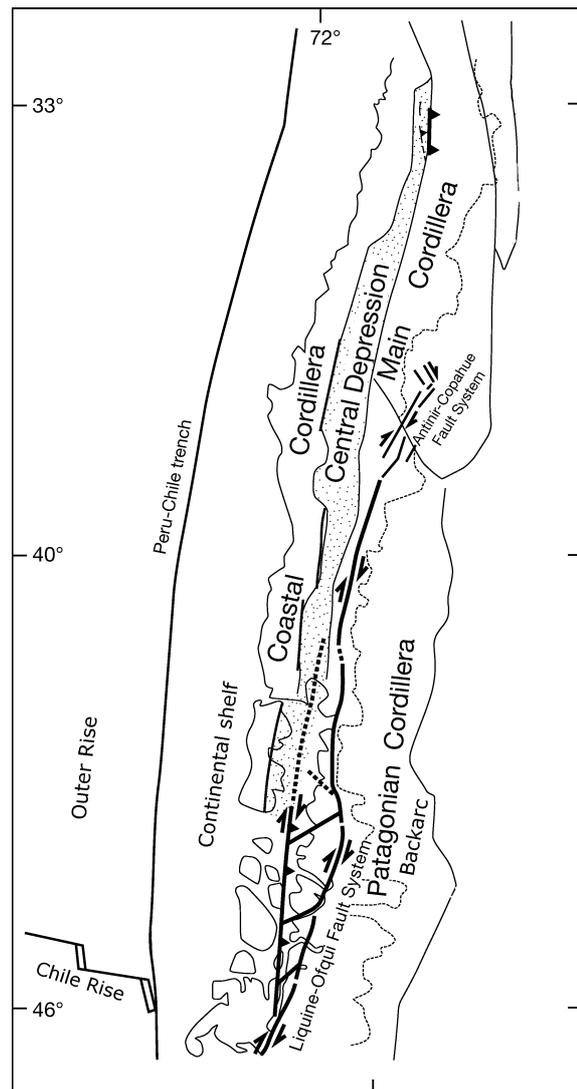

Figure 2.5: Map showing the main morphological units with the regional Neogene fault systems of southern Chile (modified after CEMBRANO et al., 2007).
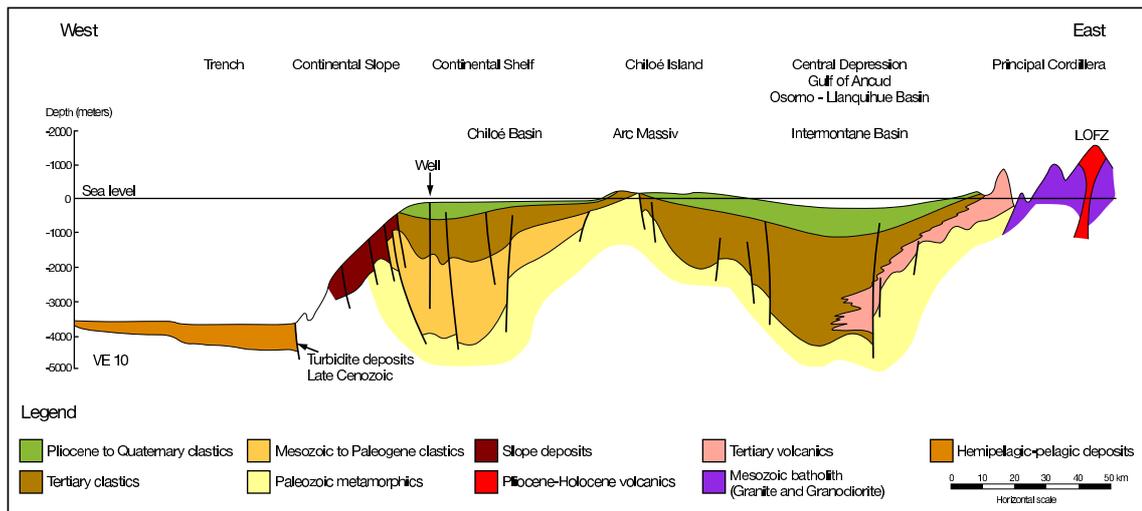
Figure 2.6: Geologic cross section along 42°S showing the sedimentary basins. Simplified after GONZÁLEZ (1990).

Forearc

Trench:

The trench is a pronounced bathymetric depression along the South American subduction zone. At 33°S the subducting Juan Fernández ridge forms a bathymetric barrier that ponds sediment transport to the north (VON HUENE et al., 1997, YÁÑEZ et al., 2001, 2002). South of the Juan Fernández ridge, the trench is covered by 2 km sediments which were mainly accumulated during the Pleistocene glaciation (BANGS & CANDE, 1997). The trench in the area under investigation is up to 4100 m deep and mainly filled with turbidites (THORNBURG & KULM, 1987b,a).

Continental Slope and Shelf:

The 60 km wide continental shelf and the upper continental slope is the location of the Chiloé basin. The basin is filled with up to 3000 m clastic sediments (Figure 2.6) which have accumulated since the late Cretaceous (MORDOJOVICH, 1981, GONZÁLEZ, 1990).

Coastal Cordillera:

This unit forms the westernmost belt on Chiloé Island (Figure 2.5) and consists mainly of low-grade meta-sedimentary rocks interpreted as a forearc accretionary complex (HERVÉ, 1988). THOMSON & HERVÉ (2002) dated the complex to be late Triassic to early Jurassic in age. In the northern and southern Coastal Cordillera, Oligocene to Miocene sediments are located (SERNAGEOMIN, 2003).

Central Depression/Longitudinal Valley:

The Central Depression ("Valle central") is a 1300 km long depression which starts in the north at 33°S, close to Santiago, and extends southwards as a 70 km wide trench parallel feature. In the working area the central depression is below sea level (Figure 2.5). The

central depression is a sedimentary basin filled with Tertiary and Quaternary sediments (Figure 2.6) and comprises the Gulf of Ancud, Gulf of Corcovado and the eastern part of Chiloé Island.

Main Cordillera:

The Main Cordillera ("Cordillera Principal") comprises the magmatic arc and shows the highest topographic elevations in the working are. Between 38°S and 46°S, the eastern limit of the central depression limits the volcanic arc where the LOFZ (see also Section 2.3) has been developing (LAVENU & CEMBRANO, 1999). At 41°S the activity of the magmatic arc shows an oscillatory eastward-westward shifting beginning with the Late Jurassic (MPODOZIS & RAMOS, 1990). Outcrops of the Patagonian batholith are widespread (Figure 2.7). The granitoids rocks of the batholith formed as a 1000 km continuous north-south striking unit and consist of Late Jurassic to Pliocene intrusive rocks (HERVÉ et al., 2000). Main emplacement occurred during the middle Cretaceous (MPODOZIS & RAMOS, 1990), with younger intrusion ages in the centre (PANKHURST et al., 1999). Parallel to the magmatic arc, the LOFZ, a dextral strike-slip zone active since the Miocene developed (see also Section 2.3). East of the Liquiñe-Ofqui fault zone there are outcrops of mafic igneous rocks which are probably part of a Paleozoic accretionary complex (PANKHURST et al., 1992, ROJAS et al., 1994). The high summits along the Main Cordillera are formed by Quaternary volcanoes, e. g. the stratovolcanoes Michinmahidua (2404 m) and Corcovado (2300 m) (NARANJO & STERN, 2004).

Backarc

In contrast to northern Chile where a fold and thrust belt has developed (JAILLARD et al., 2000, RAMOS, 2000), the backarc at 41°S exhibits only weak deformation leading to long-wavelength open folds (MOORES & TWISS, 1995, JAILLARD et al., 2000). It consists of a sequence of Jurassic rhyolitic rocks overlain by early Cretaceous, intra-arc basin sediments. This sequence is overlain by plateau basalts which formed during late Cretaceous and Tertiary (MPODOZIS & RAMOS, 1990). The series finishes with basalts forming the Somún Curá plateau from the Eocene and Oligocene (RAMOS & AGUIRRE-URRETA, 2000, JORDAN et al., 2001).
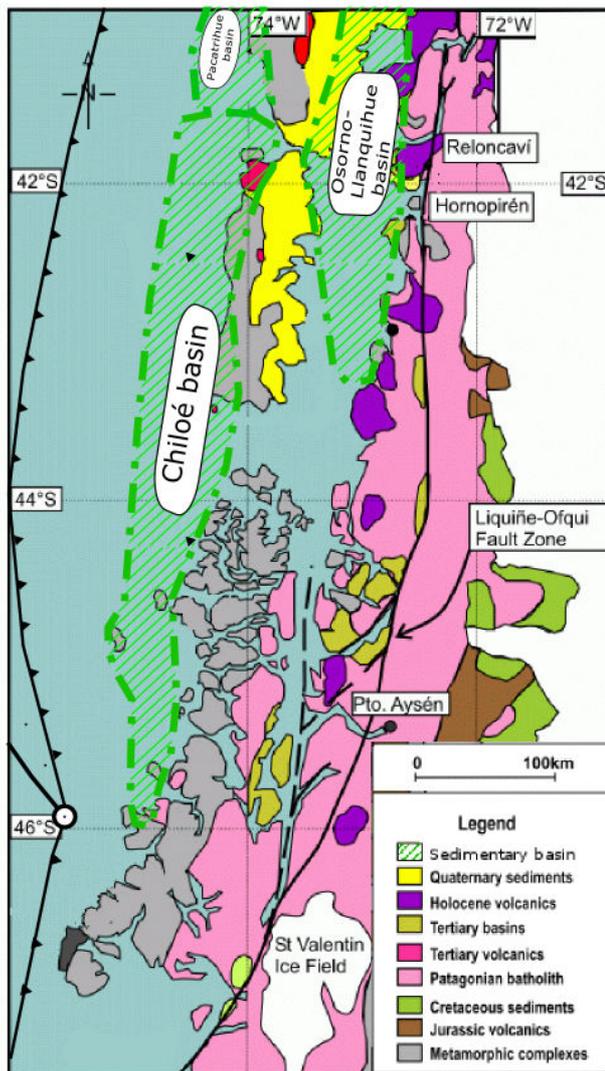
Figure 2.7: Simplified geology of the southern Chilean Andes (modified according to MUÑOZ, 2003) and sub-surface extent of sedimentary basins (GONZÁLEZ, 1990, JORDAN et al., 2001).

Chapter 3

Experiment and Data Processing

Between December 2004 and November 2005 an amphibious seismic network consisting of 18 land stations and 20 offshore stations was deployed on the Island of Chiloé, in the corresponding continental region around Chaitén and on the offshore forearc between 41.5°S and 43.5°S (Figure 3.1). The network was part of the international and interdisciplinary research initiative TIPTEQ (from **T**he **I**ncoming **P**late **T**o mega-Thrust **E**arth**Q**uake Processes) financed by the German ministry of education and research (BMBF). It was installed and maintained by the University of Potsdam (Germany), the University of Liverpool (UK), the University of Hamburg (Germany) and the University of Concepción (Chile). The average station spacing (using the mean of the distances between the next three immediate neighbours) for land stations and OBS/OBH was 31 km and 24 km, respectively (Table 3.1). The network is therefore well suited to observe local (micro-)earthquakes as well as teleseismic events. The total amount of collected waveforms from the amphibious network is shown in Figure 3.2.

3.1 Acquisition of Data and Instrumentation

Land stations

The EDL land stations (EDL=**E**arth **D**ata **L**ogger) were equipped with three-component 1 Hz sensors (Mark L4-3D) running in continuous mode at a sample rate of 100 Hz.

Table 3.1: Average station distances using different amounts of immediate neighbours

Region	Stations	Distance between stations [km] (using the immediate neighbours)		
		next 3	next 5	next 10
onshore	18	31.0	39.3	56.5
offshore	17	24.6	29.8	41.0
Total	35	26.9	33.3	46.8
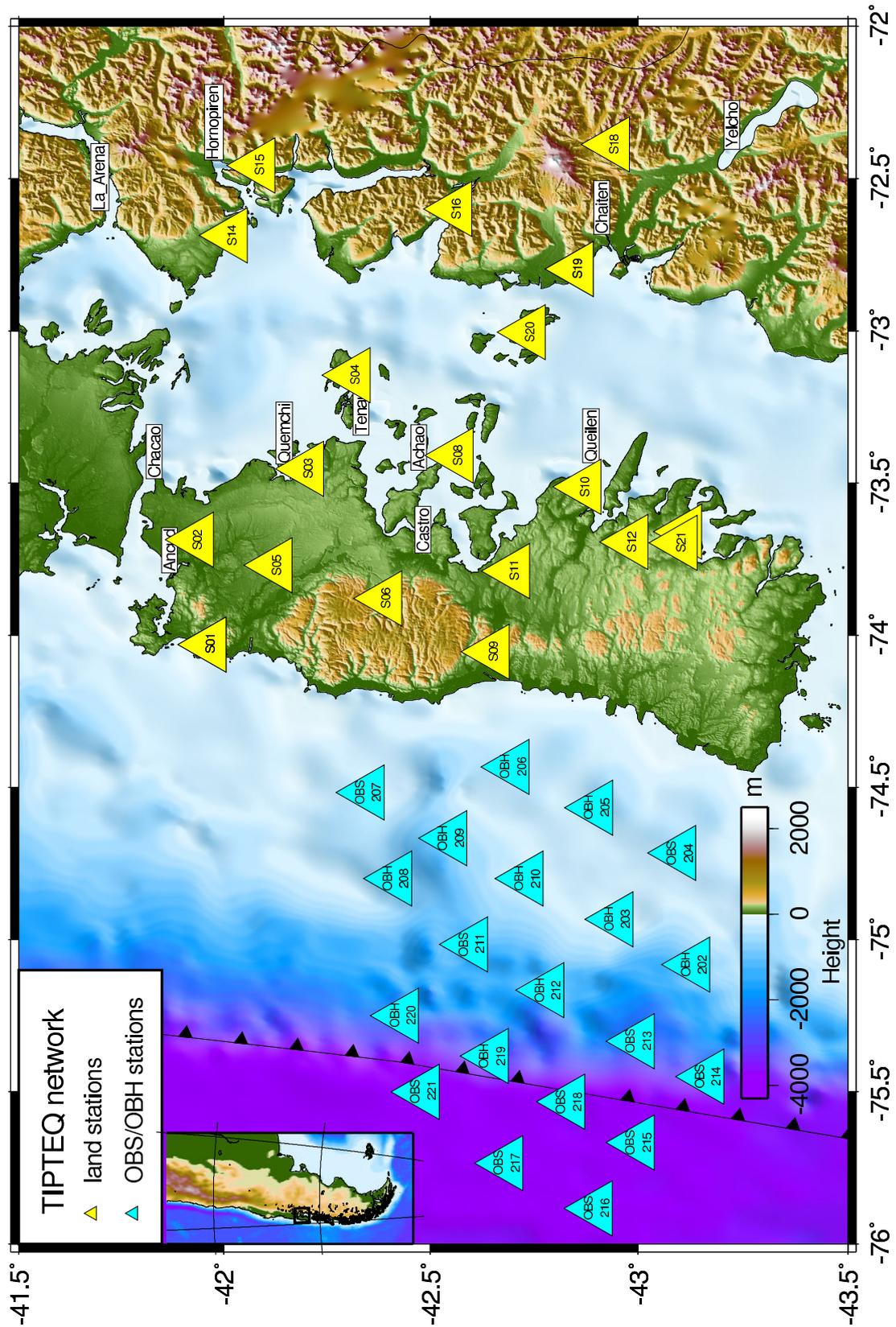
Figure 3.1: Distribution of seismic stations used in this study (yellow=land stations, blue=OBH/OBS stations). Topography according to WWW-SRTM (2007), bathymetry from WWW-BODC (2003)
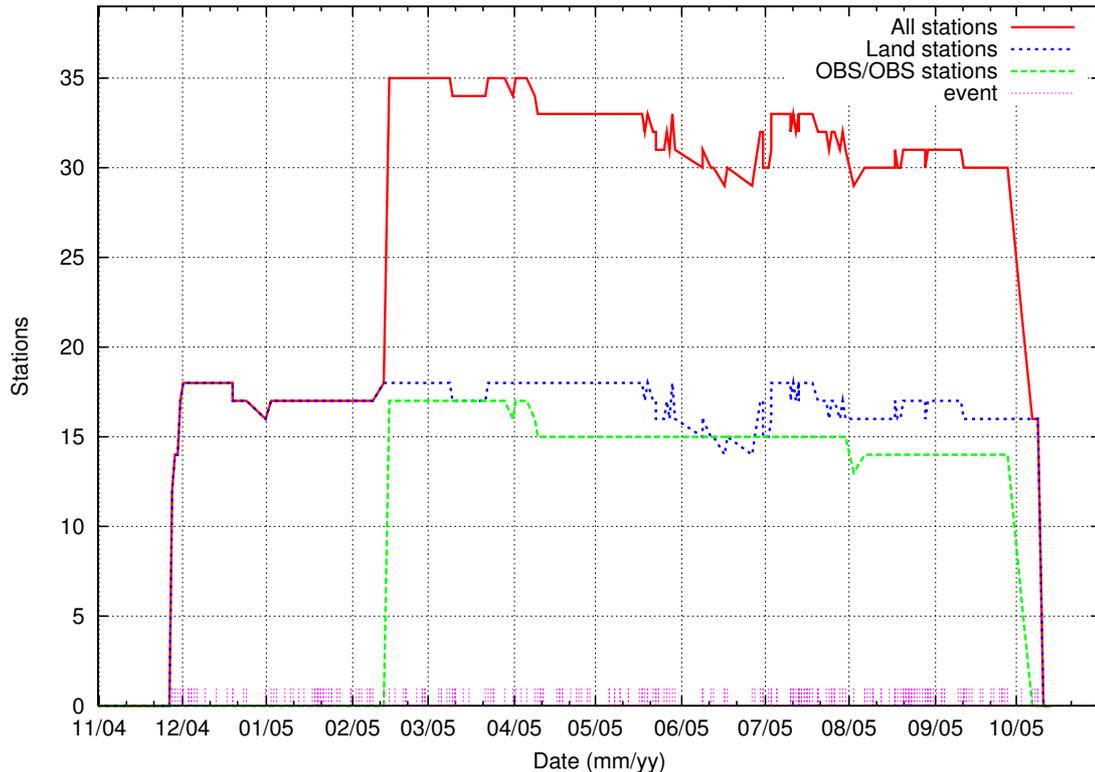
Figure 3.2: Amount of obtained station waveform data versus time. Purple dashes above the x-axis indicate triggered local events.

Accurate time stamps for the waveforms were received by GPS satellites. Each station was equipped with a photovoltaic system including battery charger, two closed batteries (2×65 Ah) and two solar panels (2×50 W). Around most of the stations fences needed to be installed as protection against animals (Figure 3.3). Each station produced approximately 35 Megabytes of compressed raw data per day, the total amount of collected station days amounts to 5600 days. The total size of collected raw data amounts to 195 gigabytes for the land stations. The stations were visited, checked and the data recovered in cycles of approximately three months. During these visits the collected data was copied to a notebook, and each day backups of the raw data on DVD's were carried out. Besides minor failures based on low energy supply or water infiltration, most of the land stations worked reliably.

Ocean button seismometers (OBS) and hydrophones (OBH)

In February 2005, additional 10 three-component, ocean bottom seismometers (OBS) and 10 ocean bottom hydrophones (OBH) were installed west of Chiloé Island thereby extending the seismic array to the west beyond the trench. The installation was carried out with the German research vessel "SONNE" (cruise SO #181). The deepest station was installed at 3775 m water depth. The complete network was dismantled in October 2005.

Figure 3.3: Left: EDL station with battery, datalogger and Mark L4-3D seismometer and external service unit. Middle: EDL station deployment with solar panels and additional fence against animals. Right: OBS station.

All OBS/H stations ran continuously with a sample rate of 50 Hz. The OBS stations were equipped with a three-component sensor and a hydrophone channel, equalling four channels in total. The OBH stations registered the hydrostatic pressure only. Internal clocks of the OBS/H stations were synchronized twice with GPS time during the installation and recovery phase. The internal time of the datalogger was then corrected assuming a linear drift. The correction of the internal clocks was carried out by S. Hofmann, University of Hamburg.

3.2 Event Detection and Phase Picking

Automatic event detection using a LTA/STA algorithm and polarizations (ASCH, 1998) was carried out on the continuous data stream. Event association was done independently on the offshore and onshore networks by using a network coincidence criterion. Furthermore, all waveforms were inspected visually to search for weak events. Figure 3.4 shows two representative local events registered by the network.

Determination of accurate arrival times and initial locations was done manually with the software package GIANT (RIETBROCK et al., 1998). Whenever possible, the arrival time determination ("phase picking") was carried out on unfiltered raw data for the land-stations. The continuous background noise level of the offshore data is much higher compared to the onshore station data. The primary sources of this well-know phenomenon are the wave surf and standing waves in the ocean, with water movement continuously generating surface waves in the solid earth (e. g. LAY & WALLACE, 1995). Therefore the OBS data was high-pass-filtered before phase picking.

In total 364 local events were detected during the experiment, and the amount of 7698 (P: 4141, S: 3557) arrival times were determined. The onsets of the OBS/OBH stations are not of the same quality compared to the onsets registered by the land stations. This is reflected by the lower number of phase onsets picked on the OBS/H stations; only
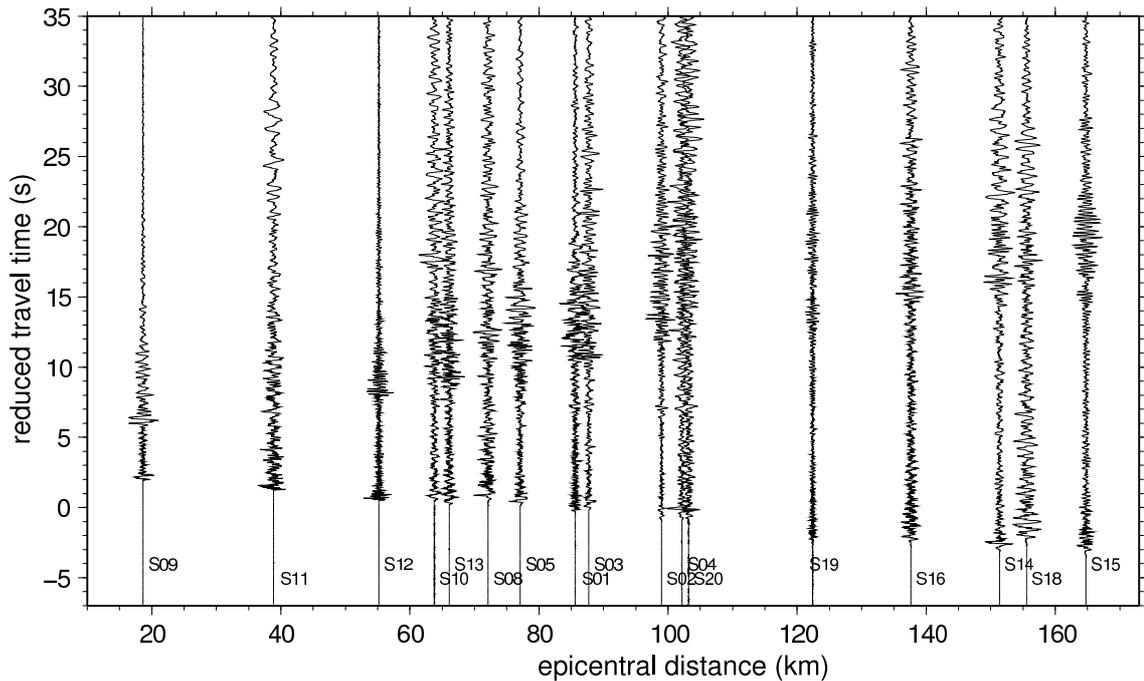
(a) Local event near coast of Chiloé Island (January 20, 2005, 15:11:31 UTC, 4.5 M_l, lat: -42.7232°, lon: -74.3039°, 25 km depth). Vertical components of EDL dataloggers plotted versus epicentral distance with a reduction velocity of 6 km/s.
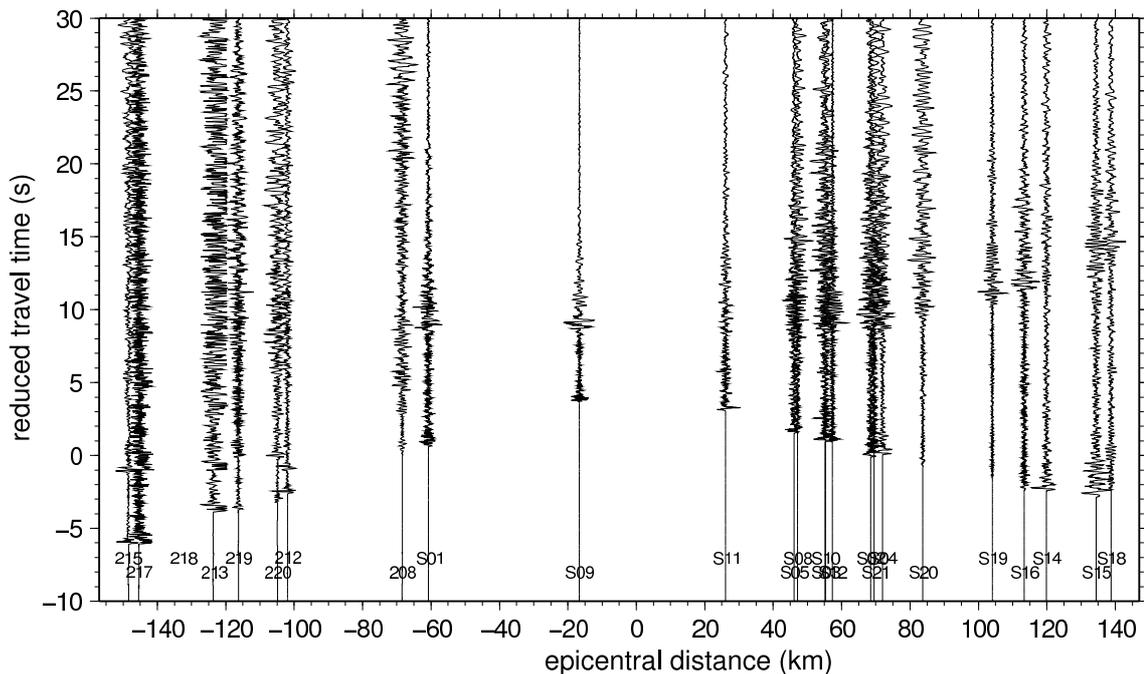
(b) Local event beneath Chiloé Island at 42 km depth (August 23, 2005, 08:44:18 UTC, 5.1 M_l, lat: -42.4972°, lon: -73.9783°). Vertical components of seismometers (land stations) and hydrophone channels (offshore stations) plotted versus hypocentral distance. Reduction velocity is 6 km/s. Negative epicentral distances are assigned to stations east of the event where mainly OBS/H are located. S-phases from OBS/OBH stations could rarely be picked.

Figure 3.4: Components (EDL: vertical component; OBS/H hydrophone channel) of two local events plotted versus hypocentral distance using a reduction velocity of 6 km/s. Only waveforms with high P onset quality are shown.
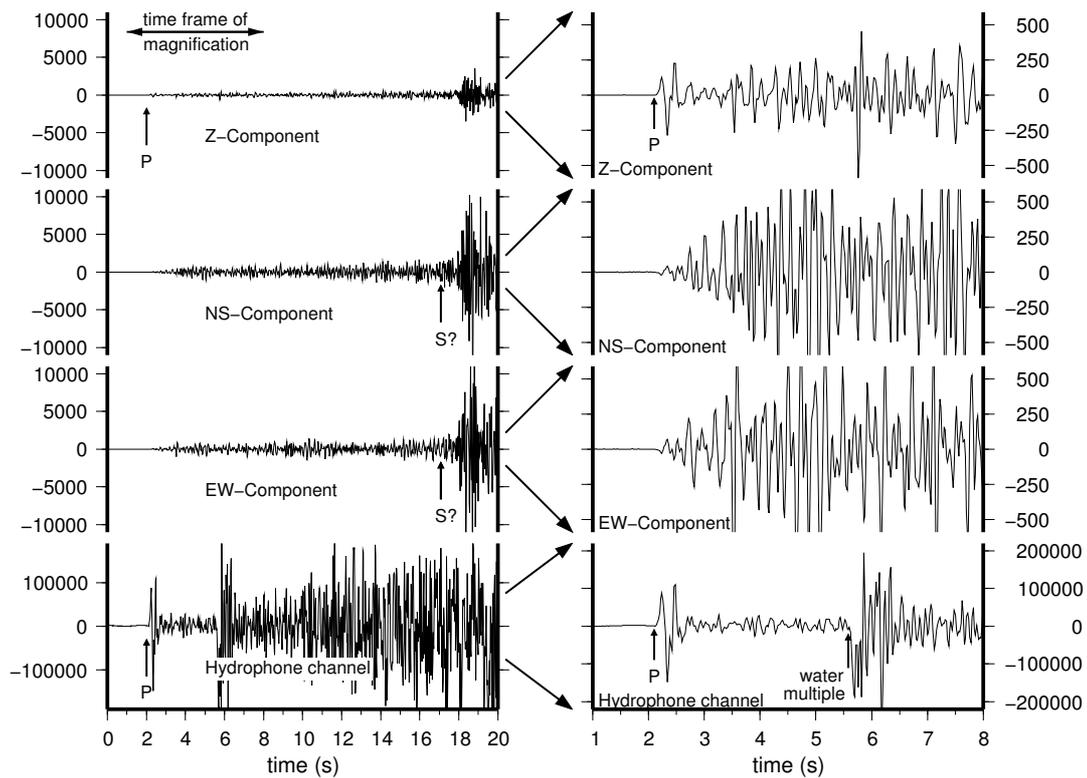
Figure 3.5: Event registered at OBS #214, located at 2641 m water depth (August 23, 2005 08:44:18 UTC, lat: -42.4972°, lon: -73.9783°, 42 km depth, M_l=5.1). The hypocentral distance is 120 km. The most pronounced P phase onset is usually found on the hydrophone channel regularly followed by water multiples and converted phases. S phases could rarely be picked from the OBS station data. Left side: Time window with P and possible S phase onsets. Right side: P onset is followed on the hydrophone channel by water multiples and/or converted phases.

15% of the determined arrival times are from the offshore stations. Figure 3.5 shows a registration of an OBS station. The most pronounced P phase onset is usually found at the hydrophone channel regularly followed by water multiples. Therefore the time of the P onset was generally determined by using the hydrophone channel. If possible, S phases were picked on the horizontal components.

Chapter 4

Methods and Techniques

In this chapter the methods applied are presented. The inversion of arrival time data results in a minimum 1-D velocity model. This 1-D model is later used as the starting model for the inversion of a 2-D velocity model (Section 4.1). The velocity models are needed for accurate hypocentre location, and yield important information about the structure of the working area.

The second group of methods are applied to receive information about the source mechanism of the measured earthquakes through its radiation pattern, allowing the fault type of the earthquake to be identified, which again is dependent on the stress field near the source. For the calculation of the focal mechanism two methods were applied in this study. In case that the event is inside the network, the focal mechanism can be calculated by using first-motion polarities. Moment tensor inversion allow the focal mechanism for events also outside the network to be determined, if the distance to the network is small and the signal-to-noise ratio is high. Finally, groups of earthquakes are inverted for the local stress field.

4.1 Simultaneous Inversion of Travel Time Data for Hypocentral Parameters and Velocity Structure

The method of seismic inversion methods has become widely used in earth sciences during the last decades (ZHAO & KAYAL, 2000). Passive tomographic techniques used in seismology are the teleseismic tomography (AKI et al., 1976) and local earthquake tomography (AKI & LEE, 1976, KISSLING, 1988). Here, local earthquake tomography (LET) is applied to invert for a 2-D velocity model of the upper crust. An introduction into the most important aspects of the method can be given here; for a thorough elaboration the reader is referred to the article of THURBER (1983) and the references therein.

The body wave travel time T from an earthquake source i to a seismic station j is expressed using ray theory as the path integral (THURBER, 1993)

$$T_{ij} \;=\; \int\limits_{source}^{station} u \;\; ds \tag{4.1}$$

where u is the slowness (reciprocal of velocity) and ds is an element of path length. The actual observations are the arrival times t_{ij}, where

$$t_{ij} \;=\; \tau_i \;+\; T_{ij} \tag{4.2}$$

and τ_i is the earthquake origin time (THURBER, 1983). For a given set of arrival times t_{ij}^{obs}, the calculated arrival times t_{ij}^{cal} can be determined from equation 4.1 and 4.2 using trial hypocentres, origin times and an initial model of the seismic velocity structure (the "a priori" information). The misfit between observed and 'predicted' (calculated) arrival times are the residuals r_{ij}:

$$r_{ij} \;=\; t_{ij}^{obs} \;-\; t_{ij}^{cal} \tag{4.3}$$

The residuals are a function of differences between calculated and observed earthquake origin times, hypocentre locations and velocity structure. The function r_{ij} is not linearly dependent on the travel time. The linear approximation by applying Taylor approximation of first degree around the start model (focal coordinates $\mathbf{x_i^0}$, earthquake origin time τ_i^0 and initial velocity model m^0) and finite parameterisation of the velocity structure is as follows (THURBER, 1983, SCHURR, 2000):

$$r_{ij} \;=\; \triangle\tau_i \;+\; \sum_{k=1}^{3} \frac{\partial T_{ij}}{\partial x_{i_k}} \,\triangle x_{i_k} \;+\; \sum_{l=1}^{L} \frac{\partial T_{ij}}{\partial m_l} \,\triangle m_l \tag{4.4}$$

with

$$\triangle\tau_i = \tau_i - \tau_i^0\,, \quad \triangle\mathbf{x_i} = \mathbf{x_i} - \mathbf{x_i^0}\,, \qquad \triangle m_l = m_l - m_l^0$$

$\triangle\tau_i$ and $\triangle x_{i_k}$ are perturbations to the hypocentral parameters in time and space, m_l represents the L parameters of the velocity model. The velocity model partial derivatives $\partial T_{ij}/\partial m_l$ are essential line integrals along the ray path reflecting the relative influence of each model parameter on a given travel time datum (THURBER, 1993). The non-linearity characteristics of the problem, linearized with equation 4.4, requires an iterative scheme for the solution. Next, we rewrite the hypocentre-velocity structure coupling inherent in equation 4.4 in a more general notation (MENKE, 1989):

$$\mathbf{d} \;=\; \mathbf{G\,m} \tag{4.5}$$

where $\mathbf{d}$ is the vector of the travel time residuals, $\mathbf{m}$ is the vector of model adjustments (hypocentres and velocities), and the matrix $\mathbf{G}$ contains the partial derivatives of travel times with respect to model parameters. If the number of observations is equal to the unknowns, $\mathbf{G}$ is square, and one can solve for $\mathbf{m}$ directly ($\mathbf{m} = \mathbf{G}^{-1}\mathbf{d}$, assuming that $\mathbf{G}$ has full rank). Because there are normally more observations than unknowns we define the *prediction error* $\mathbf{E}$ ($\mathbf{E} = \mathbf{d}^{obs} - \mathbf{d}^{pre} = \mathbf{d}^{obs} - \mathbf{Gm}$) as a measure of the misfit of the model. Minimizing $\mathbf{E}^2$ by setting the derivative of $\mathbf{E}^2$ with respect to the model parameters equal to zero leads to the *least squares solution* (LAY & WALLACE, 1995, 228p.):

$$\mathbf{m}^{est} = [\mathbf{G}^T\mathbf{G}]^{-1}\ \mathbf{G}^T\ \mathbf{d} \qquad (4.6)$$

where $\mathbf{G}^T$ is the transposed. This equation provides the best solution to $\mathbf{m}^{est}$ in a least-squares sense. Since $\mathbf{G}^T\mathbf{G}$ is a square matrix and symmetric, it has an inverse (as long it is not singular) and its eigenvalues are real (LAY & WALLACE, 1995). As a result of an irregular ray distribution, model parameters can be overdetermined and underdetermined in the same problem, making equation 4.5 a mixed determined problem (HUSEN, 1999). To avoid very small or zero eigenvalues for the underdetermined model parameters, damping is introduced to stabilize the numerical solution. By minimizing the solution length and prediction error (MENKE, 1989, 64pp. and 71p.), the solution of equation 4.5 (*"damped least squares solution"*) becomes:

$$\mathbf{m}^{est} = [\mathbf{G}^T\mathbf{G} + \epsilon^2\mathbf{I}]^{-1}\ \mathbf{G}^T\ \mathbf{d} \qquad (4.7)$$

where ϵ^2 is a damping parameter and $\mathbf{I}$ the unity matrix. The factor ϵ^2 determines the relative importance given to the prediction error and solution length. *Damped least-squares* mean that the norm of the model perturbations (more or less the complexity of the model) is weighted and combined with the squared data misfit – the combination is minimized at each iteration (EVANS et al., 1994). The damped least-squares solution is implemented in the programmes SIMULPS and VELEST, which are used for the travel time inversions of this study.

4.1.1   Joint Inversion of 1-D Velocity Structure

The computer programme VELEST (KISSLING et al., 1995) simultaneously calculates a local one-dimensional (1-D) velocity model, station corrections and accurate locations performing a joint inversion of the picked arrival time dataset. VELEST is widely used and provides very good hypocentral estimates (e. g. GRAEBER, 1997, SCHURR et al., 1999, HABERLAND et al., 2006, LANGER et al., 2007). The inversion scheme applied in this study follows the procedure described by KISSLING et al. (1994). The velocity model

is parameterised by a stack of flat layers with constant velocities over a half space. The
hypocentres of the 1-D velocity model differ only marginally from hypocentres of a 3-D
tomographic inversion as shown with data from northern Chile by GRAEBER & ASCH
(1999). This is because, if the hypocentres are well constrained, the unresolved part of
the model is absorbed by the station delays and travel time residuals rather than by shifts
in the hypocentral coordinates (SCHURR, 2000). See Section 5.1 for results of the joint
inversion using VELEST.

4.1.2   Joint Inversion of 2-D Velocity Structure

The programme SIMULPS (THURBER, 1983, EVANS et al., 1994) is used for simultane-
ous inversion of hypocentral parameter and velocity structure (v_p, v_p/v_s). The original
algorithm from THURBER (1983) was subsequently modified and enhanced with new
features (e. g. EBERHART-PHILLIPS, 1986, 1993, UM & THURBER, 1987, THURBER &
EBERHART-PHILLIPS, 1999). SIMULPS has been successfully used for various LET-
studies (e. g. GRAEBER & ASCH, 1999, HABERLAND & RIETBROCK, 2001, DESHON
& SCHWARTZ, 2004). The algorithm supports a detailed configuration of the inversion
process. The latest version of the algorithm allows the linking of grid nodes, which again
enables one to form blocks of constant velocity or gradient (THURBER & EBERHART-
PHILLIPS, 1999). Explosions can be introduced into the inversion as events with known
location and origin time. The programme is calculating the full resolution and model
covariance matrices.

The velocity model is represented by velocity values specified on a three-dimensional
grid of nodes. The spacing between any pair of adjacent planes can be chosen arbitrary
(EVANS et al., 1994). The velocity for a given point ($\mathbf{x} = (x_1, x_2, x_3)$) inside the grid
is calculated by linearly interpolating the eight neighbouring grid nodes $(p_{1,1}, p_{1,2}, p_{1,3})$,
$(p_{1,1}, p_{1,2}, p_{2,3}), \ldots, (p_{2,1}, p_{2,2}, p_{2,3})$ (THURBER, 1983):

$$v(x_1, x_2, x_3) = \sum_{i_1=1}^{2} \sum_{i_2=1}^{2} \sum_{i_3=1}^{2} v(p_{i_1,1}, p_{i_2,2}, p_{i_3,3}) \cdot \prod_{j=1}^{3} \left(1 - \left| \frac{x_j - p_{i_j,j}}{p_{2,j} - p_{1,j}} \right| \right) \qquad (4.8)$$

The formula adds the velocity values of the next eight nodes and weights the velocity
values depending on the distance from $\underline{s}$ to the adjacent nodes. During the inversion
many, travel times (path integral formula 4.1) have to be calculated. For a fast calculation
of the path integral, THURBER (1983) implemented the ray tracer with "Approximative
Ray Tracing" technique (ART). Receiver and source are connected with different circular
arcs with varying radii and inclinations. Then, the 2-D circular arcs are perturbed in
3 dimensions to further minimize its travel time in an iterative process (UM & THURBER,
1987).

4.2 Focal Mechanism

The radiation pattern of an earthquake can be used to estimate the possible rupture plane orientation. First-motion polarities for all events were manually picked and used to calculate fault plane solutions (REASENBERG & OPPENHEIMER, 1985). Below the magmatic arc, no fault plane solutions using first-motion polarities could be calculated due to insufficient coverage of the focal plane. Hence, for these areas, moment tensors inversion using body waves were applied. The methods applied are introduced on the following pages.

4.2.1 The Moment Tensor

The full mathematical description of a point source is represented by the moment tensor (GILBERT, 1970). The elements M_{ij} of the moment tensor represent nine possible couples in the Cartesian source coordinate system for a general seismic point source. The components M_{ij} are the representations of forces in th x_i directions with moment arms in the x_j directions. The displacement field for a generally orientated dislocation point source can be described with these nine components (even allowing displacements normal to the fault, e. g. extensional or compressional characteristics). The full set of force couples, M_{ij}, is shown in Figure 4.1. The tensor depends on the source strength, fault orientation and the orientation of the Cartesian coordinate system.
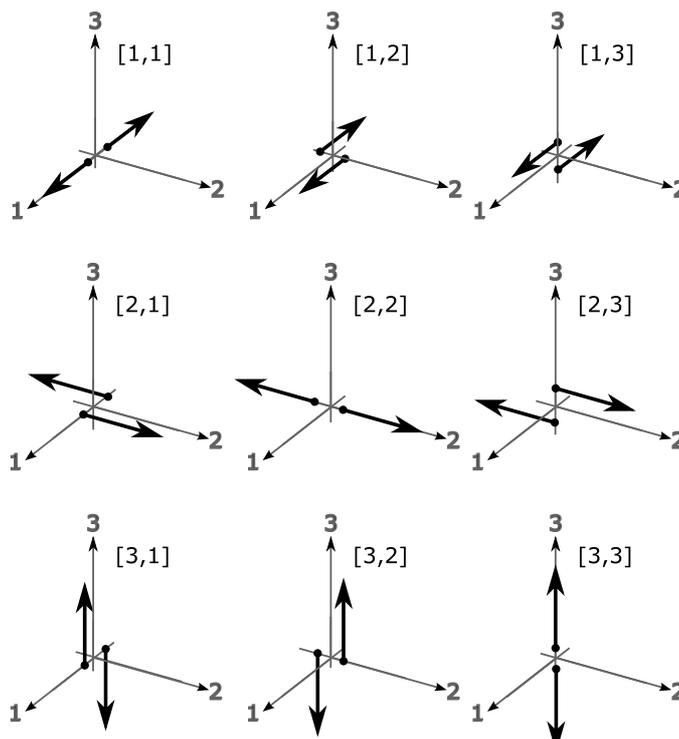

Figure 4.1: The nine couples (M_{ij}) composing the moment tensor for a generally orientated displacement discontinuity after AKI & RICHARDS (2002). The components M_{ij} are representations of forces in the x_i directions with moment arms in the x_j directions.

The diagonal elements M_{11}, M_{22} and M_{33} do not bear a torsional moment, whereas the other elements force couples (M_{ij}, $i \neq j$) are orientated perpendicular to the axes (Figure 4.1) and exert a torque. Due to conservation of angular momentum, the net torque must be zero, hence the torque of M_{ij} must be counterbalanced by M_{ji}. Consequently, the moment tensor must be symmetric (e. g. BACKUS & MULCAHY, 1976) so that only six independent components of the tensor remain:

$$M = \begin{pmatrix} M_{11} & M_{12} & M_{13} \\ & M_{22} & M_{23} \\ & & M_{33} \end{pmatrix} \tag{4.9}$$

Since the tensor M is symmetric, it can be rotated into a principle axis system. In this coordinate system, the moment tensor holds only three orthogonal linear force couples (eigenvectors, M_{11}, M_{22}, M_{33}), whereas all other elements ($M_{ij}, i \neq j$) are zero. The eigenvectors define the principal dipole axes, P (maximum compressional deformation), T (minimum compressional deformation), and B (null axis). For a pure shear fracture M_{ij} is related to the slip vector $\vec{s}$, the fault plane normal $\vec{n}$ and the area of the fault plane A (JOST & HERRMANN, 1989):

$$M_{ij} = \mu A (d_i n_j + d_j n_i) \tag{4.10}$$

where μ is the shear modulus in the source region. Note the symmetry of the slip vector $\vec{s}$ and the fault normal $\vec{n}$ which, for a point double couple, results in the ambiguity of the fault plane and auxiliary plane. The three dipole axes are related to the slip vector $\vec{s}$ and the fault normal $\vec{n}$ (AKI & RICHARDS, 2002):

$$\begin{aligned} \vec{p} &= 1/\sqrt{2}(\vec{n} - \vec{d}) \\ \vec{b} &= \vec{n} \times \vec{d} \\ \vec{t} &= 1/\sqrt{2}(\vec{n} + \vec{d}) \end{aligned} \tag{4.11}$$

A *double-couple* is defined as shear dislocation where the slip vector $\vec{s}$ is perpendicular to the plane normal $\vec{n}$ (no volume changes are allowed). Consequently one eigenvalue of the moment tensor of a double-couple dislocation is zero, the other two eigenvalues are M_0 and $-M_0$ (with M_0, the scalar seismic moment).

$$M = \begin{pmatrix} M_0 & 0 & 0 \\ 0 & -M_0 & 0 \\ 0 & 0 & 0 \end{pmatrix} \tag{4.12}$$

The radiation pattern of a double-couple point source can be calculated (AKI & RICHARDS, 2002). Figure 4.2 shows the two force couples and the two possible fault
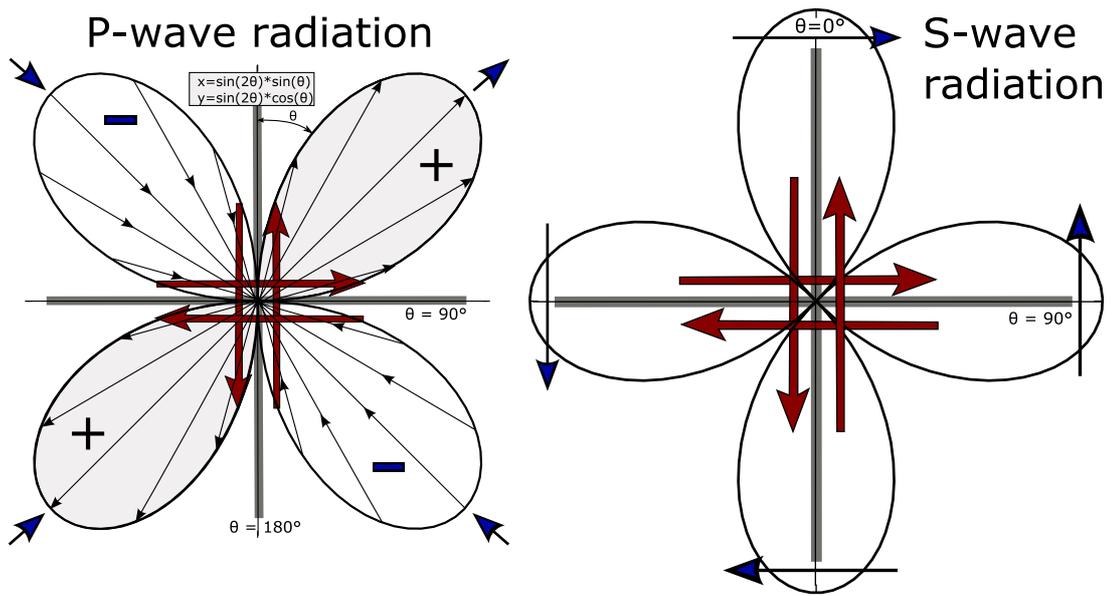
Figure 4.2: Diagrams for the radiation pattern (amplitude, far-field) of a radial (left) and transverse (right) component of displacement due to a double-couple source on a vertical or horizontal rupture plane (x_1x_3 plane). Values are calculated for a plane of constant azimuth. Modified after AKI & RICHARDS (2002).

planes. Compressional and dilatational P quadrants are separated by two orthogonal nodal planes. They are at right angles to one another and intersect along the B axis. One of the nodal planes is the fault surface, whereas the other plane is called auxiliary plane and has no structural significance. The spatial distribution of the compressional and dilatational quadrants in the radiation pattern is exploited to determine the focal mechanism by using first-motion polarities. The nodal and the auxiliary plane cannot be distinguished using seismological data from the event alone. To discriminate the actual fault plane, one has to take additional information into account, e.g. aftershocks preferentially distributed on one plane, observed ground breakages or mapped faults.

The seismic moment M_0 is a scalar quantity to measure the size of an earthquake and is defined by:

$$M_0 = \mu \, u \, A \qquad (4.13)$$

where μ is the shear modulus of the rocks involved in the earthquake, A is the rupture area and u is the average displacement. The seismic moment provides a physical scaling for earthquake whereas magnitudes are based on empirical relations (AKI & RICHARDS, 2002). For a given moment tensor (double couple) M_0 can feasibly calculated by (SILVER & JORDAN, 1982):

$$M_0 = \sqrt{\frac{\sum_{j,k} M_{jk}^2}{2}} = \sqrt{\frac{\sum_i m_i^2}{2}} \qquad (4.14)$$

where m_i are the eigenvalues of the moment tensor M. To compare seismic moment M_0
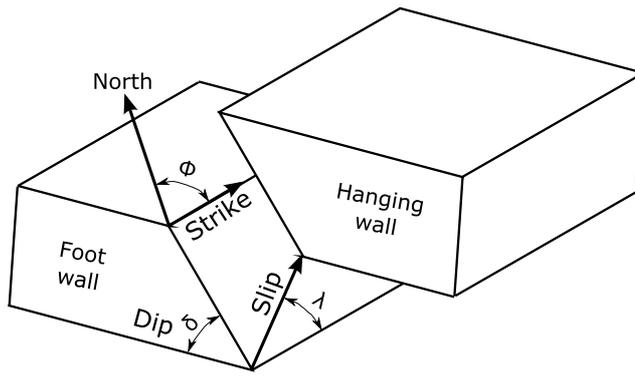
Figure 4.3: Definition of the angles (strike, dip, rake) that describe dislocation on a fault. Strike (ϕ, [0;360°]) is measured clockwise from north, the dip (δ, [0;90°]) is measured down from the horizontal, and rake (λ, [−180°;180°]) is measured between slip and strike on the fault plane (modified after AKI & RICHARDS, 2002).

with moment magnitude M_w the formula from KANAMORI (1977) is used:

$$M_w = 2/3 \ log M_0 \ - \ 10.73, \qquad [M_0] = dyne \cdot cm = 10^{-7} Nm \qquad (4.15)$$

A double-couple source model can be parameterised with the parameters strike ϕ, dip δ, rake λ. For the definition of these values see Figure 4.3. The elements of the moment tensor M_{ij} are related to these parameters by the following relationships (AKI & RICHARDS, 2002):

$$
\begin{aligned}
M_{xx} &= -M_0 \quad (sin \, \delta \, cos \, \lambda \, sin \, 2\phi \quad + sin \, 2\delta \, sin \, \lambda \, sin^2 \phi) \\
M_{xy} &= +M_0 \quad (sin \, \delta \, cos \, \lambda \, cos \, 2\phi \quad +\tfrac{1}{2} sin \, 2\delta \, sin \, \lambda \, sin \, 2\phi) \quad = M_{yx} \\
M_{xz} &= -M_0 \quad (cos \, \delta \, cos \, \lambda \, cos \, \phi \quad + cos \, 2\delta \, sin \, \lambda \, sin \, \phi) \quad = M_{zx} \\
M_{yy} &= +M_0 \quad (sin \, \delta \, cos \, \lambda \, sin \, 2\phi \quad - sin \, 2\delta \, sin \, \lambda \, cos^2 \phi) \\
M_{yz} &= -M_0 \quad (cos \, \delta \, cos \, \lambda \, sin \, \phi \quad - cos \, 2\delta \, sin \, \lambda \, cos \, \phi) \quad = M_{zy} \\
M_{zz} &= +M_0 \qquad sin \, 2\delta \, sin \, \lambda
\end{aligned}
\qquad (4.16)
$$

For a normal fault the rake is positive ($0° < \lambda < 180°$), equivalent the rake is negative for thrust events ($-180° < \lambda < 0°$). Pure strike-slip faults have values of $\lambda = 0°$ (sinistral or left-lateral) or $\lambda = 180°$ (dextral or right-lateral). Figure 4.4 shows the basic fault types and the lower hemisphere projection of the focal sphere onto a single pane ("beach ball").

Separation of the Moment Tensor

Geometric properties of the source are obtained by a decomposition of the moment tensor. It is uniquely decomposed into the isotropic moment M_{ij}^{ISO} and the deviatoric M_{ij}^{DEV} moment tensors (JOST & HERRMANN, 1989, JULIAN et al., 1998):

$$M = M_{ij}^{ISO} + M_{ij}^{DEV} = \frac{1}{3} \underbrace{\begin{pmatrix} tr(M) & 0 & 0 \\ 0 & tr(M) & 0 \\ 0 & 0 & tr(M) \end{pmatrix}}_{M_{ij}^{ISO}} + \underbrace{\begin{pmatrix} \overline{m}_1 & 0 & 0 \\ 0 & \overline{m}_2 & 0 \\ 0 & 0 & \overline{m}_3 \end{pmatrix}}_{M_{ij}^{DEV}} \quad (4.17)$$
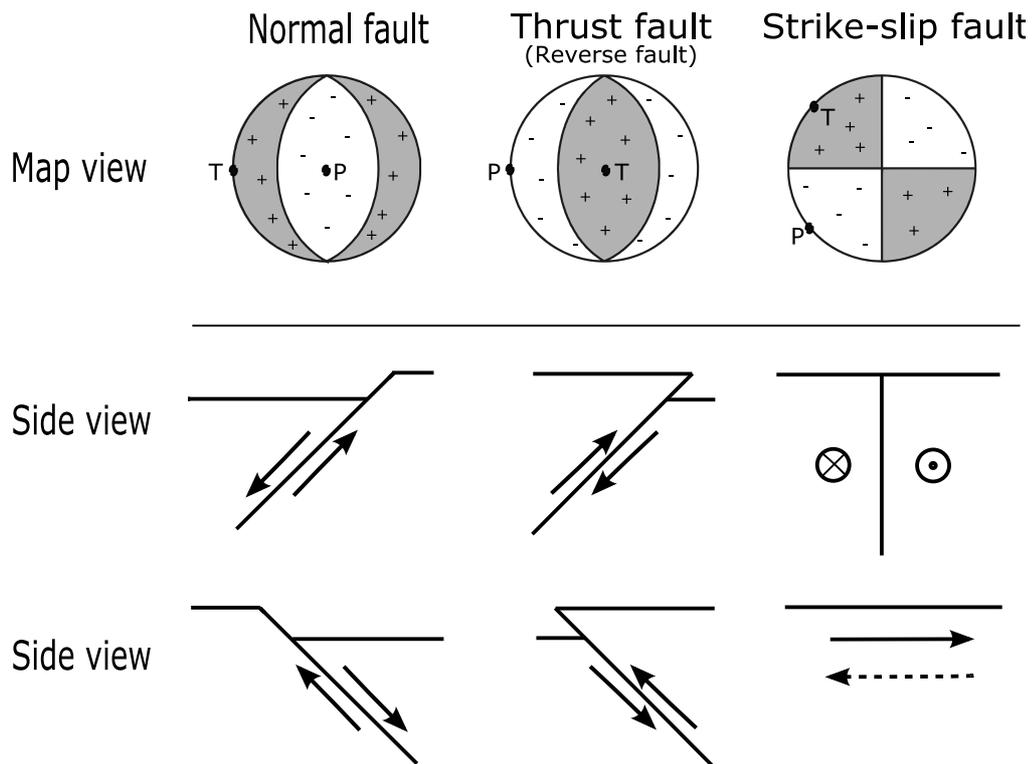
Figure 4.4: Definition of the three basic fault types (normal, thrust and strike-slip fault). The quadrants are coloured black or white according to the first-motion polarity direction. Oblique fault types are a mixture of the types shown in the figure above. (Black: first onset up $(+)$, away from the source, compression; white: first onset down $(-)$, toward the source, tension); Downside: each focal mechanism suggests two possible fault planes. Seismographic evidence alone is not enough to choose the right one. This ambiguity can only be solved with additional information (e. g. local geology or aftershock patterns).

where $tr(M) = m_1 + m_2 + m_3$ is the trace of the moment tensor. M_{ij}^{ISO} represents the expansion or compressional part of the fracture. The eigenvalues $\overline{m}_i$ of the deviatoric tensor are:

$$\overline{m}_i = m_i - \frac{1}{3}(m_1 + m_2 + m_3) = m_i - tr(M) \tag{4.18}$$

Further decomposition of M_{ij}^{DEV} is not unique. We decompose here the deviatoric moment tensor into a best double-couple and a compensated vector dipole (CLVD) since both have the same orientation of their principal axis (JULIAN et al., 1998). To estimate the deviation of the seismic source of a pure double-couple DZIEWONSKI et al. (1981) introduced the parameter ϵ:

$$\epsilon = \left| \frac{\overline{m}_{min}}{\overline{m}_{max}} \right| \tag{4.19}$$

where $\overline{m}_{min}$ and $\overline{m}_{max}$ are the smallest and largest eigenvalue of the deviatoric moment tensor M_{ij}^{DEV}. Because $\sum \overline{m}_i = 0$ for a pure double-couple source $\epsilon = 0$ and $\epsilon = 0.5$ for a pure CLVD. The rates of the best double-couple (DC) and CLVD are expressed in percentages of the deviatoric moment tensor M_{ij}^{DEV}:

$$
\begin{aligned}
DC[\%] &= (1 - 2\epsilon) \quad * \quad 100 \\
CLVD[\%] &= \quad 200 \quad * \quad \epsilon
\end{aligned}
\tag{4.20}
$$

4.2.2   Moment Tensor Inversion

Fault plane solutions were calculated by moment tensor inversion (MTI) utilizing the information contained in the observed waveforms. The components of the displacement u_n at point $\vec{x}$ at time t (general response of the earth to internal forces f_p) can be expressed as a volume integral around the source ξ (AKI & RICHARDS, 2002):

$$u_n(\mathbf{x}, t) = \int \int \int_V G_{np}(\mathbf{x}, t, \xi, \tau) * f_p(\xi, \tau) dV(\xi) \tag{4.21}$$

where $*$ is the convolution symbol, G_{np} is the n-th component of the earth at the station in response to a unit-force excitation in p-direction at the source (Green functions) and ξ, τ are the focal coordinates in space and time. One can show that by applying Taylor expansion around the source position ξ with the precondition that net forces (gravity effects and mass advection (JULIAN et al., 1998)) are neglected, a relation between the displacement field $u_n(x, t)$ and the moment tensor results (AKI & RICHARDS, 2002, DAHM, 1993):

$$u_n(\mathbf{x}, t) = M_{pq}(t) * \frac{\partial}{\partial \xi_q} G_{np}(\mathbf{x}, t, \xi, \tau)|_{\xi_0} \tag{4.22}$$

the second term on the right-hand side is now separated in the near-field and the far-field components. Therefore we take the spatial derivation of G_{np} with respect to the source

coordinate (e.g. RÖSSLER, 2006):

$$\frac{\partial}{\partial \xi_q} G_{np}(\mathbf{x}, t, \xi, \tau) = \frac{\partial G_{np}}{\partial x_i} \frac{\partial x_j}{\partial \xi_q} + \frac{\partial G_{np}}{\partial t} \frac{\partial t}{\partial \xi_q} \tag{4.23}$$

the second term of the right-hand side decays with distance r from the source as r^{-1}, the first term decays with higher order (DAHM, 1993). Therefore, first term on the right can be neglected in the far-field ($r > \lambda/(2\pi)$). Then, equation 4.23 becomes

$$\frac{\partial}{\partial \xi_q} G_{np}(\mathbf{x}, t, \xi, \tau) \approx \frac{\partial G_{np}}{\partial t} \frac{\partial t}{\partial \xi_q} = \dot{G}_{np} p_q \tag{4.24}$$

where p_q is the slowness vector. The far-field approximation of equation 4.22 with the assumption that all components of the moment tensor share the same time dependence ($M_{pq}(t) = h(t) M_{qp}^0$) now reads

$$
\begin{aligned}
u_n(\mathbf{x}, t) &= M_{pq}^0 \, h(t) * \dot{G}_{np}(\mathbf{x}, t, \xi, \tau) \, p_q \\
&= M_{pq}^0 \, \dot{h}(t) * G_{np}(\mathbf{x}, t, \xi, \tau) \, p_q
\end{aligned}
\tag{4.25}
$$

where $h(\tau)$ is the source time function ($h(0) = 0, h(\infty) = 1$). The time it takes $h(t)$ to reach the maximum is called the rise time. If the period of the observed waves is much larger than the source duration G_{np} can expanded around the source time centroid τ_0. Equation 4.25 reads now (RÖSSLER, 2006):

$$u_n(\mathbf{x}, t) = M_{pq}^0 h(\infty) \dot{G}_{np}(\mathbf{x}, t - \tau_0) p_q + M_{pq}^0 h(\infty) \dot{G}_{np}(\mathbf{x}, t - \tau_0) p_q \int_0^\infty h(\tau)(\tau - \tau_0) d\tau + ... \tag{4.26}$$

τ_0 is chosen so that the integral on the right side vanishes (DAHM, 1993). Neglecting terms of higher order results in the equation:

$$u_n(\mathbf{x}, t) = M_{pq}^0 \, G_{np}(\mathbf{x}, t; \xi, \tau_0) \, p_q \tag{4.27}$$

The equation provides a linear relation between the displacement field and M_{pq}^0. If sufficient observations are available and the medium that determines the Green functions is appropriately known M_{pq}^0, τ_0 and ξ^0 can be determined (DAHM, 1993). In the time domain, the alignment of the synthetic and observed seismograms is often difficult. Small time shifts already result in different moment tensor solutions. This problem is solved here by fitting the seismograms in the (squared) frequency domain. On the other hand, a solution obtained in the frequency domain loses information about phases and is, therefore, ambiguous inasmuch as pressure and tension axis cannot be distinguished (CESCA et al., 2006). This ambiguity of the compressional/tensional sectors is feasibly resolved by adding information about first-motion polarities of onsets with high-quality. In the frequency domain, the problem formulated in equation 4.27 is not linear. Therefore, the solu-

tion is achieved by linear approximation (BRUHN, 2003, page 23) and by searching for the global minimum in the parameter space. This search combines a grid search and a gradient method to find the minima. While for larger events moment tensor inversion is nowadays calculated automatically (e.g. USGS, SIPKIN (1982), SIPKIN & ZIRBES (2004); Harvard CMT, DZIEWONSKI et al., 1981), the determination of reliable MTI for small events (with shorter wavelengths) is still a challenge. However, MTI were recently successfully applied to body waves from local events with magnitudes smaller than M_w=4.0 (SCHURR & NÁBĚLEK, 1999, STICH et al., 2003, CESCA et al., 2006, RÖSSLER et al., 2007). In this study amplitude spectra from body waves for selected events were used (magnitudes of between 2.8 and 3.8 M_w), following the procedure outlined by DAHM et al. (1999) and CESCA et al. (2006). Small earthquakes radiate waves with sufficient signal-to-noise ratio at relatively high frequencies (>0.5 Hz) only. Preprocessing prior to MTI includes resampling (20 Hz), restitution of the recorder response, quality control and rotating the traces into the focal coordinate system.

4.2.3 Focal Mechanism from First-Motion Polarities

Focal mechanisms for the stronger events in the Benioff zone were determined from first-motion polarities. This classical method uses the first-motion polarities (up and down) of P onsets which are compared with the far-field radiation pattern of a point source (Figure 4.2). A good azimuthal coverage of observations around the focal sphere is mandatory to determine a reliable focal mechanism. In this study the calculation was carried out with the programme FPFIT (*Fault Plane FIT*) according to the procedure described by REASENBERG & OPPENHEIMER (1985). FPFIT finds the double-couple fault plane solution (source model) that best fits a given set of observed first-motion polarities for an earthquake. For each first-motion polarity of an event, the estimated ray azimuth (seen from the source) from north and its inclination above horizontal (take-off angle measured from the source) are given into the inversion. The inversion is accomplished through a two-stage grid search procedure that finds the source model minimising a normalised, weighted sum of first-motion polarity discrepancies (REASENBERG & OPPENHEIMER, 1985).

Other methods for the determination of the focal mechanism are additionally using the absolute S or P amplitudes and/or ratios of amplitudes (P/SV) (e.g. SNOKE et al., 1984). Due to the inhomogeneous station subsurface structure (site effects) in the amphibious network and the small amount of S observations of the offshore stations, these methods were not applied in this study.

4.3   The Focal Mechanism Stress Inversion Method

For a given group of focal mechanisms one can calculate the stress field for different regions by an inversion for the stress field for groups of earthquakes (in this study for the Benioff zone and the continental part of the working area). Tectonic forces accumulate stress in the lithosphere. When the stress exceeds the material strength, the media fails and an earthquake occurs. The direction of slip of the event is determined by the stress field and preexisting zones of weakness. The regional stress field is therefore connected to the orientation of focal mechanisms. For the inversion of the stress field the method from MICHAEL (1984, 1987) was applied which is based on the method of GEPHART & FORSYTH (1984). For a detailed treatment of focal mechanism stress inversion the reader is referred to GEPHART & FORSYTH (1984), MICHAEL (1984, 1987), GEPHARD (1990) and RUDLOFF (1998). Two main assumptions are made:

- The stress tensor is uniform in time and space in the crustal volume investigated.
- On each fault plane slip occurs in the direction of the resolved maximal shear stress.

To determine the unknown parameters, the difference between the prediction of the stress field and the observations (the two conjugate planes per focal mechanism) need to be minimised for all events. The error function (misfit) $E(\sigma)$ is defined as:

$$E(\sigma) = \sum_{i=1}^{n} min(e_i^1(\sigma), e_i^2(\sigma)) \tag{4.28}$$

where σ is the stress tensor being tested, n is the number of fault plane solutions, $e_i^1(\sigma)$ and $e_i^2(\sigma)$ are the fit functions for nodal plane 1 and 2 for a given stress tensor σ. GEPHART & FORSYTH (1984) used as fit function e_i the minimum rotation angle around any arbitrary axes that brings the fault plane geometry into coincidence with a stress field. The method described by MICHAEL (1987) differs in the fit functions e_i, which solely considers rotations around the normal vector of the fault plane. Both methods lead to similar results (MICHAEL, 1987); both methods were applied to the stress tensor inversion using the software packet ZMAP (WIEMER & ZÚÑIGA, 1994, WIEMER, 2001). In order to minimise the error function $E(\sigma)$ a grid search over the focal sphere was performed, at first with a 90° variance and 10° spacing (approximate method), and then with a 30° variance and 5° spacing (WIEMER, 2001). The solution stability was determined by a bootstrap method which was carried out 2000 times for each inversion. Since the results of the methods only differ slightly (without figure) and the method of MICHAEL (1984, 1987) provides a more appropriate estimate of uncertainty (HARDEBECK & HAUKSSON, 2001), only the solutions of the method described by MICHAEL (1987) are shown in this work.

4.4   Calculation of Adopted Local Magnitudes

Local magnitudes (M_l) were calculated by using an automated procedure based on the RICHTER (1958) magnitude definition:

$$M_l = log\ A \quad - \quad log\ A_0 \tag{4.29}$$

where A is the zero-to-peak amplitude. The term $-log\ A_0$ corrects for the different epicentral distances and is scaled so that for an earthquake of $M_l = 3$, at a distance of 100 km, the zero-to-peak amplitude A becomes 1 mm when measured on a Wood-Anderson seismograph (RICHTER, 1958). BAKUN & JOYNER (1984) determined the term $-log\ A_0$ from amplitudes of Wood-Anderson seismograms for central California, and established the relation for M_l:

$$M_L = log\ A \quad + \underbrace{[\,n\ log(R/100) \quad + K\ (R\ -\ 100\ ) + 3\,]}_{Distance\ correction\ factor} \tag{4.30}$$

where R is the hypocentral distance, K is an attenuation coefficient and n is the geometrical spreading factor. BAKUN & JOYNER (1984) achieved the best fit to the Richter's relation with the values n=1 and K=0.00301. In this study the local magnitudes were calculated by applying the formula and coefficient values from BAKUN & JOYNER (1984). The best approach would be to determine the coefficients n and K for southern Chile by using the local seismicity data, but the size of the local database is insufficient. Therefore the coefficients from central California (BAKUN & JOYNER, 1984) were adopted for the determination of M_l.

Chapter 5

Seismicity and Structure

5.1 The Minimum 1-D model

There was no local velocity information available for the working area. To obtain precise hypocentre localisations, an adequate local velocity model for the working area is crucial. A standard velocity model (e. g. AK135, KENNETT et al., 1995) would produce large location errors and RMS residuals when locating the events. Hence, arrival time data was used for a joint inversion of 1-D velocity structure, station delays and hypocentral coordinates (Section 4.1.1).

In the inversion with VELEST (KISSLING et al., 1995), only events with more than 8 onset times, containing at least 4 S wave observations, and a GAP (= largest azimuth range with no observations) $\leq 180°$ were included. This reduced the number to 98 well-constrained events with 1.287 P and 1.044 S-wave travel time observations. For computational reasons the elevation (depth) of the OBS/OBH stations was set to sea level, and the resulting travel time error compensation is accomplished by the simultaneous inversion of station correction terms (HUSEN et al., 1999). First a minimum RMS 1-D P-wave velocity model was inverted by using a constant v_p/v_s ratio of 1.77 which was derived from Wadati diagrams (Figure 5.1). A wide range of initial P-wave velocity models (indicated in Figure 5.2)
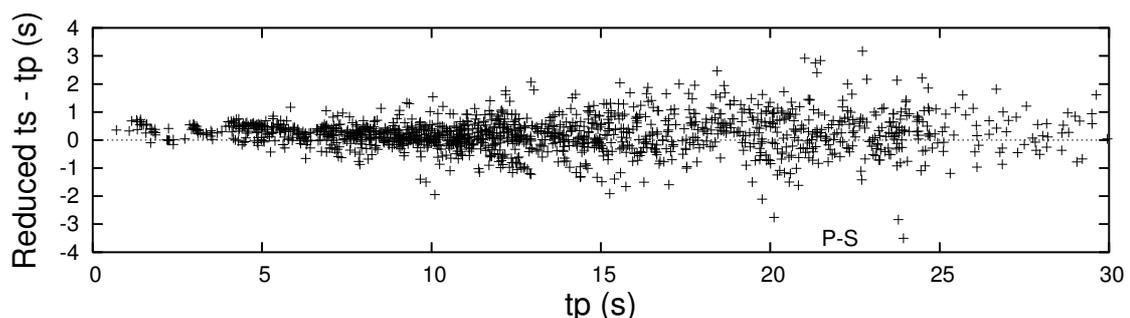

Figure 5.1: Reduced Wadati diagram derived from P and S wave travel times with high qualities. The diagram is reduced for a v_p/v_s ratio of 1.77.

Table 5.1: The minimum 1-D velocity model

depth km	v_p km/s	v_s km/s	v_p/v_s
-2 – 1	5.09	3.15	1.62
1 – 5	5.65	3.16	1.79
5 – 10	5.72	3.34	1.71
10 – 15	6.38	3.80	1.68
15 – 23	6.97	3.87	1.80
23 – 30	7.32	4.01	1.83
30 – 39	7.82	4.41	1.77
39 – 45	7.94	4.66	1.70
45 – 60	7.98	4.66	1.71
60 – 130	8.85	4.81	1.84

was used to investigate the quality and stability of the final minimum P wave velocity model. The minimum 1-D S-wave velocity model was determined by an additional series of inversions with different initial v_p/v_s ratios according to HUSEN et al. (1999).

In the upper crust P-wave velocities between 5.1 km/s and 5.8 km/s are estimated, which steadily increase to 7.8 km/s at 30 km depth (Figure 5.2 and Table 5.1). Velocities of 7.8 km/s and more are already found at 30 km depth, which are at a shallower level than the ones to the north at 38°S, where this transition is found at a depth of 55 km (BOHM et al., 2002, HABERLAND et al., 2006). The velocity layers below 60 km are poorly resolved because of the reduced seismicity in greater depths. Due to near vertical ray paths at shallow depths, the uppermost layers down to 15 km depth are not properly constrained. Inverted station delay times are smaller than 0.5 s, taking into account the static corrections introduced by the station elevation (Figure 5.3). All earthquakes with more than 8 observed onset times were relocated with the new minimum 1-D velocity model resulting in 245 well located events. The distribution of the hypocenters is discussed in Section 5.3. From the 364 detected local events 322 could be located. The properties of the dataset with all 322 available events relocated with the minimum 1-D velocity model in single event mode of velest is shown in Figure 5.4. To determine the pick accuracy and to find outliers, travel time residuals for different pick weights were calculated (Figure 5.5).
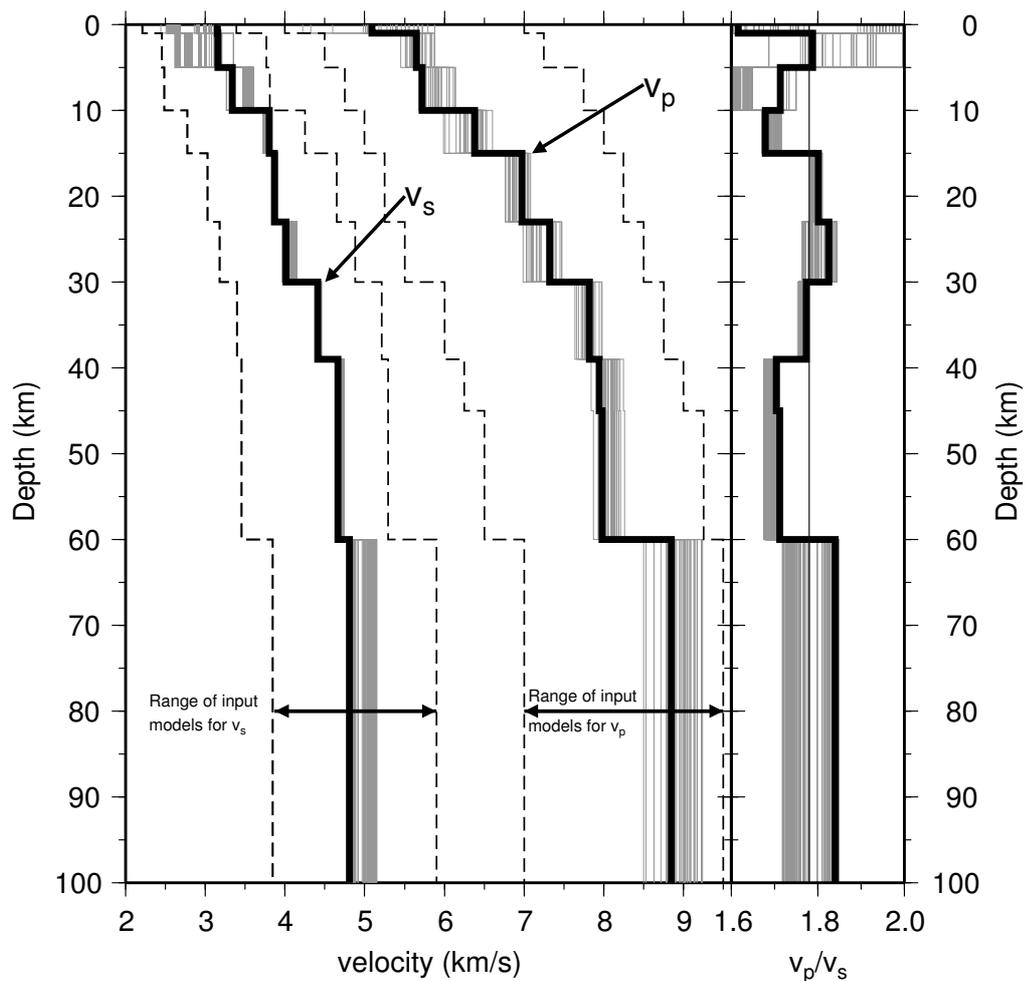
Figure 5.2: Resulting minimum 1-D velocity model (LANGE et al., 2007). Models that fit the data equally well (best 3%) are plotted in grey. Range of input models for P and S velocity covering the velocity space between the two dashed lines. On the right, final v_p/v_s ratios are shown.
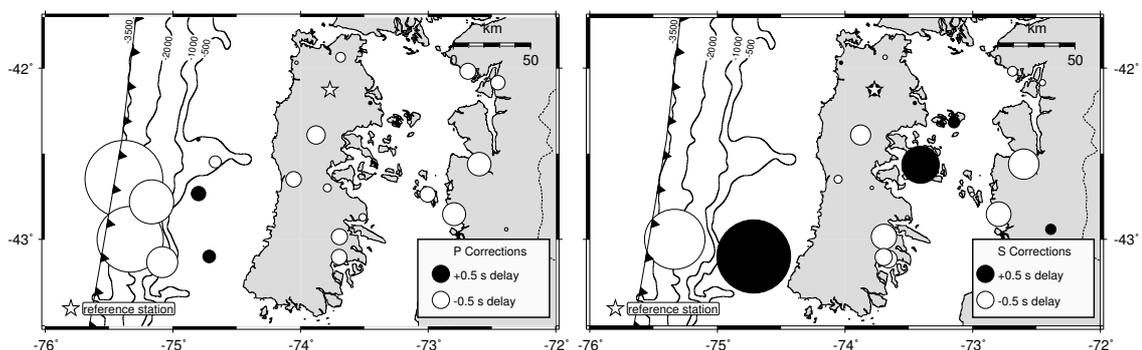
Figure 5.3: Station corrections for P-wave (left) and S-wave (right) onsets. The reference station is marked with a star and only station corrections with more than 15 P onsets are shown. The high negative station corrections near the trench are due to computational reasons. The elevation (depth) of the OBS/OBH stations was set to sea level, and the resulting travel time error compensation is accomplished by the simultaneous inversion of station correction terms (HUSEN et al., 1999). Bathymetry according to SMITH & SANDWELL (1997). Modified after LANGE et al. (2008)
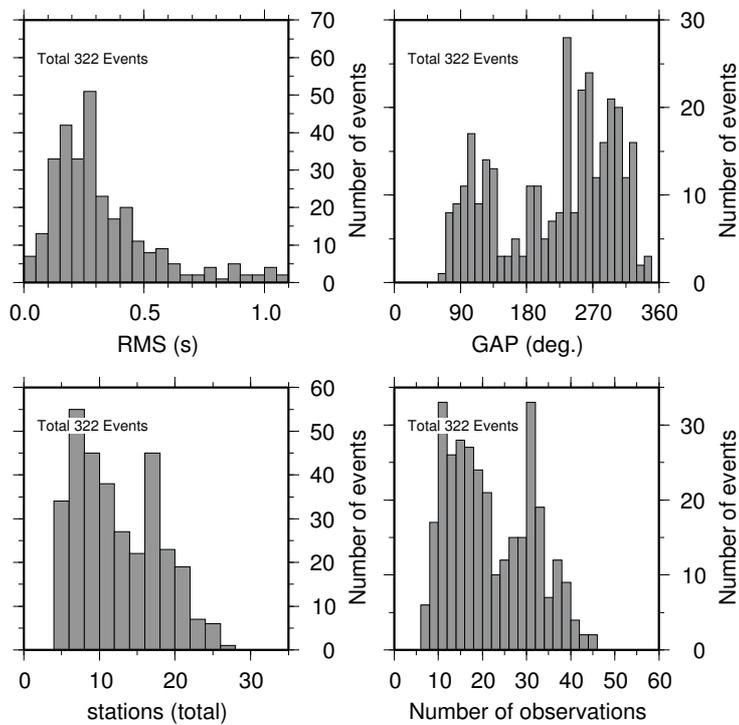
Figure 5.4: Histograms of number of RMS (upper left), GAP (upper right), amount of observed stations (down left) and number of observations (down right) for the hypocentres located with the minimum 1-D model.
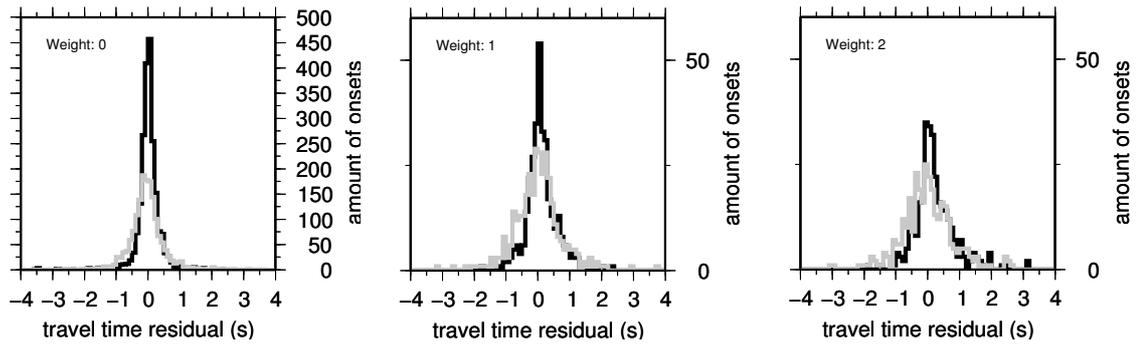
Figure 5.5: Calculated travel time residuals (with minimum 1-D velocity model) from the onset database for different pick qualities (weights) and phases (P:black; S: grey).
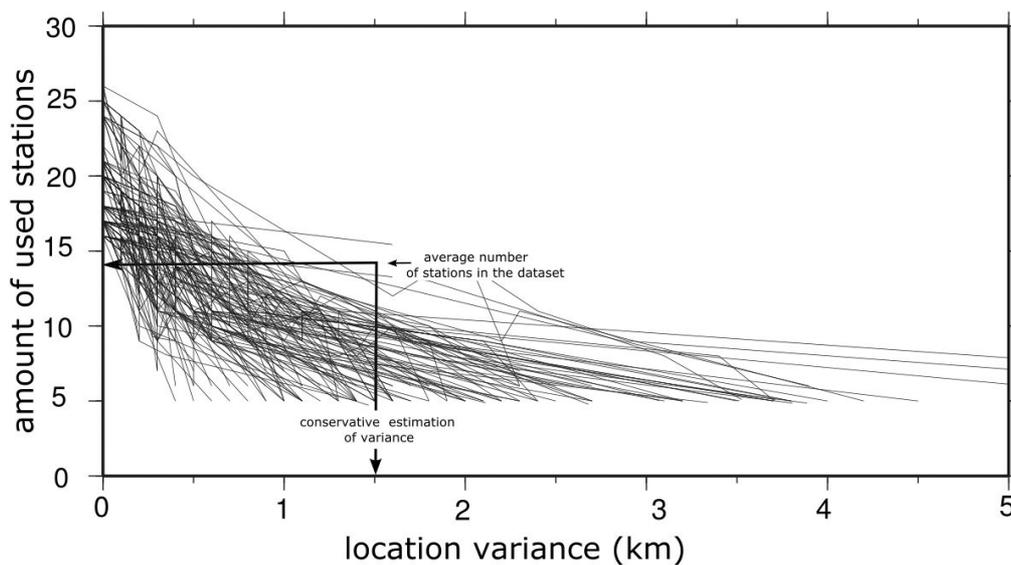
Figure 5.6: Using reduced subsets of stations for relocating single events to estimate location accuracy (Jackknife test). Amount of used stations (for all events introduced in the joint inversion) versus location variance. The location was carried out by using the single-event mode of VELEST.

In order to estimate the accuracy of the obtained hypocentres (GAP≤180°), "jackknife tests" were performed , i. e. subsets of observations (picks) for certain (stronger) events were selected randomly and relocated with the final velocity model (single-event mode localisation in VELEST). By using reduced subsets of 14 stations per event (which is the average number of stations per event of the dataset used in the simultaneous inversion), one finds a maximum standard deviation of 1.5 km which is assumed to be representative for the hypocentre accuracy (Figure 5.6).

Stability and robustness of the resulting minimum 1-D model was tested following the procedure outlined by KISSLING et al. (1994) which uses systematic and random shifting of the hypocentres and re-introduces the "disturbed" locations again in the location routine (hypocentre, velocity model and station corrections). The dislocation of the hypocentres plotted in Figure 5.7 yields a standard derivation of 1.5 km for the horizontal coordinates
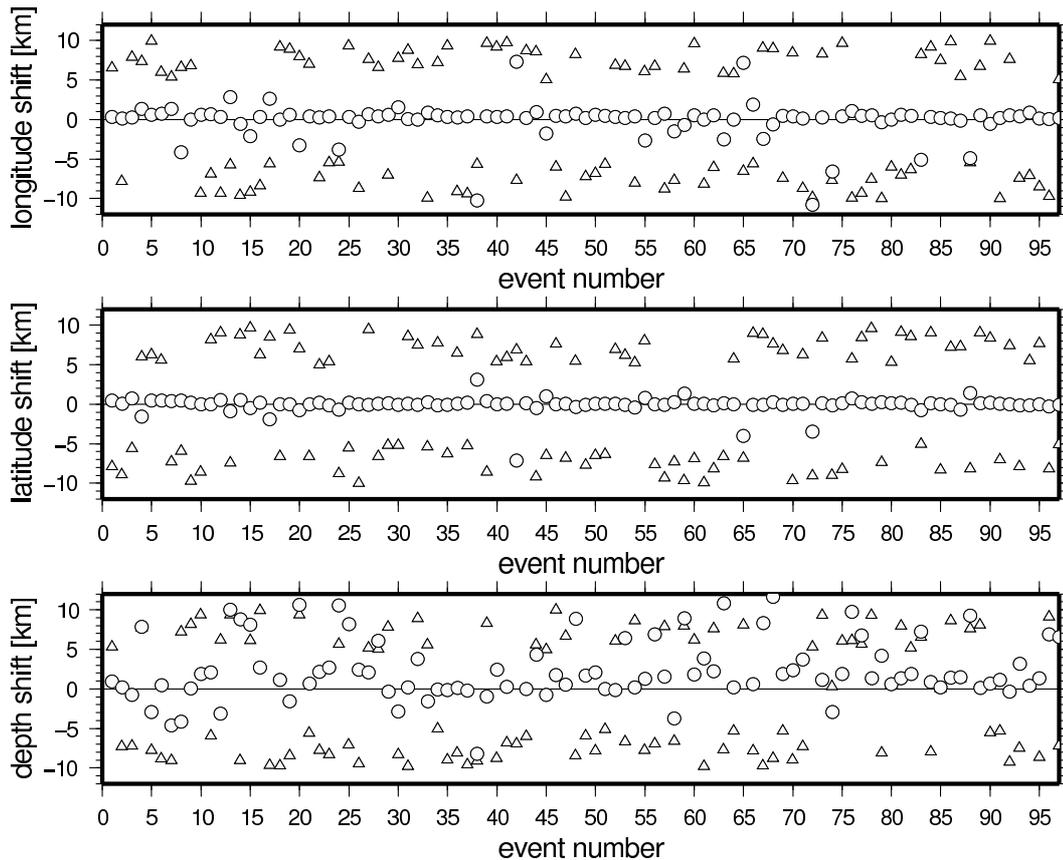
Figure 5.7: Dislocation of hypocentres randomly shifted (triangles) between 5 and 10 km and reintroduced into the coupled inversion for hypocentres, velocity model and station corrections. Circles denote the relocalised hypocentres after the shifting. Standard deviation for horizontal dislocations (2 km) are much smaller than depth dislocations (4 km).

and 5 km for the depth. These small values suggest that the inverted velocity model is a global minimum of the inversion. The relative higher standard derivation of the dislocations, compared to the jackknife test, is the result of using joint inversion for the calculation of the dislocations, while the events for the jackknife test were relocated by using the single-event of VELEST.

5.2   Local Magnitudes

Local magnitudes (M_l) based on the formula and coefficients from BAKUN & JOYNER (1984) (Section 4.4) were determined. The automated magnitude calculation was elaborated by A. Rietbrock using the software package GIANT (RIETBROCK et al., 1998). First, the maximum peak-to-peak amplitude of a time window (2 seconds) after the picked P onsets is determined from raw waveform data. Second, the period is estimated using the time difference between the two maximum amplitudes. The peak-to-peak amplitude (taking into account the gain) for the calculated period of the stations (1 Hz Mark L4-C) is used to transfer the amplitude into the corresponding amplitude response of a Wood-Anderson Seismometer (e. g. PEZZO & PETROSINO, 2001). The standard Wood-Anderson transfer function damping factor 0.8 and the frequency of oscillation (1.25 Hz) was applied (RICHTER, 1958). Finally, for each amplitude, a magnitude is calculated according to equation 4.30. Then all magnitudes for one event are listed and a mean magnitude value is derived by summing up all station magnitudes and dividing it by the number of participating stations (e. g. SOBIESIAK, 2004). Due to unknown transfer functions of the OBS/OBH stations, only land stations could be used for the determination of M_l.

A total of four events located by the network are also listed in the NEIC catalogue (WWW-PDE, 2007). The three magnitude differences (0.43, 0.05 and -0.41) are generally close to magnitudes in the NEIC catalogue, taking into account that the comparison of the two catalogues is based on different magnitude scales. The earthquake catalogue from the Servicio Sismológico, Universidad de Chile (http://ssn.dgf.uchile.cl/) which includes local magnitudes has three events in common with our catalogue and allows a more conclusive comparison of the magnitudes. The magnitudes are close to each other (0.43, 0.22 and -0.11 M_l) indicating a reliable estimation of M_l.

The magnitude range of the earthquake catalogue is between 0.5 and 5.1 M_l. The highest magnitudes are found east of the Chiloé Island coast (Figure 5.8). All but one of the Benioff zone events below 45 km depth have magnitudes smaller than 3, equally all but one of the events below the trench show only small magnitudes (M_l<3). The continental side of the working area is characterised by different clusters of shallow events with magnitudes of up to 3.8 M_l. In the next section a detailed discussion about the distribution of hypocentres and their magnitudes is carried out.
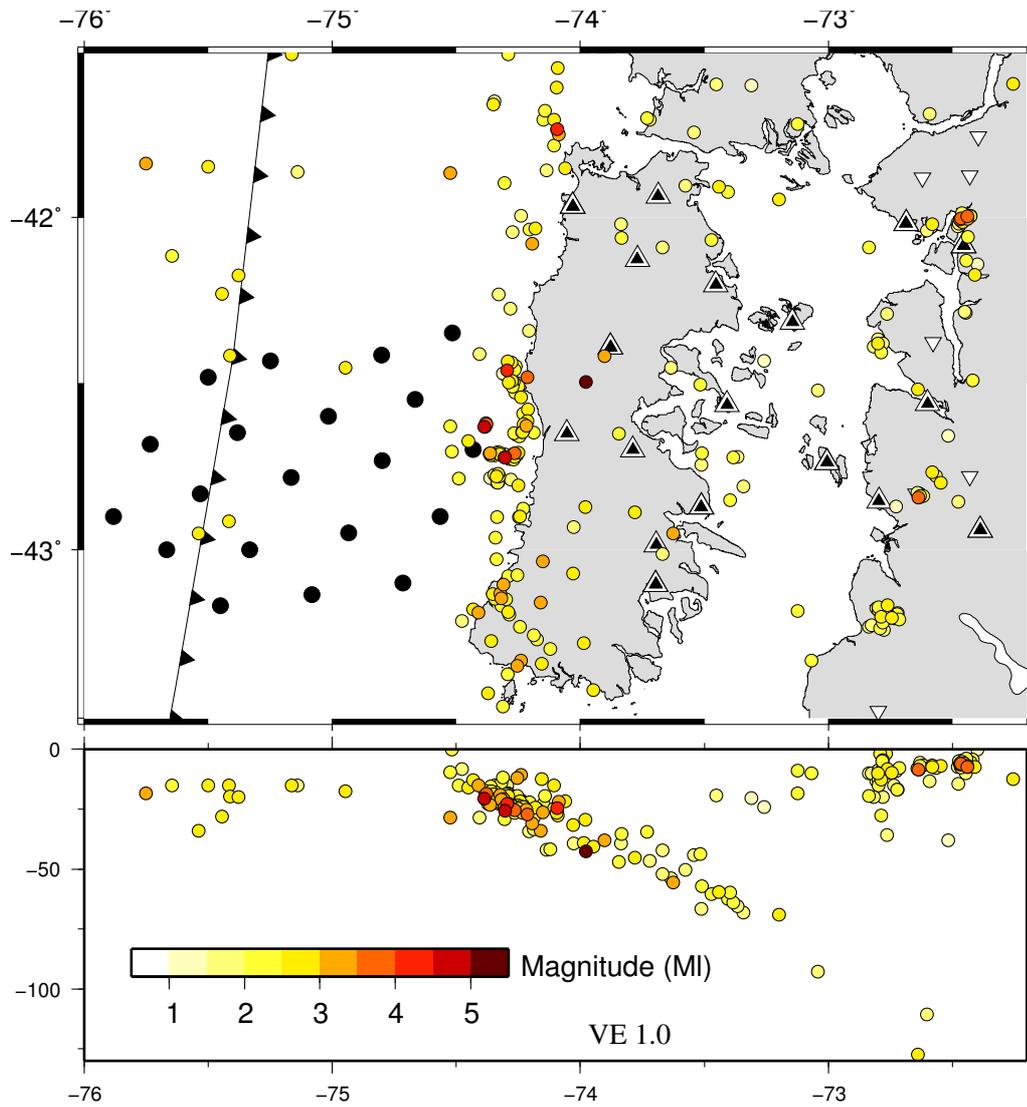
Figure 5.8: Distribution of local magnitudes (M_l). Magnitudes are in a range between 0.51 and 5.11 M_l. Seismic stations are indicated by black triangles and circles. Volcanoes are indicated with inverted white triangles.

5.3   Seismicity and Geometry of the Slab

The observed seismicity during the 11-month observation period is clearly localised in different regions of the subduction zone between 12 and 70 km depth. The seismicity pattern can be roughly divided into five regions, which will be described along a profile crossing the trench from west to east following the subducting Nazca plate (see also numbers in Figure 5.9).

1.) Seismicity at the trench is located between 12 and 34 km depth, which is well below the oceanic crust and presumably associated with mantle processes. Although a dense OBS/OBH network was in place, no events larger than $M_l = 3.3$ and no seismicity associated with the oceanic crust were found. Events at this depth rage below the trench were described beneath the trench in other subduction zones (DESHON et al., 2003, OBANA et al., 2005). Due to reduced P velocities derived from refraction data between the outer rise and the trench, CONTRERAS-REYES et al. (2007) suggest alterations due to hydration for the area directly continuing west of the network.

2.) Directly east of the trench a 70 km wide zone is observed in which only one event (M_l=2.5) has been recorded. Similar sparse seismicity is also documented in the NEIC PDE catalogue (Figure 1.1), thus suggesting long-term aseismic behaviour of this part of the seismogenic zone, associated, however, with a large slip ($\sim$17 m) during the 1960 Valdivia earthquake (BARRIENTOS & WARD, 1990).

3.) Most events of the dataset occurred below the western shore line of Chiloé Island at a depth range of between 12 and 30 km depth (Figure 5.10). The observed seismicity in this region is mainly constituting of four larger events (M_l 4.0–4.4) and their associated aftershock sequences. These earthquakes are predominantly thrust-type events as indicated by fault plane solutions. The epicentres mainly follow the curved course of the coast line (Figure 5.10). While the western upper edge of this increased seismicity zone is clearly defined, the eastern and lower one is much more diffused. However, there is a pronounced drop in the seismicity rate below 30 km depth as seen in the depth-frequency histogram (Figure 5.9). The changeover from seismic to aseismic takes place in a coastal-parallel strip of less than 25 km width (Figure 5.10). Calculations of the distance between the epicenter locations of the events shown in Figure 5.10 and the curved coast lead to a mean distance of 8.7 ($\pm$5.0) km for all events and 6.4 ($\pm$3.4) km for events deeper than 22 km, respectively (Figure 5.11). Possible explanations for this finding will be discussed in Section 7.2.

4.) Below 30 km the subducting Nazca Plate is depicted by seismicity down to a depth of 70 km. At 42 km depth a thrust event with M_l=5.1 is located (Figure 5.8). However, all other events below 30 km are below M_l=2, with exception of a M_l=2.9 thrust
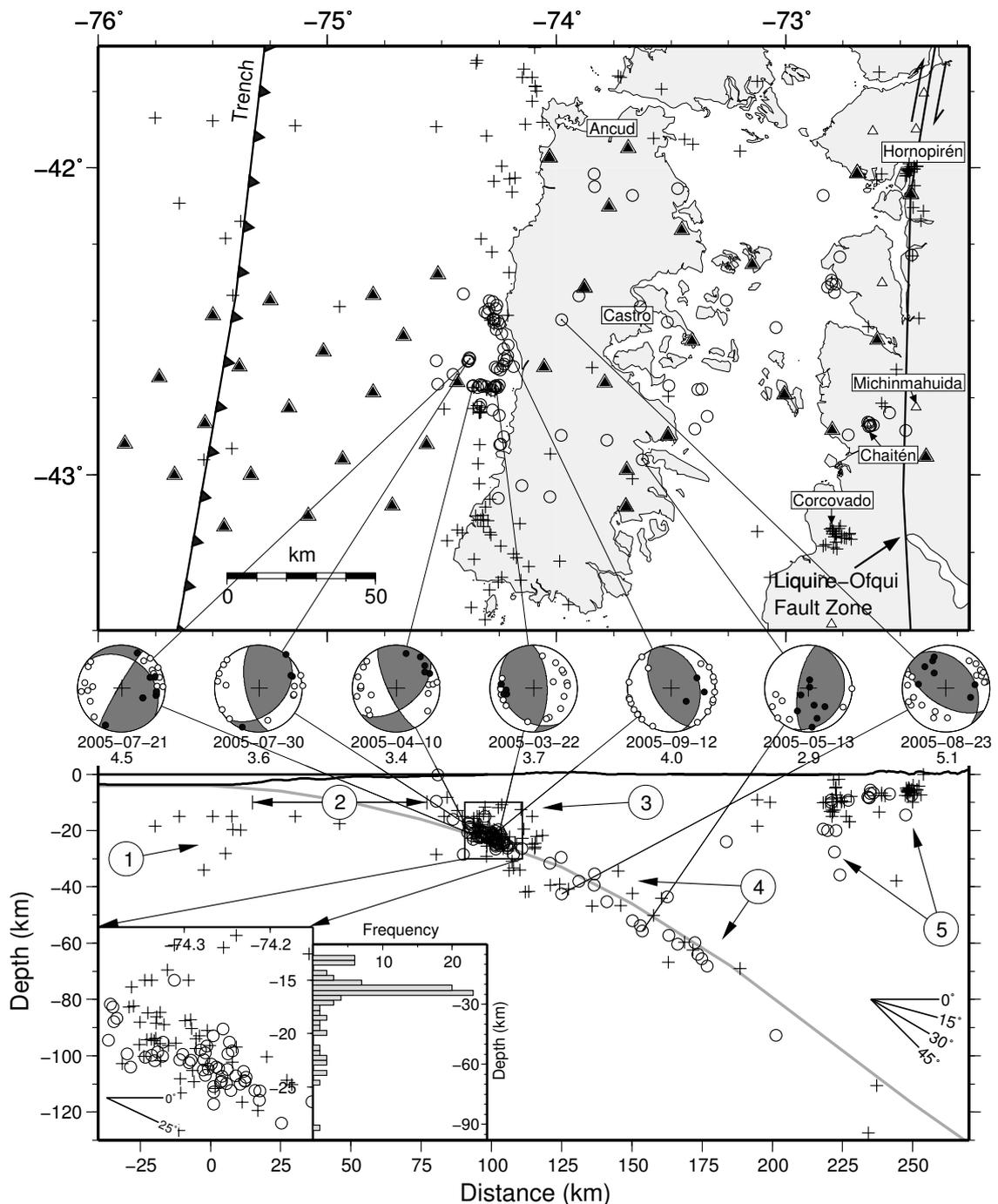
Figure 5.9: Distribution of located earthquakes modified after LANGE et al. (2007).
Top: Hypocentres with GAP≤180° (GAP>180°) are depicted by circles (crosses).
Black triangles mark seismic stations, volcanoes are marked by upright white trian-
gles. Middle: Fault plane solutions (lower hemisphere plot) based on first-motion
polarities and labelled with date and magnitude. Bottom: Hypocentres projected
onto a E-W vertical cross-section clearly show the inclined Wadati-Benioff zone
and shallow crustal seismicity. The light grey line indicates interpreted possible top
of subducting slab. Inlay plots show a close-up view of the seismicity beneath the
coast and the depth-frequency distribution of events within (GAP≤180°) the net-
work. Numeration refers to the consecutive numbered text in this section.
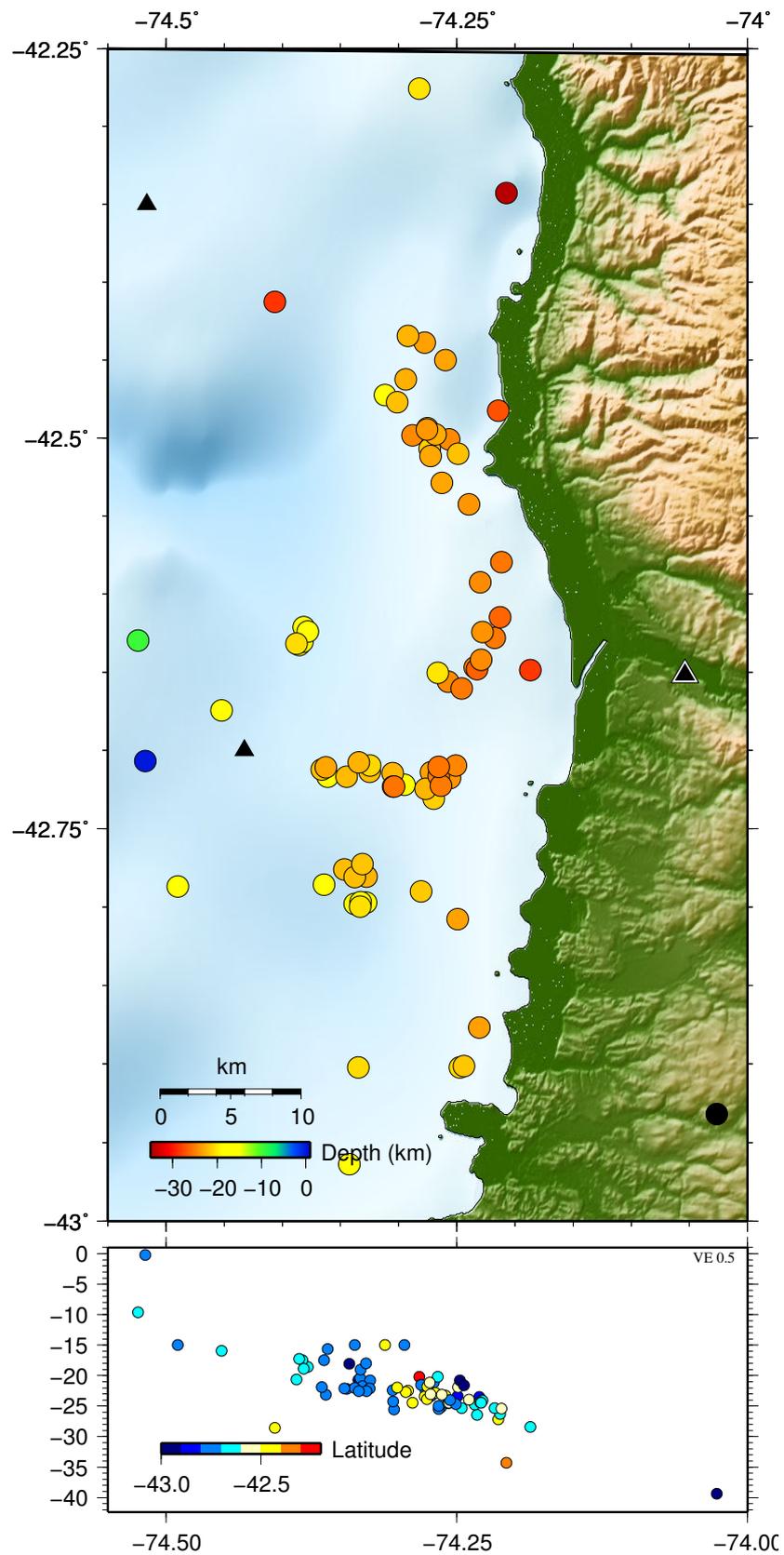
Figure 5.10: Close-up view of the seismicity near the coast. The epicentres mainly follow the curved course of the coast line. See text for more information.
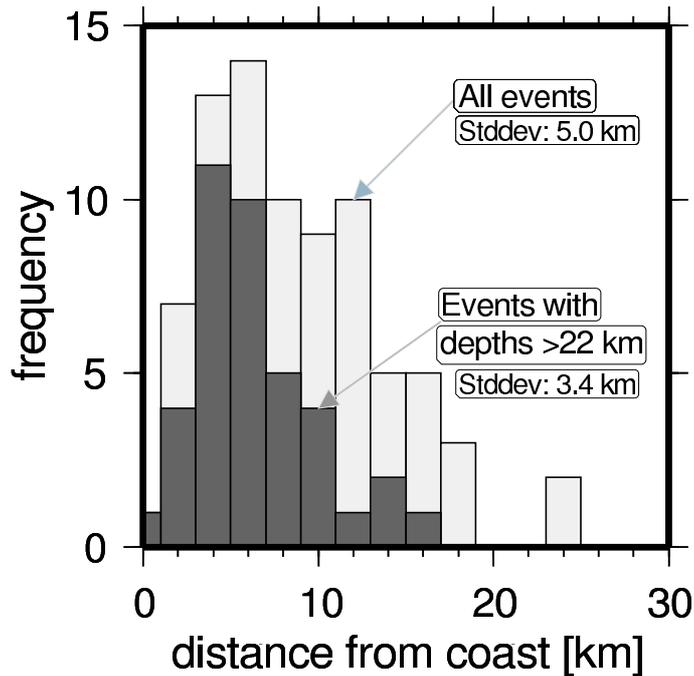
Figure 5.11: Histogram of the epicenter–coast distances of the events shown in Figure 5.10. The mean distances for all events to the coast is 5 ($\pm$5.0) km; the deeper events (<22 km) are located within a strip with mean distances of 6 ($\pm$3.4) km to the coastline of Chiloé Island.

event at 55 km depth. Linear regression (Figure 5.12) of events with GAP$\leq$180° and depths below 30 km (projected on a west-east cross-section) yields an inclination of 33($\pm$3)° of the Wadati-Benioff zone (WBZ) (30°$\pm$1° for depths$\geq$15 km, Figure 5.12).

5.) High seismicity with events of up to M_l 3.8 is found within the continental crust along the active volcanic arc (<20 km). The seismicity in this region is localised in several spatial clusters, two of which are closely located to the volcanoes Corcovado and Chaitén (Figure 5.9). One cluster of 33 events is located 10 km south of Hornopirén with depths of less than 10 km along the LOFZ. A detailed description and discussion of these shallow, crustal events including their focal mechanisms is carried out in Section 6.1.
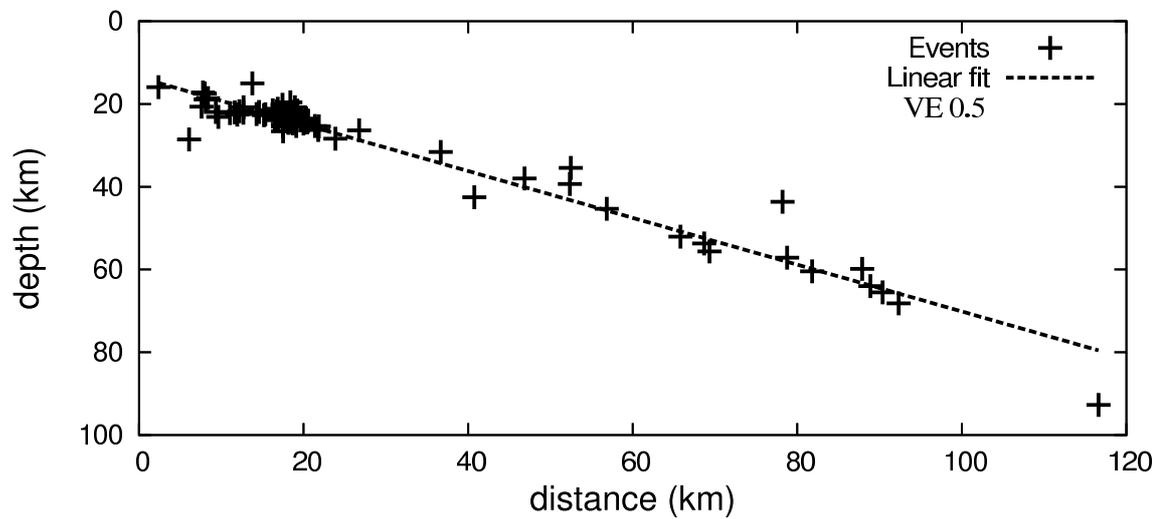
Figure 5.12: Linear regression of the events within the Benioff zone (GAP≤180°, depth≥15km) yields an inclination of 30±1°.

5.4   2-D Velocity Structure from Local Earthquake Tomography

The 1-D inversion described in Section 5.1 was performed in order to obtain an appropriate initial minimum 1-D model which is the starting model for the 2-D inversion. The importance of the careful selection of the minimum 1-D model was described by various authors (KISSLING, 1988, EBERHART-PHILLIPS, 1990, KISSLING et al., 1994, GRAEBER & ASCH, 1999). For the 2-D inversion with SIMULPS (EVANS et al., 1994) events with at least 8-P and 4-S observations were used. Apart from that, stations with less than 15 high-quality observations, OBS/H with high station residuals or dubious time corrections were not included in the inversion in order to be sure that all the observed travel times are accurate. The remaining stations are exclusively located east of the trench. After having checked the the stability of the 2-D inversions exclusively included events of GAP≤180°, events with GAP≤200° were included in the inversion which results in a dataset consisting of 117 events. The relaxation of the GAP criterion to 200° did not produce substantially different velocity models (not shown). The number of observations and unknown variables for the inversion is shown in Table 5.2. The density of the network and the amount of local events allowed only a 2-D inversion of the data.

Distance between nodes were 25 km at the outside and 20 km in the central part of the model (Figure 5.13). Vertical distances of the nodes are at 5 km until 15 km depth followed by nodes at 22, 30, 40, 50, 60, 150 and 500 km depth. Following EVANS et al. (1994), one additional node is introduced at large distances (>100 km). Figure 5.13 shows the north–south trending model and the spatial difference of the relocation of hypocentres between the minimum 1-D model and the final 2-D inversion. The plotted ray paths show a good coverage in the central part of the model, while the area west of Chiloé Island is traversed mainly by almost parallel rays.

Table 5.2: Number of observations and variables of the inversion

Observations		
P onsets		1628
S onsets		1348
	$\sum$ =	2976

Unknown variables			
focal parameter:	coordinates	$= 3 * 117$	351
	origin times		117
model parameter:	model nodes	$= 15 * 25$	375
		$\sum$ =	843
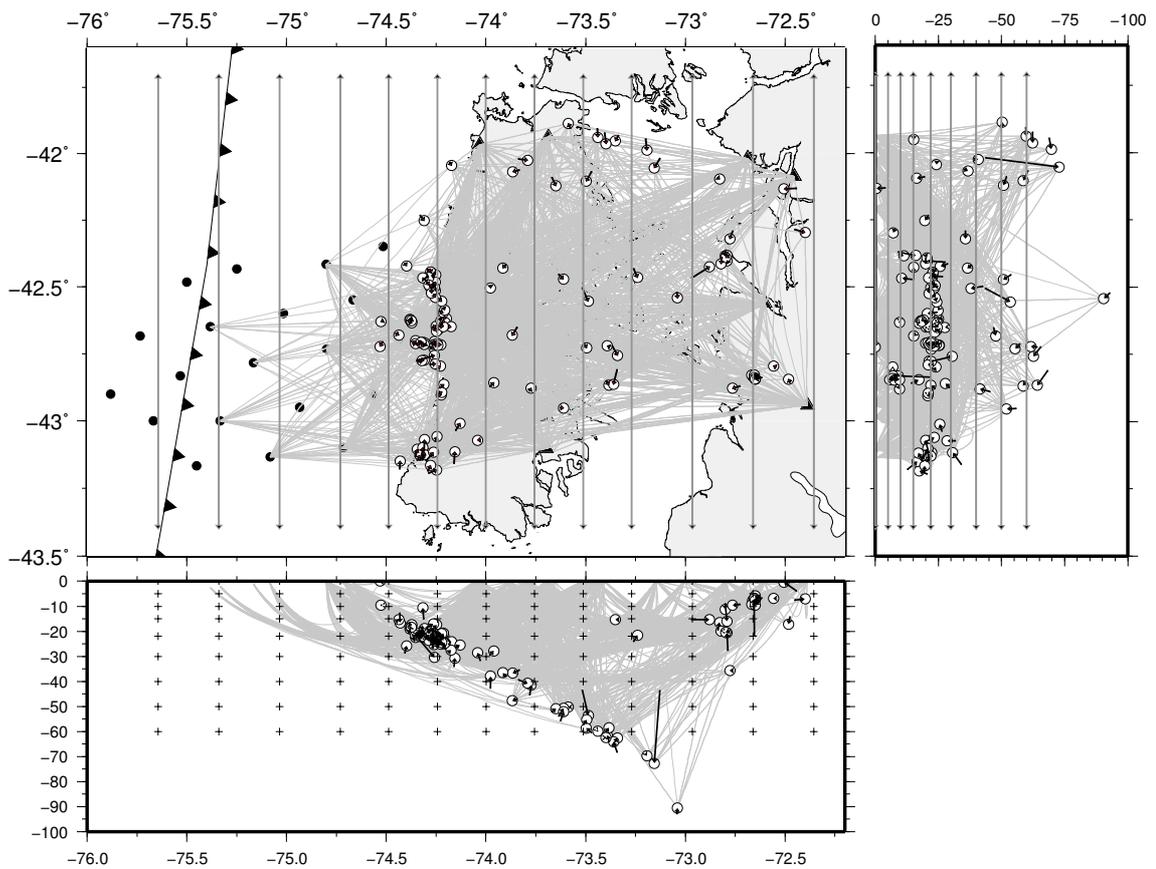
Figure 5.13: Ray paths of 2-D SIMULPS inversion. Final locations are plotted as white circles, the difference to the minimum 1-D model is indicated with arrows. The north-south trending 2-D model geometry is indicated with crosses (lower profile) or with arrows (upper left and right). Landstations and OBS/H are indicated with black triangles and black circles, respectively.
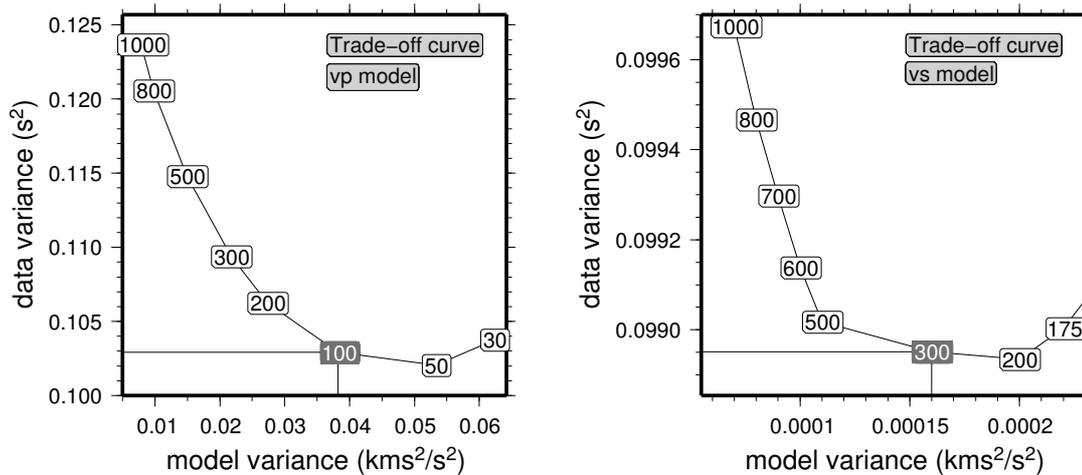
Figure 5.14: Model variance versus data variance plotted for different damping values. The trade-off curves for v_p (left) and v_s (right) models are used to determine the damping values. The resulting damping values are marked with dark background colours (100 for v_p and 300 for v_s). The values are chosen such as to minimize the model variance and data variance at the same time.

The damping value (ϵ^2 in equation 4.7) is a crucial input parameter in the inversion which has to be chosen carefully. Low damping values will lead to high model perturbations, whereas high damping values yield low model perturbations. The damping can be determined by "trade-off" curves between model variance and data variance (EBERHART-PHILLIPS, 1986). This is done by plotting model variance versus data variance of one-step inversions with different damping values for a given model geometry. The trade-off curves for the P and S inversion are shown in Figure 5.14, the resulting damping values are marked with dark colour (100 for v_p and 300 for v_s). The damping is chosen such as to minimize the model variance and data variance at the same time.

Resolution

The spread function of the resolution matrix is a possibility to assess the resolution of the model nodes. The spread function (TOOMEY & FOULGER, 1989, MICHELINI & McEVILLY, 1991) summarizes the information contained in a single averaging vector or row of the full-resolution matrix (HUSEN et al., 2000). For a peaked resolution, i.e. low smearing, the diagonal element is much larger than the off-diagonal elements and the spread is low (HUSEN, 1999). The spread values in Figure 5.15 show low values in the central part of the model.

Synthetic checkerboard tests were carried out to evaluate the resolution of inversion. The procedure includes forward calculation of the travel times for a synthetical velocity model. In a second step the calculated travel times are then disturbed with random noise, the extent of which depended on the pick quality. According to HUSEN et al. (2000) Gaussian
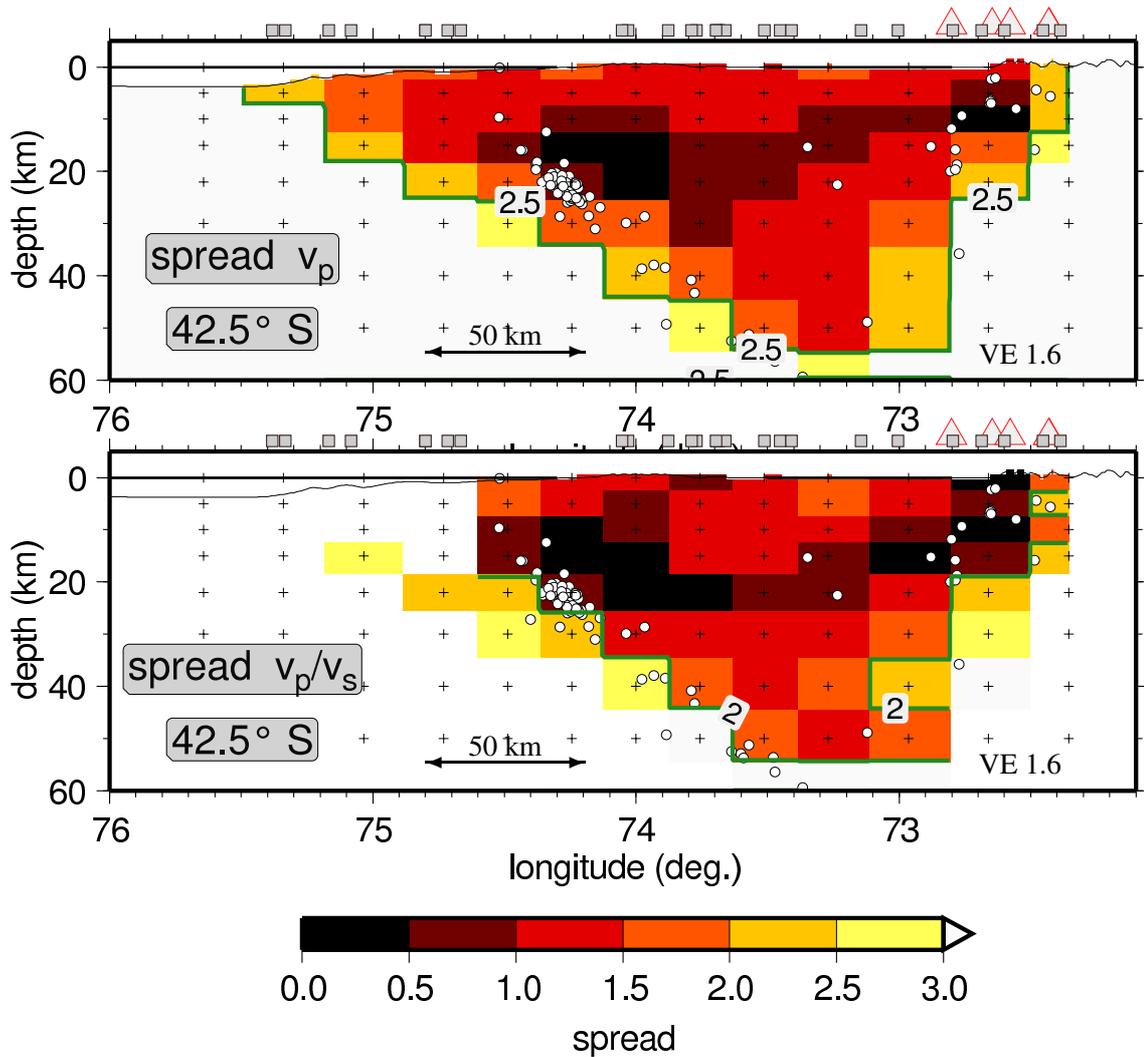
Figure 5.15: Spread values of model resolution matrix for the 2-D v_p (top) and v_p/v_s (bottom) models. The model resolution is high in areas where the spread matrix holds low values. The green contour line encircles regions of good resolution. Stations and active volcanoes are indicated with grey boxes and red triangles, respectively. Model nodes are plotted as crosses.
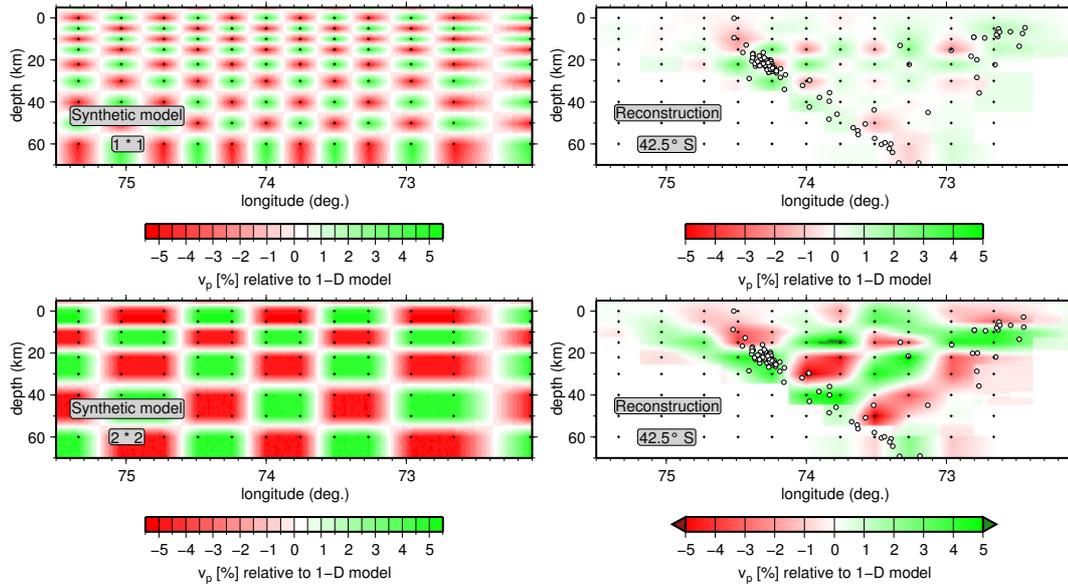
Figure 5.16: Result of checkerboard tests. LEFT: Synthetic P velocity models (upper left: 1×1, down left: 2×2 board). Right: Reconstruction of synthetic P velocity model (upper right: 1×1 ,down right: 2×2 board). The reconstructions are plotted with the resulting hypocentre locations (white circles). See text for more information.

distributed noise was added with a standard deviation ranging from 0.05 s, for highest-quality observations, to 0.2 s, for lowest-quality observations. The noise was added by using the programme `simul_random` (HABERLAND, 1999). Finally, the disturbed travel times are introduced into the inversion. The comparison of the inverted velocity model with the synthetical velocity model helps to assess the resolution of the tomographic inversions. In Figure 5.16 two checkerboard runs are shown in which the minimum 1-D v_p model was regularly perturbed with $\pm 5\%$. Figure 5.16 shows that the perturbations applied to each model node cannot fully be restored in the amplitude, while the checkerboard test with 2×2 model perturbations restored the pattern also in its complete amplitude in the central part of the model. The checkerboard pattern can be reconstructed below Chiloé Island, whereas the areas below the LOFZ, below the continental slope and below the Benioff zone show lower resolutions due to reduced ray coverage.

A threshold for the spread value has been chosen to separate regions with high and low resolution. The choice of the threshold is based on the checkerboard tests, the ray coverage and on the relative size of the spread. The spread contours of the chosen threshold of 2.5 (green lines in Figure 5.15) were superimposed onto the resulting tomographic velocity models.

Results

After 6 iterations the 2-D inversion achieved a 59% reduction of data variance in comparison with the one of the minimum 1-D model.

The v_p model exhibits the main anomalies which are marked in Figure 5.17 in capital letters and described in detail below:

A & B: The two shallow, crustal areas of low velocity (marked as A and B in Figure 5.17) coincide spatially well with the Chiloé basin and the Osorno-Llanquihue basin below the longitudinal valley (GONZÁLEZ, 1990). In-between the two basins, where the paleomagmatic arc is located, the velocity is slightly increased expressed by the shallowing of the v_p 6 km/s contour line.

C: The subducting oceanic lithosphere is imaged with high velocity values, as indicated by the inclined 7.8 km/s contour line.

D: Below Chiloé Island low velocities are found. This anomaly is similar to the tomography study by BOHM (2004) at 38°S where a similar anomaly is observed and is interpreted as a serpentinised mantle wedge (BOHM, 2004).

E & F: Below the longitudinal valley elevated velocities are found, which become visible as a bulge on the 7.8 km/s contour line located at 30 km depth (below E in Figure 5.17). In the direction of the magmatic arc the depth of the 7.8 km/s contourline decreases again to 35 km depth (below F in Figure 5.17). According to the assumption that the 7.8 km/s contour line follows the crustal/mantle boundary, the bulge suggests an indication for a shallow position of the continental mantle of approximately 30 km depth below the eastern side of Chiloé Island and a slightly deeper location of 35 km in the direction of the magmatic arc. Instead of a mantle bulge an alternative model has to be taken into account. The area west of high velocity zone (below D in Figure 5.17) might consist of serpentinised mantle material, which would show lowered P velocities adjacent west of the high v_p values. The model of such a serpentinised mantle wedge below Chiloé Island would equally explain a "bulge" in the v_p contourlines of the velocity model below the longitudinal valley. A sketch of the both models are shown in Figure 5.18.

Due to the lower amount of S onsets and the higher uncertainty of the S picks, the inversion for the v_p/v_s is less stable than the v_p inversion and the resolution of the v_p/v_s model is too low to be conclusive. The shallow areas with increased v_p/v_s ratios (G in
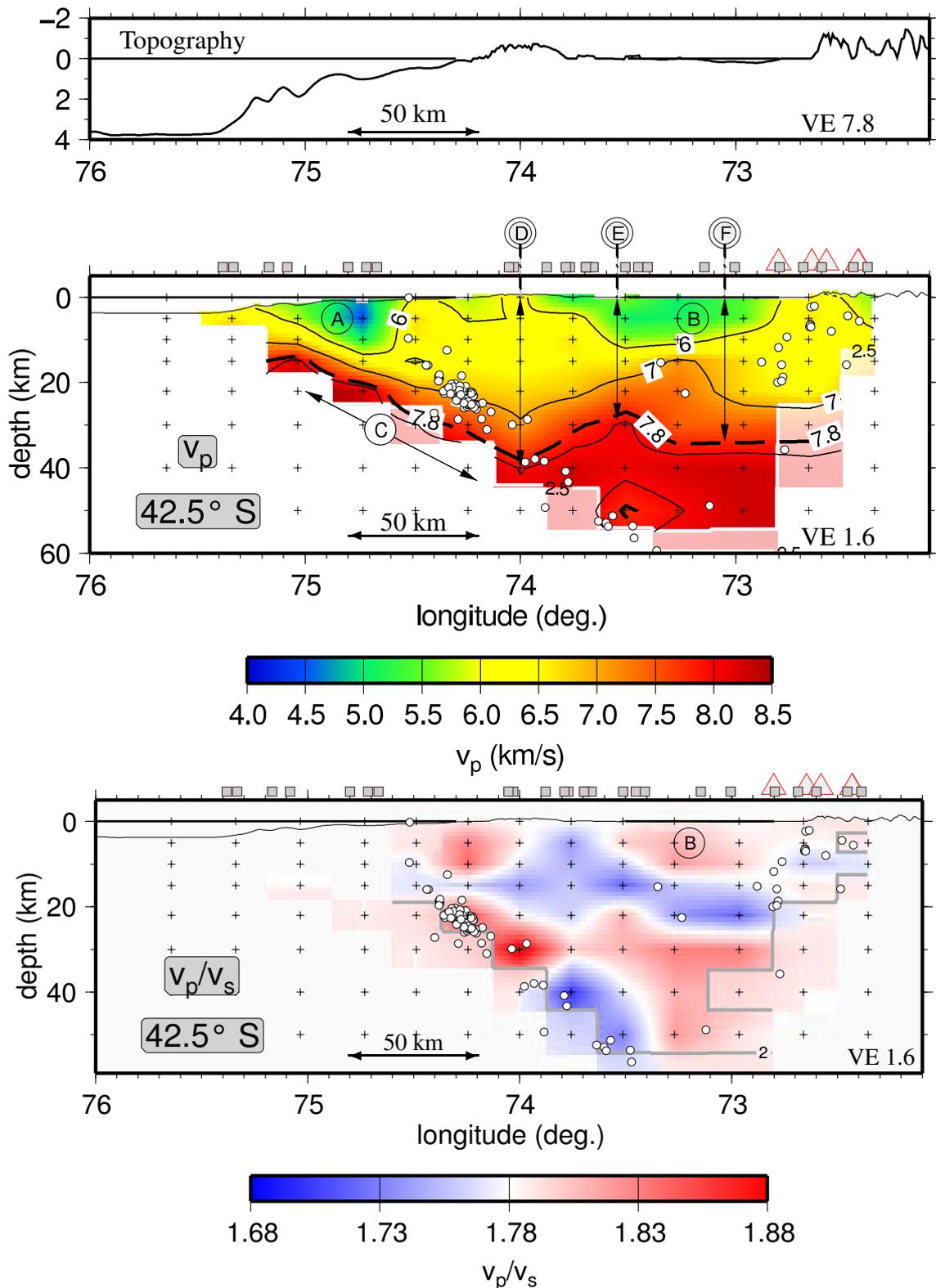
Figure 5.17: Topographic profile (top) and 2-D tomographic velocity models (middle: v_p, bottom: v_p/v_s) along 42.5°. The velocity models are clipped in areas where the resolution of the models is low. White circles represent hypocentres located within the shown 2-D velocity model. The dashed line indicates the v_p 7.8 km/s contour line. Stations and active volcanoes are indicated with grey boxes and red triangles, respectively. Model nodes are plotted as crosses. The white and grey contours enclose regions of good resolution defined by the spread value. Regions of poor resolution are displayed in faded colours.
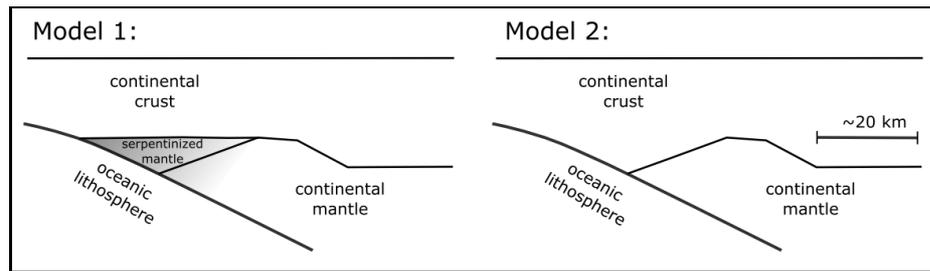
Figure 5.18: Sketch of the two suggested models for the location of the continental mantle. Since a serpentinised mantle has lowered v_p values in comparison to the continental mantle, both models equally explain the "bulge" of the velocity contourlines as observed in Figure 5.17. See text for more information.

Figure 5.17, bottom) coincide spatially with the sedimentary basins. Hydration of the subducted oceanic plate should result in elevated v_p/v_s ratios and lowered v_p values (CARLSON & MILLER, 2003). Since the seismicity cluster below the coast of Chiloé Island between 15 and 36 km depth (marked H in Figure 5.17, bottom) is situated in an area with v_p/v_s ratios of up to 1.88 and v_p velocities of 7 km/s one might speculate that the oceanic crust is hydrated.

A similar area of increased v_p values is described for southern Chile at $38°$ by BOHM (2004), but mantle velocities there are reached at greater depths of 55 km below the magmatic arc and ~ 45 km depth below the longitudinal valley. The finding of an area with increased v_p values at $42.5°$S (by this study) and at $38°$S by BOHM (2004) indicates that the mantle bulge is a regional feature with a continuous lateral extension of more than 450 km along the southern Chilean subduction zone. Recent tomographic studies made on the basis of data from the northern TIPTEQ array (HABERLAND, in prep.) again show this high velocity zone below the longitudinal valley at $\sim 38°$S (Figure 5.19). Uncertainties are too large to be conclusive, but it can be speculated that the shallower course of the 7.8 km/s contour line at $42°$S indicates a shallower position of the mantle with higher latitudes.
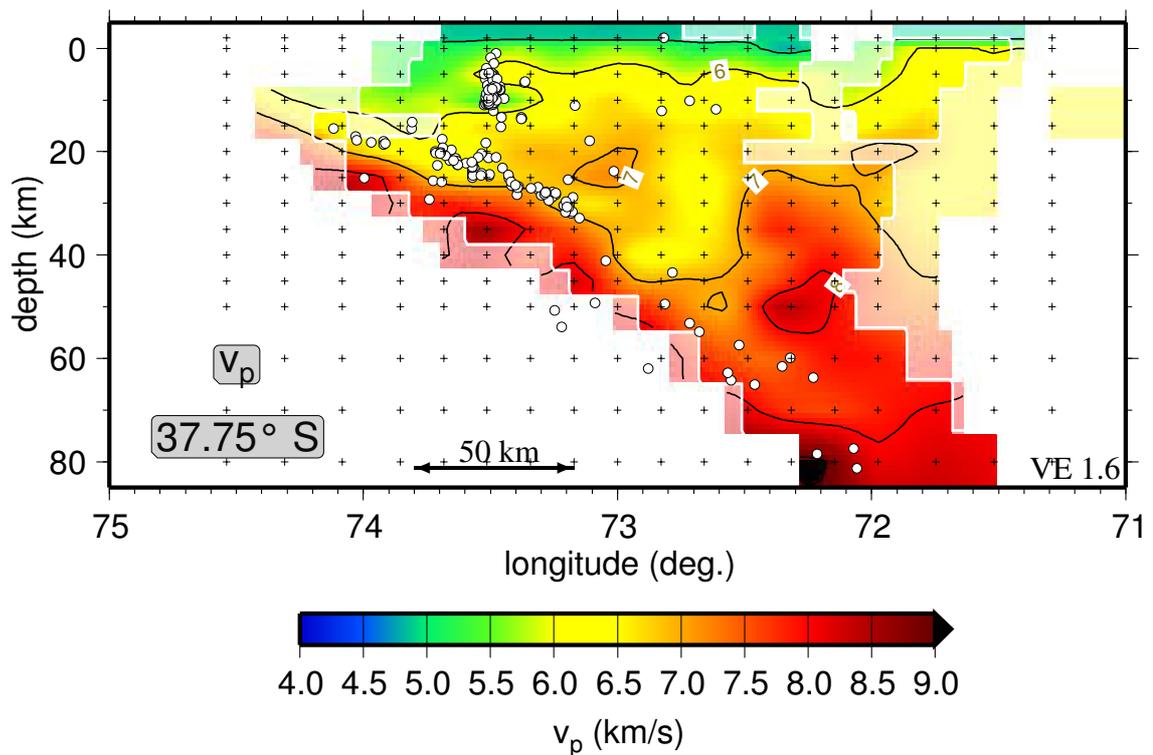
Figure 5.19: West-east section through 3-D v_p model at 37.75°S (HABERLAND, in prep.). The velocity model reveals, alike our study area, a high velocity feature below the longitudinal valley. The Figure is plotted with the same scale and colourscale as Figure 5.17.

Chapter 6

State of Stress

6.1   Focal Mechanisms and Seismicity Along the LOFZ

Moment tensor inversion (MTI, Section 4.2.2) for the strongest events along the LOFZ was applied. The inversion solution in this study is given in terms of five independent components of the moment tensor, thus forcing the isotropic component to be zero. This constraint is reasonable for tectonic earthquakes, but not for volcanic events. Different factors indicate a tectonic origin of the observed seismicity. Events below the Corcovado and Chaitén volcanoes exhibit P and S onsets typical for tectonic events. Furthermore, no volcanic signals such as tremors were observed like further north at Villarrica volcano (ORTIZ et al., 2003, TÁRRAGA et al., 2006). MTI solutions for the whole moment tensor (six components) do not show elevated isotropic moment tensor components, but indicate predominantly double-couple mechanisms. Shear wave splitting as indication of seismic anisotropy was not observed for the dataset. At least six vertical components of P-waves and one transversal component of the S-phase from selected key stations were used for each inversion. In order to avoid near field effects, observations of hypocentral distances which were smaller than 2 wavelengths ($\sim$9 km) were ignored. Since calibration of the ocean bottom seismometers was not available, only land stations were used for the MTI. For all given pairs of stations and hypocentres, full waveform Green functions were calculated (e. g. MÜLLER, 1985, CESCA et al., 2006) using the 1-D minimum velocity model (see Section 5.1). CESCA et al. (2006) showed that the azimuthal coverage of the epicentre has a minor impact on the results of the inversion when using an amplitude spectra tensor inversion; the error resulting therefrom can be compared with the one introduced by wrong velocity models or wrong source time functions. In order to check the stability of the final moment tensors, inversions with different frequency ranges, taper lengths and taper types were calculated. The frequency range was restricted to values between 0.5 and 4.5 Hz (Table 6.1). Furthermore, different source constants (depths/duration) and subsets of stations for the inversion were used, in order to check the appropriate setting of these parameters. The alignment of the synthetic and observed seismograms was checked in the

Table 6.1: Summary of moment tensor solutions for shallow continental events along the LOFZ.

Nr.	Date/Time	Lat/Lon	Depth from location routine [km]	Strike/Dip Rake	DC(%)	Misfit	M0 (dyn*cm)	M_w	f(Hz)	Wave-forms used	Epicentral distance to next stations [km]
1	2005-08-18 18:33 52.4	42.0048°S 72.4387°W	6.86	210/45 -151	88	0.30	7.8E+20	3.2	1.1–4.5	10	6.1/20.5/63.3
2	2005-08-18 21:26 36.5	41.9968°S 72.4393°W	7.43	109/64 -23	83	0.31	5.4E+21	3.76	0.8–4.0	8	10.0/20.6/64.2
3	2005-08-18 21:28 20.3	42.0033°S 72.4515°W	5.90	198/66 169	68	0.29	8.7E+20	3.23	1.0–4.5	8	9.2/19.5/63.3
4	2005-08-22 21:29 05.5	42.0058°S 72.4705°W	6.07	223/22 -120	84	0.19	5.4E+20	3.09	1.0–4.0	10	9.0/17.9/62.7
5	2005-08-23 01:15 21.5	42.0024°S 72.4645°W	6.11	281/66 -4	62	0.22	1.5E+21	3.39	1.1–4.5	8	9.3/18.4/63.2
6	2005-01-18 21:22 29.1	42.3806°S 72.8002°W	10.13	144/45 0	78	0.36	2.13E+20	2.82	1.1–4.5	13	26.0/29.2/41.3
7	2004-1210 17:03 44.9	42.8437°S 72.6369°W	8.43	231/59 -162	70	0.28	2.7E+21	3.56	0.5–4.0	9	13.1/23.0/31.4
8	2005-05-19 11:44 42.5	42.8001°S 72.5458°W	6.92	319/84 2	62	0.27	3.3E+20	2.95	1.1–4.5	8	20.3/21.3/26.8
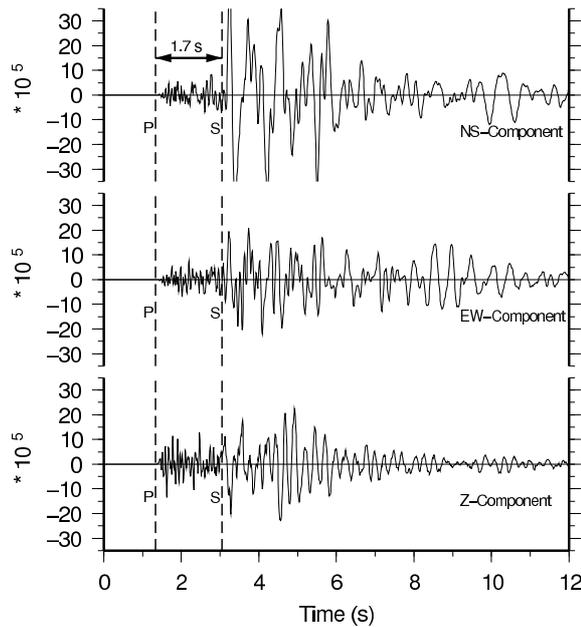
Figure 6.1: Example of typical wave forms of closest station S15 and for onsets arriving from the nearby Hornopirén cluster. The onset of the event from 18.08.2005, 21:26 is shown. P minus S time is 1.7 s indicating a short distance to the hypocentre. Modified after LANGE et al. (2008).

time and frequency domain. Some of the events (in particular in the northern part of the study area, see discussion below) exhibit poor azimuthal coverage. However, small P minus S onset times (<1.7 s) at closely located stations clearly indicate that the hypocentres are located in the upper crust very close to the next station (Figure 6.1). Accordingly, the accurate depths and locations of the events yield a high stability of the MTI. Calculations of Green functions for varying source depths and the inversion for the moment tensors for two representative events with M_w 2.0 and 3.2 are shown in Figure 6.2. The centroid depths calculated by the MTI (using the depth with minimal residual) are compatible with the hypocentre depths from the arrival times and differ by less than 1.5 km for all inverted events. Small variations of the depths ($\pm$1.5 km) result in only minor variations for strike, dip and rake ($\pm$6°). The moment tensor was decomposed into a major double-couple and a compensated vector dipole (CLVD) (JOST & HERRMANN, 1989). Synthetic and observed seismograms of amplitude spectra and displacements are shown in Figure 6.3 for the M_w 3.2 event on August 18, 2005 (Event 2 in Table 6.1).

Crustal seismicity in the forearc is clearly separated from the Wadati-Benioff seismicity (Figure 5.9). During the 11-month measurement period 75 events with shallow depths (<25 km) occurred within the continental crust. These events are located in clusters along the LOFZ and can be spatially related to the LOFZ and volcanoes.
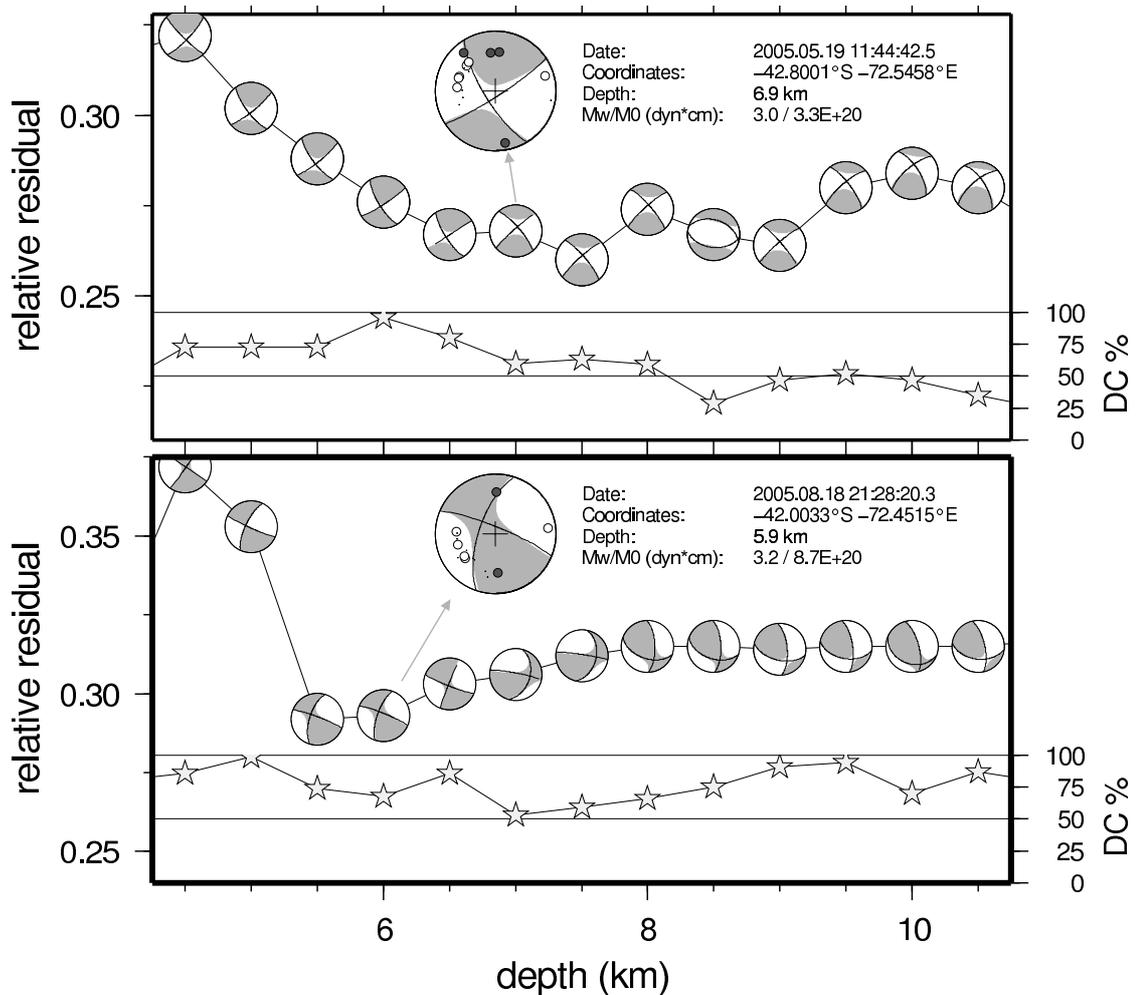
Figure 6.2: Summary of the inversion for two representative events. Inverted fault plane solutions and double-couple moment-tensor components plotted versus varying depths. The final solution (the solution with the depth from the inversion routine) for the two events is plotted with high-quality first-motion polarities and marked with an arrow. Double-couple components are plotted as stars. Modified after LANGE et al. (2008).
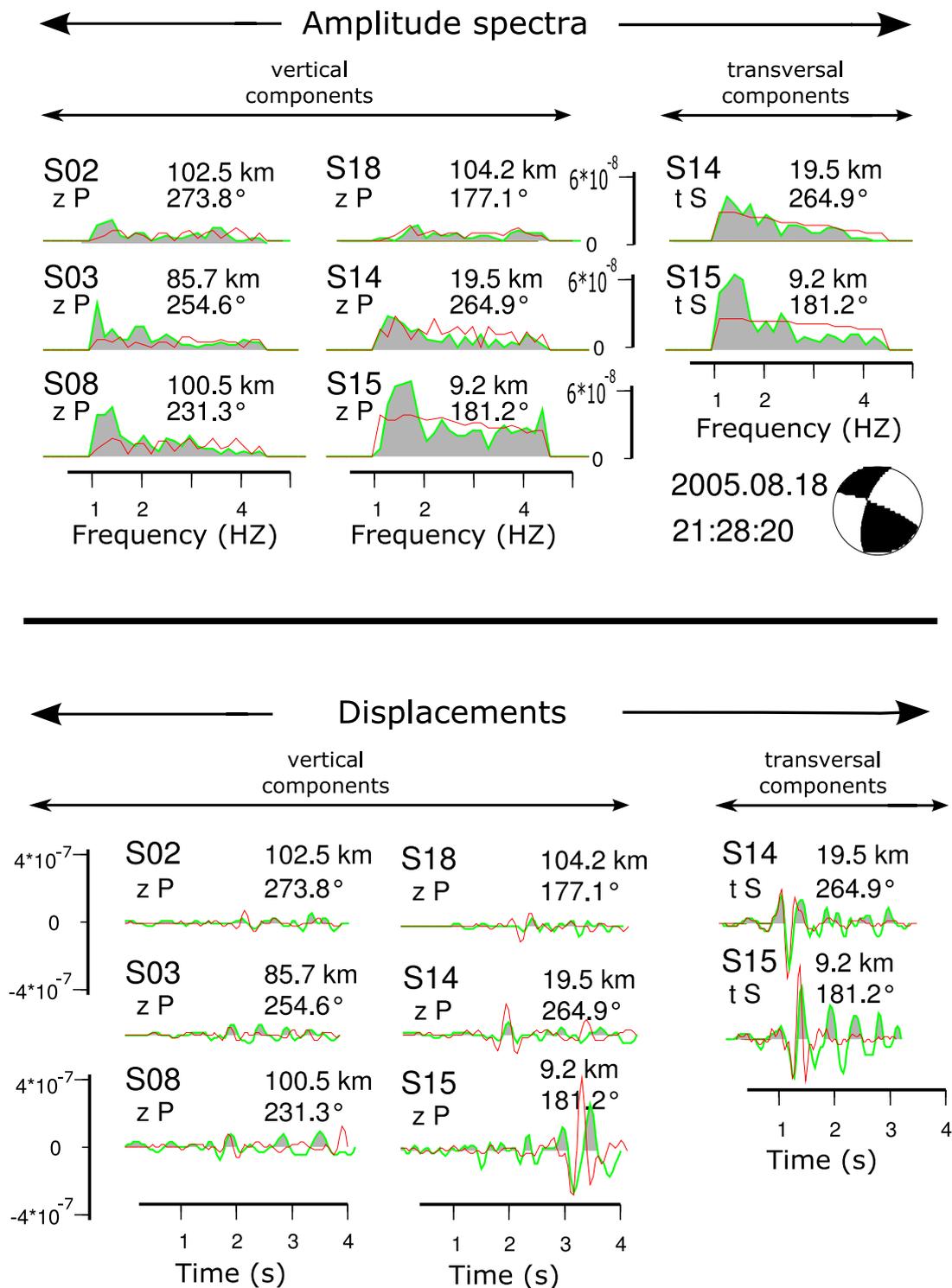
Figure 6.3: Comparison between synthetic (lines) and observed (grey areas) amplitude spectra (top) and displacements (bottom) for vertical components (P phase, zP) and transversal components (S phase, tS). The event (M_w 3.2) occurred on August 18, 2005. The components are annotated with station name, distance and backazimuth. Modified after LANGE et al. (2008).

In the following the different seismicity clusters (from north to south) are described in detail using the numbers provided in Figure 6.4:

A.) 10 km south of the town of Hornopirén (42°S) seismic activity of up to a magnitude of 3.8 M_w occurred in a region within the LOFZ (Figure 6.5). The main events, which were felt by the inhabitants of Hornopirén, occurred on August 18, 2005, at 21:26 and 21:28 UTC (M_w 3.8 and 3.2) followed by events on 22.08.2005, 21:29 and 23.08.2005, 01:15 with M_w of 3.1 and 3.4, respectively. In total, 32 aftershocks were detected from this cluster, 19 events of which reveal more than 8 P and 4 S readings. The events are located at shallow depths of between 5 and 8 km (Figure 6.5). The distances from these events to the nearest stations were 10, 20 and 60 km, respectively. Most of the fault plane solutions (Events 1–5 in Table 6.1) exhibit similar strike-slip mechanisms. The possible fault planes on which the movement occurred are trending $\sim 10°$ or $\sim 100°$. The observed events reside on the eastern branch of NNE-SSW trending faults bounding a pull-apart basin (DEWEY & LAMB, 1992). Taking into account the NS trending geometry of the LOFZ ($\sim 10°$N) and the NS trending schistosity ($\sim 19°$N) (CEMBRANO et al., 2000), north-south directed strike-slip movement is most likely to result in a dextral strike-slip fault plane which is inline with the regional geological observations. The smallest magnitude event (M_w=3.1) is the only event which does not reveal a strike-slip mechanism. This event indicates extension which possibly took place on the eastern side of the pull-apart basin. The moment tensors from the strike-slip events are compatible with the stress field derived from mylonitic faults (long-term signal) by CEMBRANO et al. (2000) which exhibit continuously SW-NE oriented largest compressional stress (σ_1=244°,13°) since 1.6 Ma (LAVENU & CEMBRANO, 1999), indicating a stable tectonic regime along the fault zone at this latitude. The deepest event with a depth of 7.6 km within the LOFZ near Hornopirén (Figure 6.5) gives the minimal depth extent of the LOFZ of 8 km for this latitude. The location of the cluster directly below the surface trace of the LOFZ described by CEMBRANO et al. (2000) in Figure 6.5 indicates a relatively steep inclination of the fault system. This cluster of seismic activity is a clear evidence for activity inside of the LOFZ. Further activity along the LOFZ is indicated by individual events located in direct vicinity of the LOFZ more to the south (Figure 6.4).

B.) Along the southwestern coast of Hueqi peninsula five events occurred. In 1906, the Hueqi volcano in the centre of the island erupted explosively (CASERTANO, 1963). The fault plane solution for the strongest event in this cluster (M_w=2.8) shows a strike-slip mechanism. It is likely that this cluster is related to a $\sim 135°(\pm 15°)$ trending fault which forms the coast line and continues to the S into the valley SE of station S16 (see Figure 6.6).
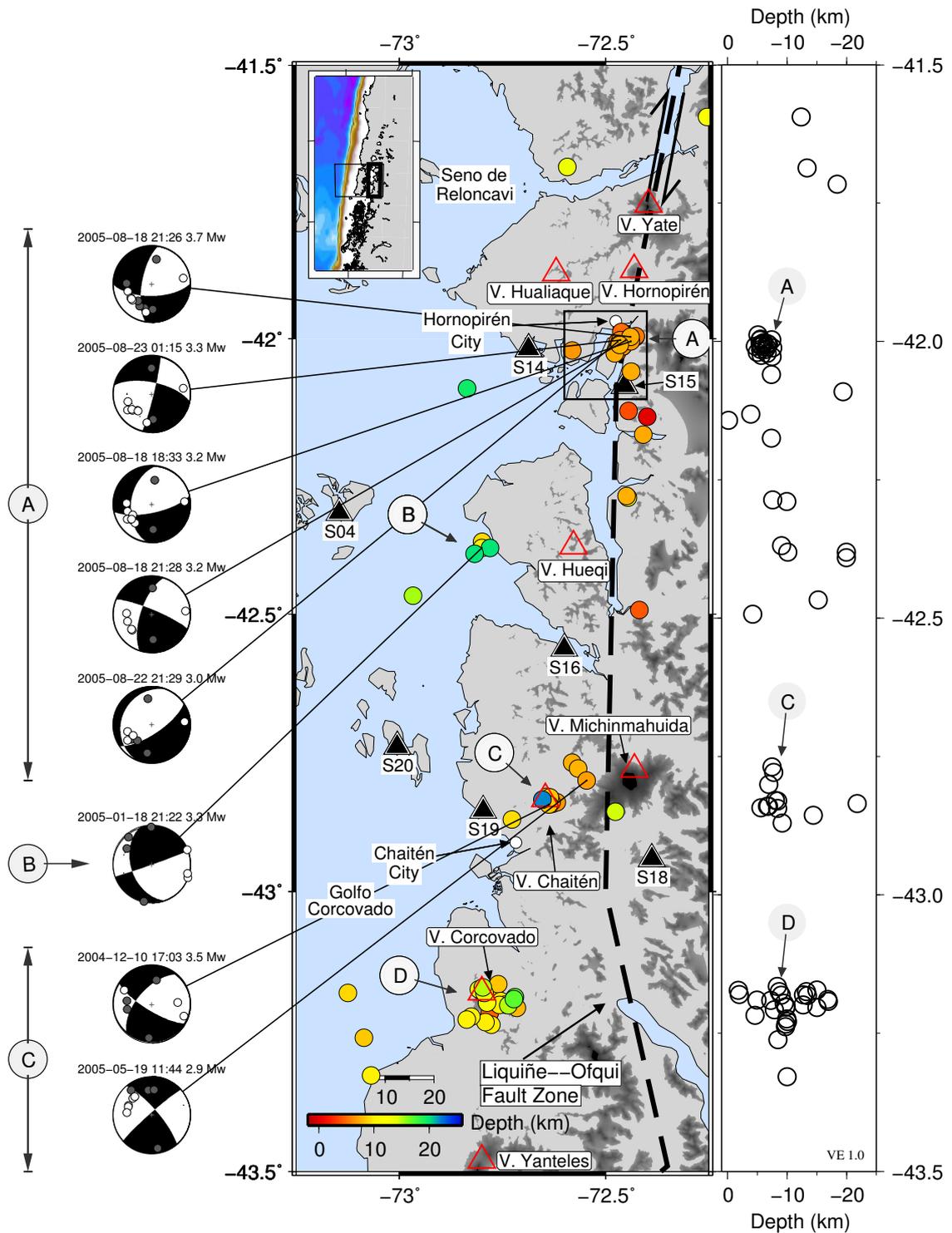
Figure 6.4: Crustal seismicity with solution from MTI (double couple component lower hemisphere plot with first-motion polarities) along the LOFZ (41.5°S–43.5°S) is located mainly in four spatial clusters (A–D). Seismic stations are indicated by inverted triangles. Volcanoes are indicated with upright red triangles (SIEBERT & SIMKIN, 2002). Box indicates the location of the close-up view shown in Figure 6.5. Modified after LANGE et al. (2008).
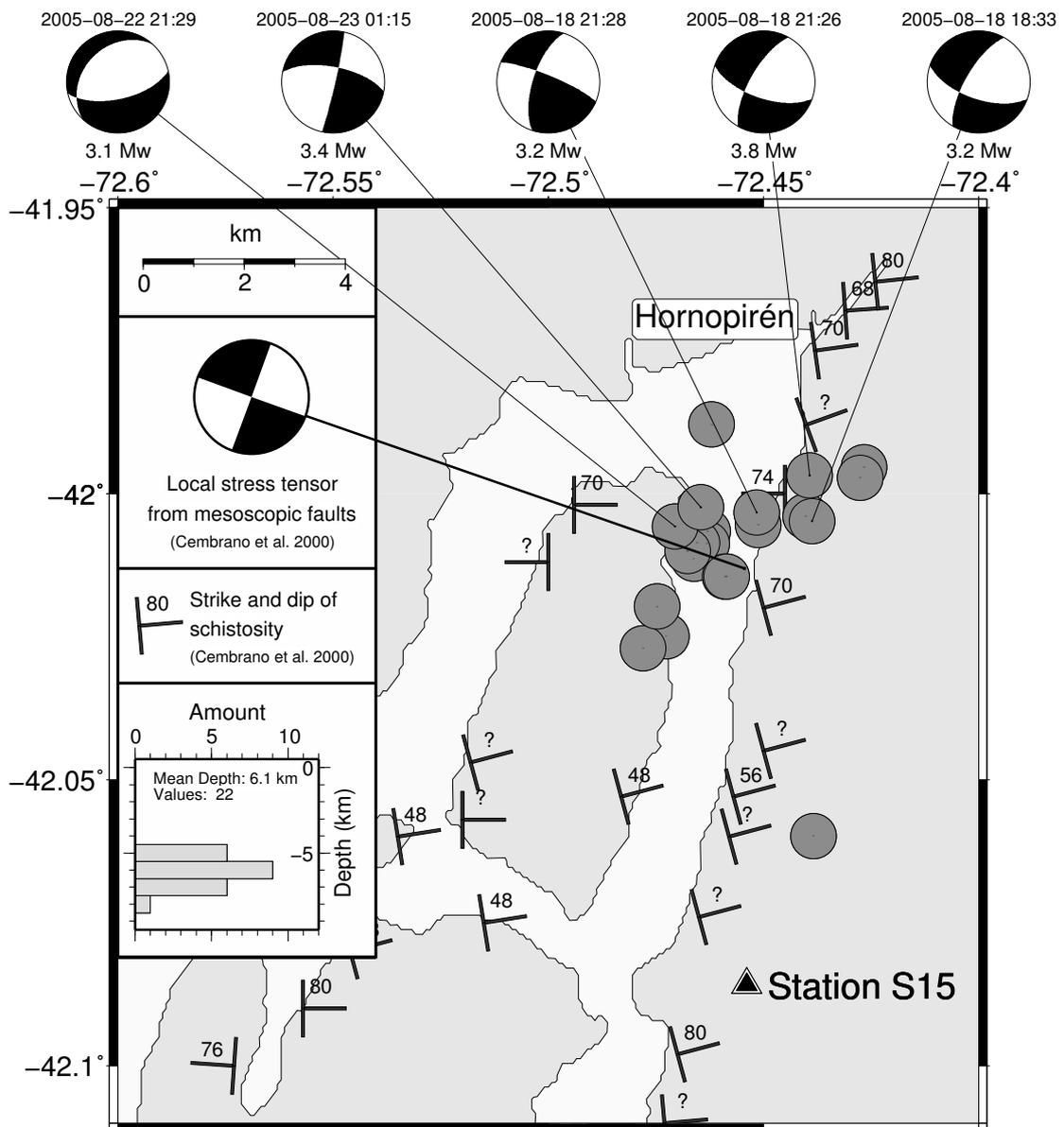
Figure 6.5: Blow-up view (16×16 km) of the events near Hornopirén (cluster A in Figure 6.4) with focal mechanisms (double-couple components) from moment tensor inversion (modified after LANGE et al. (2008)). Inclination of mylonitic surface outcrops of the LOFZ after CEMBRANO et al. (2000). The LOFZ is an approximately 8 km wide N-S trending feature at this latitude. Local stress tensor of CEM-BRANO et al. (2000) derived from mesoscopic faults plotted in the inlay and showing a strike-slip mechanism. All of the hypocentres reside at depths of less than 10 km (see histogram) below surface outcrops of the LOFZ indicating a steep inclination of the fault zone. The closest seismic station (S15) is indicated by a black triangle. Location of close-up view is indicated in Figure 6.4.
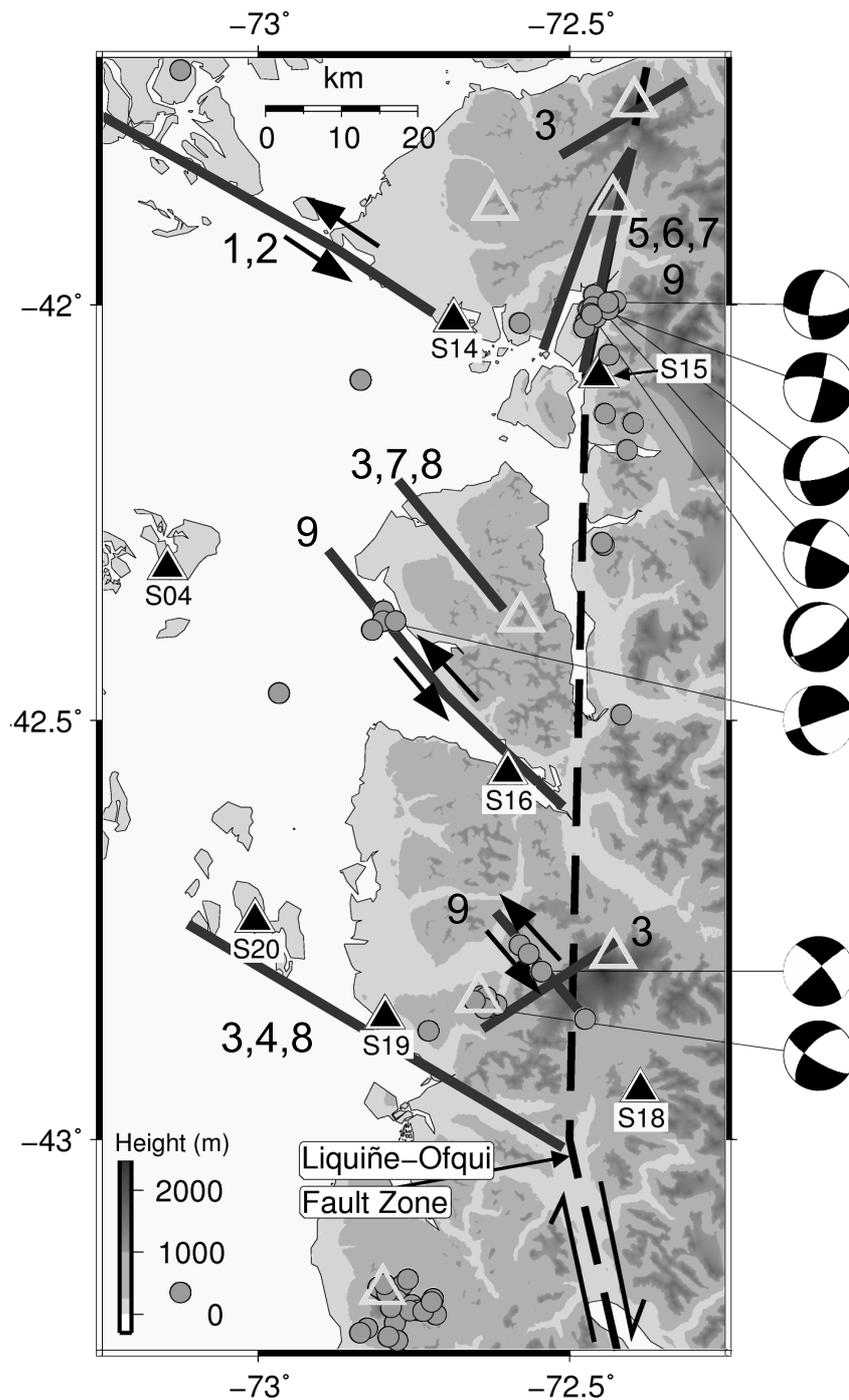
Figure 6.6: Compilation of major faults and alignments along the LOFZ (between 41.5° and 43.5°S) and crustal seismicity with fault plane solutions of this study. Seismic stations are shown as black triangles, volcanoes are indicated with grey triangles. Modified after LANGE et al. (2008). Numbers indicate references to faults and alignments: 1: MELNICK & ECHTLER (2006), 2: HACKNEY et al. (2006), 3: LÓPEZ-ESCOBAR et al. (1995), 4: LAVENU & CEMBRANO (1999), 5: CEMBRANO et al. (2000), 6: DEWEY & LAMB (1992), 7: SERNAGEOMIN (2003), 8: CEMBRANO et al. (1996) 9: this study

C.) Below Chaitén volcano, a post-glacial caldera or explosion crater, 3 km in diameter (LÓPEZ-ESCOBAR et al., 1993), seismicity of up to magnitude M_w 3.6 was observed. Chaitén caldera has developed along a 14 km SW-NE oriented fissure, the last eruption was dated to 9370 BP (NARANJO & STERN, 2004). Main seismicity in this area is spatially related to the Chaitén caldera located on the western flank of Michinmahuida, a strato-volcano with a permanent ice cap. The two focal mechanisms for this cluster show again strike-slip mechanisms with 40° or 130° strike directions of the possible fault planes. The event from May 19, 2005 is the southwestern-most event of NW-SE aligned hypocentres. Accordingly, this event can be related to a NW-SE trending fault plane.

D.) The southernmost cluster of seismicity is spatially related to the Corcovado volcano. Compared to the other clusters, the hypocentral resolution is much lower because the events are all outside the network. Nevertheless, this cluster has strong activity in terms of event number, but the magnitude of the events does not exceed the magnitude M_w 2.6. Because of the poor azimuthal coverage, a reliable moment tensor solution for events in this cluster could not be obtained.

The focal mechanism dataset along the LOFZ consists of eight shallow events with depths less than 11 km (Table 6.1) which are mainly strike-slip events (Figure 6.4). The inverted stress field (MICHAEL, 1987) of the events show varying solutions for σ_2 and σ_3, while the direction of σ_1 is comparably stable with an almost horizontal (8°) and 76° trending direction. The inferred stress field shows a strike-slip regime (Figure 6.7). Since the input dataset is governed by strike-slip events, this is the expected stress regime. The comparison of the stress field with mesoscopic fault data (CEMBRANO et al., 2000) from Hornopirén with similar values (σ_1=244°, 13°; σ_2=57°, 77°; σ_3=154°, 02°) indicates that the actual deformation is similar to the long-term deformation stress field suggesting a stable stress regime since the Pliocene (CEMBRANO et al., 2000). Furthermore, the 60° striking elongation of the volcanoes (ROSENAU et al., 2006) is close to the trending of σ_1 from actual seismicity and the mylonitic faults. Since a direction of 55° of σ_1 for a 10°E trending strike-slip deformation zone is the expected shortening axis (LÓPEZ-ESCOBAR et al., 1995), the trending of 76° of σ_1 derived from the stress field inversion is inline with the structurgeological model of stress partitioning within the forearc (FITCH, 1972). Figure 6.8 shows the orientations of the principal geological features.

Strike slip faults occur in about 50% of modern subduction zones (JARRARD, 1986b). The model of slip partitioning due to oblique subduction is applied to many of them, e. g. the Great Sumatra fault (BECK JR., 1983, BAROUX et al., 1998, MCCAFFREY et al., 2000) and others (JARRARD, 1986b, KIMURA, 1986). Like the LOFZ many of these fault zones are accompanied by volcanic arcs (e. g. MCCAFFREY et al., 2000). A discussion about
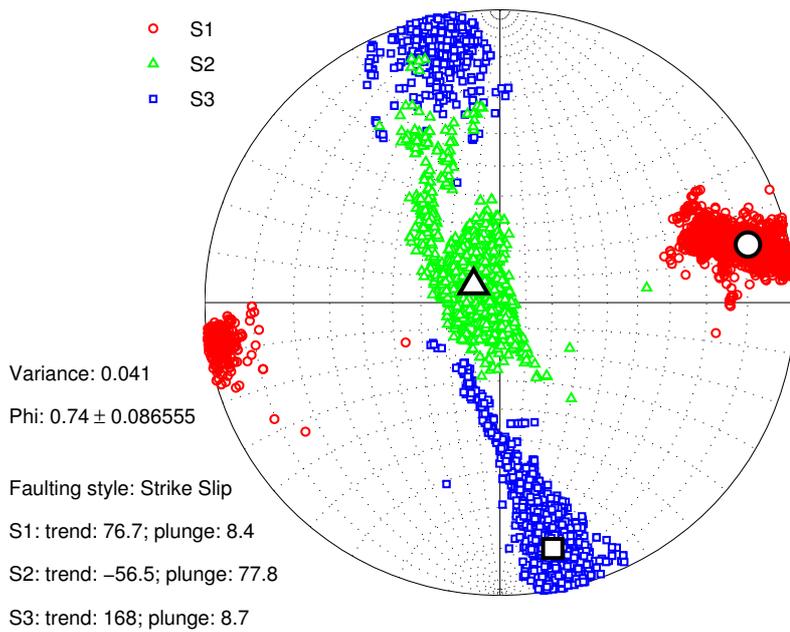
Figure 6.7: Stress inversion of the continental events along the LOFZ (Figure 6.4) exhibit a strike-slip regime with 76° trending of σ_1. The small symbols indicate the results of the bootstrap calculations. Modified after LANGE et al. (2008).
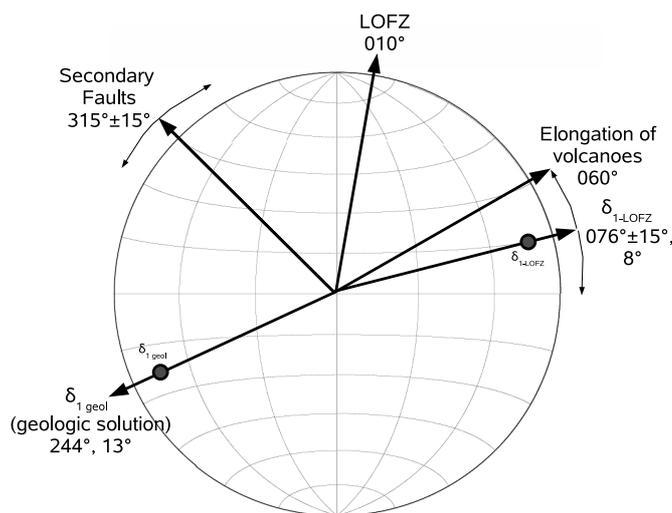
Figure 6.8: Lower hemisphere equal area projection showing the orientation of compressional stress from geological faults ($\sigma_{1\,geol}$, CEMBRANO et al. (2000)) and from stress tensors inversion ($\sigma_{1\,LOFZ}$, Figure 6.7), together with the orientation of faults and elongated volcanoes. Modified after LANGE et al. (2008).

the genetic relation between the location of the volcanoes and the LOFZ was carried out by LÓPEZ-ESCOBAR et al. (1995). MCCAFFREY et al. (2000) observed for the Sumatra fault that two thirds of the margin-parallel component of relative plate motion occurs on the Sumatran strike-slip fault; the rest occurred near the trench. It has been proposed that for the southern Chilean margin the actual obliquity is too small to account by itself for strike-slip tectonics (CEMBRANO et al., 2000). For the southern Chilean Andes it is suggested that a thermally weak continental crust and strong intra-plate coupling are the key factors for intra-arc faulting (CEMBRANO et al., 2000).

6.2 Focal Mechanism of the Benioff Zone Events

Only events with at least 10 unambiguous polarities were considered for the calculation of focal mechanisms in which first-motion polarities were employed (REASENBERG & OP-PENHEIMER, 1985). The method (Section 4.2.3) is applied to events within the network (GAP≤180°). Furthermore, events which did not produce unique solutions were rejected. A subset of 26 events passed the polarity quality test and produced stable solutions. The focal mechanism with the corresponding first-motion polarities are plotted in Figure 6.9.

As shown in Figure 6.10, the depth range of the focal mechanism is between 16 and 64 km, and all events are located east of 74.5° longitude. The smallest magnitude for which a focal mechanism could be calculated was 1.9 M_l. Because of insufficient coverage of the focal plane (and therefore no unique fault plane solution) for the shallow continental events, and for the events near the trench, no fault plane solution for these areas could be calculated. Therefore, all fault plane solutions (based on first-motion polarities) are exclusively associated to the Benioff zone. From 26 solutions the majority of 19 events exhibit thrust type character, followed by 6 strike-slip mechanisms and one normal fault solution. From the 11 events with magnitudes $M_l \geq 3$ (red solutions in Figure 6.10) all but one show thrust type characteristics suggesting that they occur near or at the plate interface. This result suggests a strongly compressional stress/strain regime from 16 km down to a depth of 64 km. The stronger diversity of the mechanism for smaller events may reflect their occurrence on secondary faults.

The dataset used in the stress inversion (MICHAEL, 1987) consists of the 26 events from first-motion polarities (Figure 6.9 and 6.10) with magnitudes of 1.9 and 5.1 M_l. The hypocentres are located in a depth range between 15 and 64 km. The inverted stress field in Figure 6.11 reveals stable directions for σ_3 with varying directions for σ_1 and σ_2 reflecting the different directions of the thrust events (73% of the events are thrust-type events) of the focal mechanism dataset (Figure 6.9). The dip inclination of σ_1 is almost horizontal (3°), and the dip of σ_2 is inclined by 18°. When using the classification of GUIRAUD et al. (1989), these directions, together with the steep inclination of 71°of σ_3, indicate a compressive stress regime. The algorithm does not weight the events with magnitudes. In terms of energy release, the dataset is determined by the 5.1 M_l event from August 23, 2005 with SE-NW trending σ_1.

The shallow compressional regime found here is in agreement with other studies of subduction zones (e. g. DELOUIS et al., 1996, CHRISTOVA, 2004) and is interpreted as result of "seismic coupling" (KANAMORI, 1971) between the oceanic plate and the overriding continental plate. For the deeper part of the Wadati-Benioff zones down-dip extension has been reported regularly, starting typically at depths higher than 50 km. This commonly reported stress pattern for intermediate-focus earthquakes is down-dip tension, and its
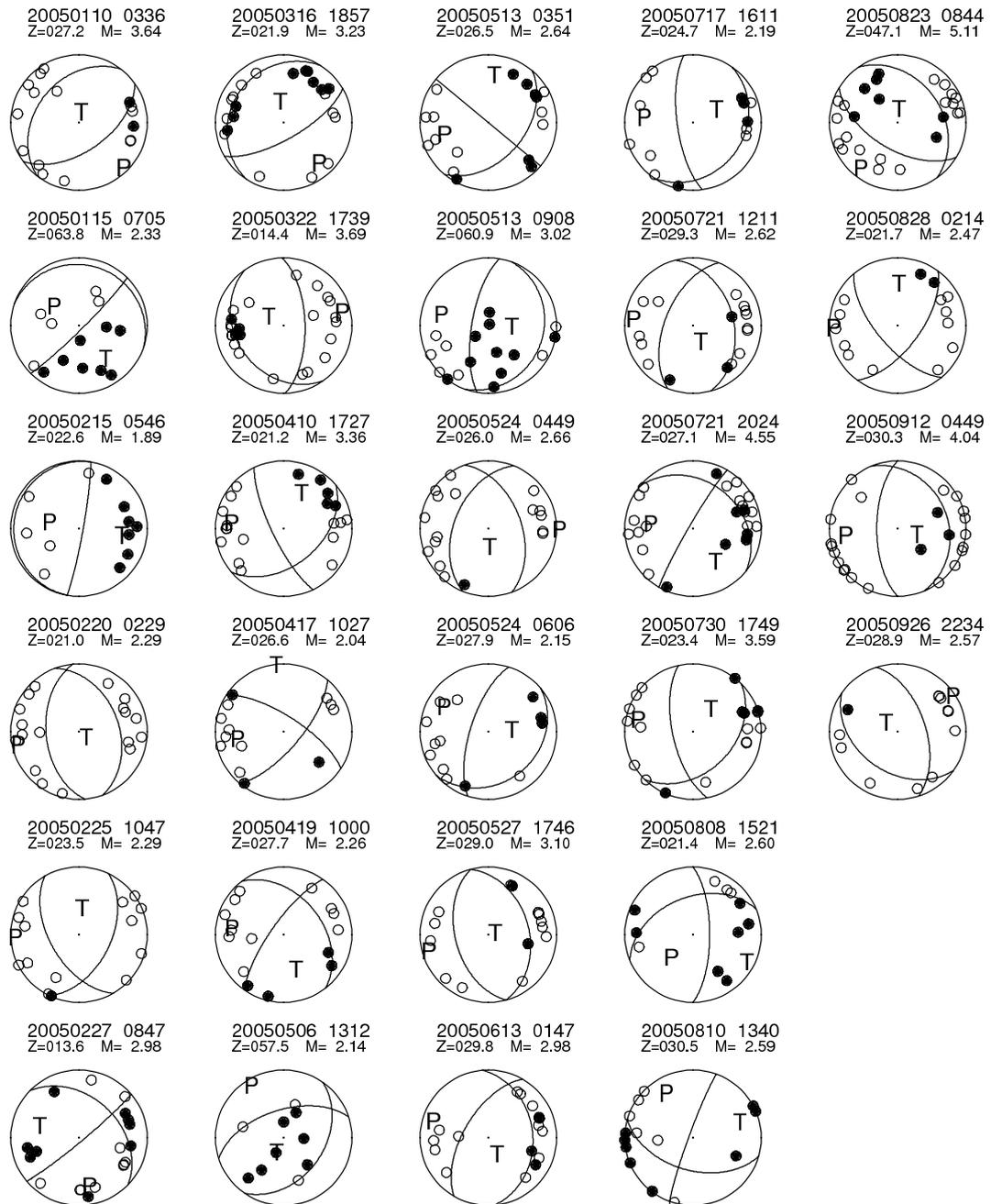
Figure 6.9: Fault plane solutions of the Benioff-Zone (lower hemisphere plot) based on first-motion polarities labeled with date, time, depth (km) and magnitude (M_l). Each solution holds at least 10 high-quality onsets and leads to an unique fault plane solutions using FPFIT.
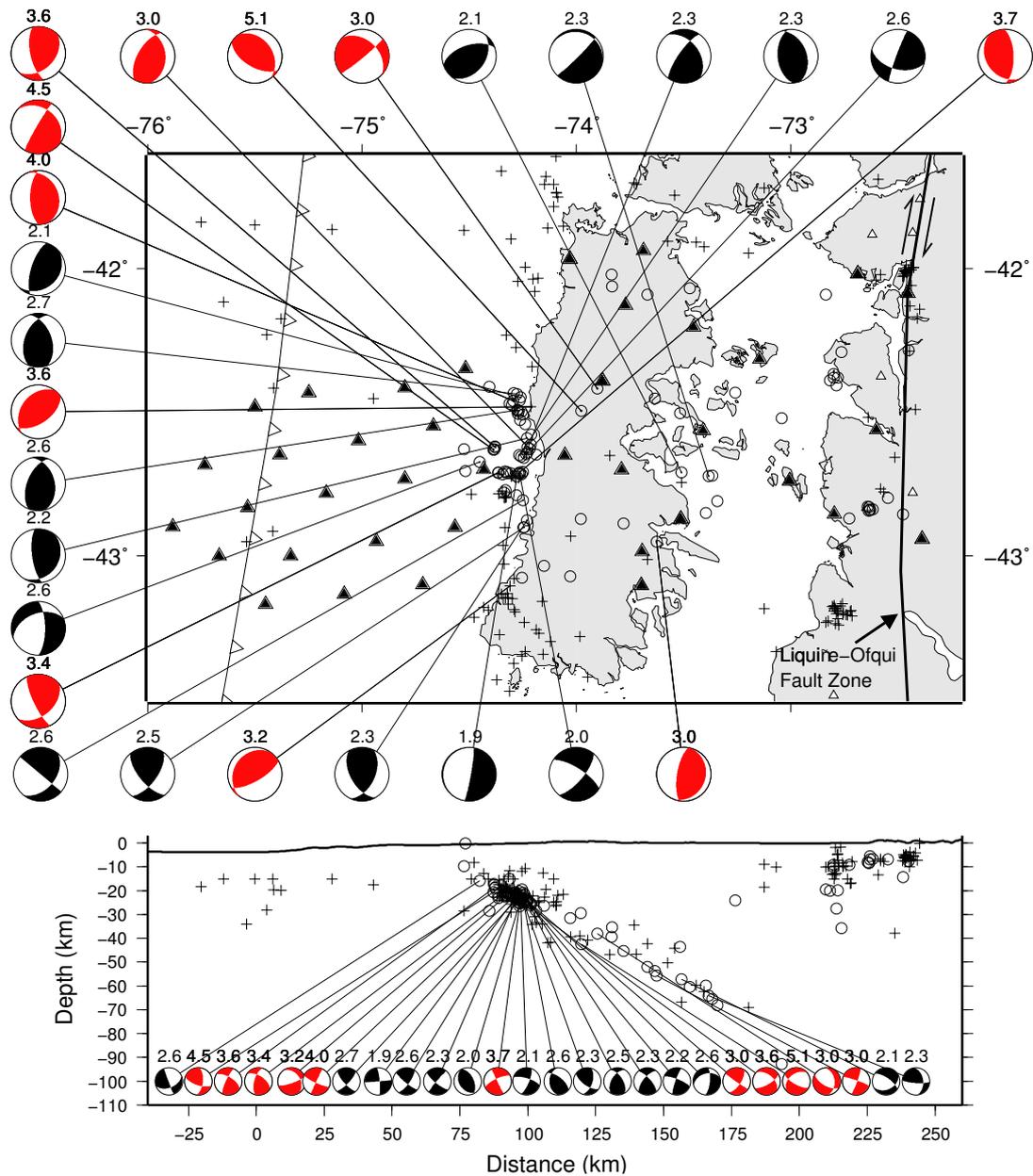
Figure 6.10: Location of fault plane solutions of events attributed to the Benioff-Zone (lower hemisphere plot, labeled with M_l) based on first-motion polarities. Stronger events ($M_l \geq 3$, shown in red) all but one show thrust characteristics. The majority of the weaker events likewise show thrust mechanisms suggesting a strongly compressional regime to depths of 65 km. In the vertical west-east cross-section (downside) the focal spheres are projected as seen from the south.
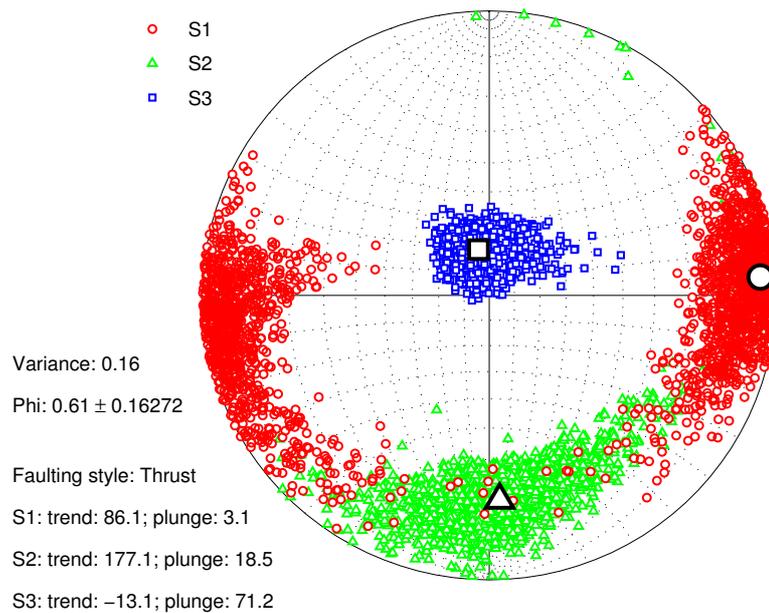
Figure 6.11: Stress inversion of events attributed to the Benioff zone (Figure 6.10) exhibits a thrust regime with an almost vertical direction for σ_3. The solutions for σ_1 and σ_2 show high variability and reflect the varying trends of the thrust events which prevail the input dataset. The small symbols indicate the results of the bootstrap calculations.

interpretation that slab pull (transmission of gravitational forces to the surface plate by guiding stresses within the slab) is the dominant force (CHRISTOVA & SCHOLZ, 2003, CONRAD et al., 2004, BILEK et al., 2005). For northern Chile DELOUIS et al. (1996) report a change from thrust regime to a tensile regime in the slab for depths below 50 km, while in other subduction zones this transition is located in a deeper portion of the subduction zone (CHRISTOVA, 2004). For southern Chile at 37°S, BRUHN (2003) almost exclusively reports thrust events for depths of less than 50 km, while for higher depths the T axis are aligned parallel to the downgoing slab indicating a down-dip extensional regime. The lack of substantially deeper seismicity (which is why there are no fault plane solutions for depths exceeding 65 km) in the area under investigation only allows to conclude that the thrust regime is likely to expand down to 65 km depth. The distribution of P axes for the shallow events in the Benioff zone near the coast of Chiloé Island mainly shows west-east trending directions, while the T axes in this region strike mostly north-south (Figure 6.12). The deeper focal mechanisms (>30 km) are characterized by a higher variability of the P and T axis. The majority of the P axes along the slab are inclined by less than 25°.
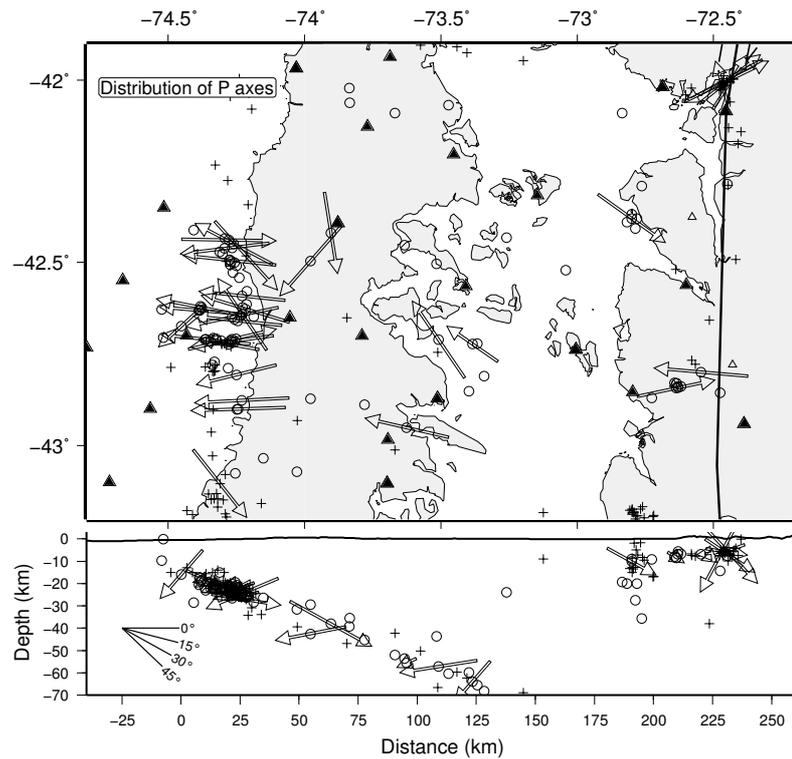
(a) Distribution of P axes. The P axes along the coast of Chiloè Island are mainly striking in east-west direction.
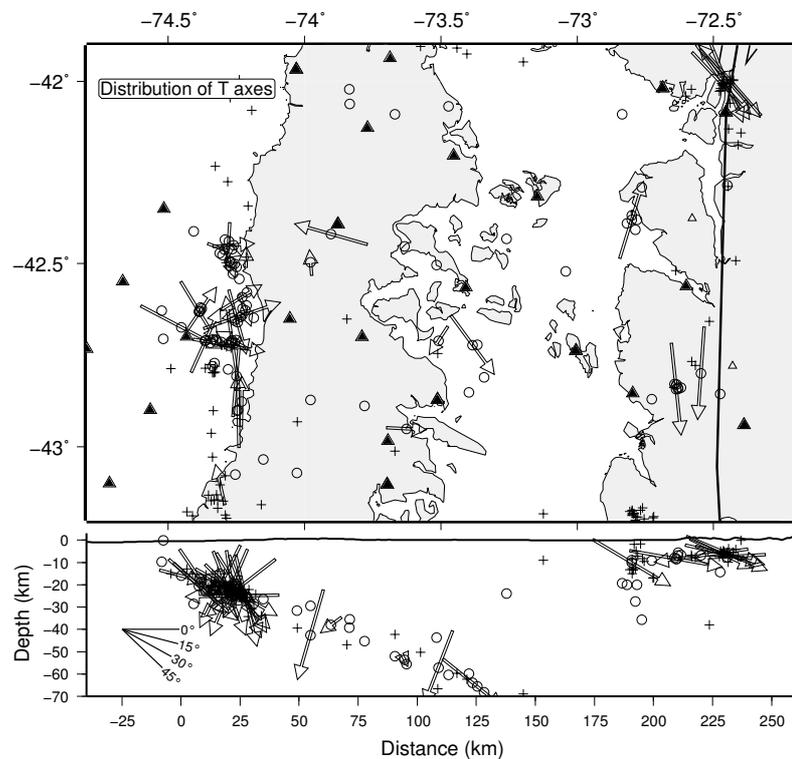
(b) Map shows the distribution of T axes. For the events below 40 km depth no down-dip extension can be identified.

Figure 6.12: Distribution of P and T axes of all fault plane solutions. The lengths of the vectors are shown according to the projection of the respective cross-section.

Chapter 7

Discussion

7.1 Geometry of the Benioff Zone

The data on micro-seismicity obtained from the local network and presented here makes up the first accurate image of the Wadati-Benioff zone in the southern Andes between 41.5° and 43.5°S. The downgoing Nazca plate is readily identifiable as an eastward dipping plane with an inclination of 30–33°. A similar dip (25–31°) of the Wadati-Benioff zone seismicity has been found further to the north at 38°S (BOHM et al., 2002, HABERLAND et al., 2006), where 30 Ma year old lithosphere is currently subducting (MÜLLER et al., 1997). In central Chile the inclination of the shallow part (20–50 km) of the Wadati-Benioff zone ranges typically between 20° and 30° and no significant lateral change of the subduction angle in the upper part of the subduction zone ($\leq$45 km) can be noticed (SUAREZ & COMTE, 1993, PARDO et al., 2002). PARDO et al. (2002) concluded that the shape at the initial part of the subduction seems to be independent of the age of the oceanic plate. Based on the seismicity presented in this study and the observations of HABERLAND et al. (2006), this conclusion is extended to the southern Andes until 43°S. This part the age of the subducting Nazca plate is with 18 Ma much younger than in the central Andes. The subducting Nazca plate in the study area is young, hot and buoyant, thus it was assumed to possibly subduct at low angles. The comparison of the data on local seismicity given by DELOUIS et al. (1996), CAMPOS et al. (2002), COMTE et al. (2002), BOHM et al. (2002), PARDO et al. (2002), HABERLAND et al. (2006) (with inclinations between 18° and 35°) and this study gives a further indication that, at least for the central and southern Chilean subduction zone, plate age and therefore temperature and density of the oceanic lithosphere do not control the initial subduction angle of the upper part ($\leq$45 km) of the downgoing plate.
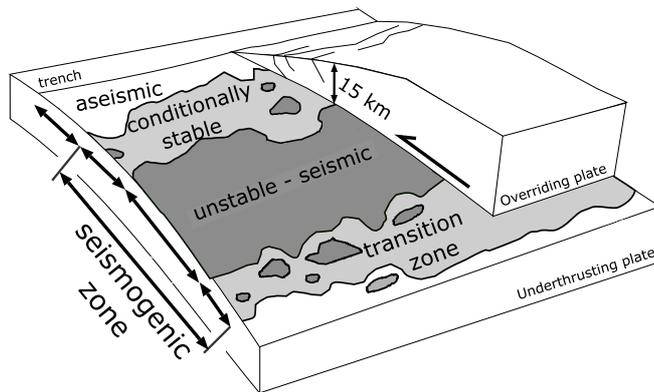
Figure 7.1: Cartoon illustrating the frictional conditions of the subduction thrust fault plane (BILEK & LAY, 2002) and the seismogenic zone. The conditionally stable regime can accumulate strain without complete relaxation by creep and ruptures during large earthquakes. Modified after BILEK & LAY (2002) and BACHMANN (2007).

7.2   Seismogenic Zone: Shallow Part

The seismogenic zone is the shallow part of subduction zones where the most destructive earthquakes emerge (e. g. DIXON & MOORE, 2007). In the following the term "seismogenic zone" is used to refer to that zone which ruptures during major earthquakes with thrust events (HOUSE & JACOB, 1983, BYRNE et al., 1992). By using this definition, the seismogenic zone can be observed only during the coseismic part of the seismic cycle or by aftershock observations (e.g. HUSEN et al., 1999, DESHON et al., 2003). BILEK & LAY (2002) suggest a more detailed model of the seismogenic zone; they propose an internal structuring of the shallow part of the seismogenic zone consisting of a conditionally stable (accumulating strain without relaxation by creep) and an unstable frictional part (Figure 7.1). Following the model of BILEK & LAY (2002), the area located in a conditionally stable regime should be aseismic during the inter-seismic. The seismicity, which was observed during the 11-month deployment of the array, captures only a small inter-seismic time window of the complete seismic cycle which is estimated to be 375 years for Southern Chile (CISTERNAS et al., 2005); therefore the extent of the seismogenic zone cannot be determined by referring to the observed (interseismic) seismicity alone.

The highest seismicity rate is found 10 km to the west of Chiloé Island in a narrow strip within a depth range of 12 km to 30 km (region 3 in Figure 5.9). The thrust-type character of these events and their shallow position allocate them in the coupling or seismogenic zone between the two plates. However, since estimates for the width of the rupture plane of the 1960 earthquake range between 125 and 150 km (PLAFKER & SAVAGE, 1970, BARRIENTOS & WARD, 1990), these events occur only in a certain part of the seismogenic zone. Accordingly, the aseismic region (region 2 in Figure 5.9) west of this zone of high seismicity might correspond to a region with aseismic frictional afterslip (HSU et al., 2006) or in a conditionally stable regime (SCHOLZ, 1998), which can accumulate substantial strain in weak material without complete creep relaxation (BILEK & LAY,

2002).

Further indication that the aseismic region is located mainly within the 1960 rupture zone can be deduced from other studies. Petrological findings assume the seismogenic zone to be temperature-controlled. HYNDMAN & WANG (1993) suggest the upper limit of the seismogenic zone to be strongly temperature-dependent by the transformation of smectite to illite and chlorite which occurs between 100°C and 150°C. The temperature distribution for southern Chile calculated by OLESKEVICH et al. (1999) shows that 100°C is already reached 25 km east of the trench, further indicating that the inter-seismically observed aseismic zone (region 2 in Figure 5.9) is located within the seismogenic zone. Additionally, this conclusion is supported by results from GPS observations (KLOTZ et al., 2001, KHAZARADZE & KLOTZ, 2003) which show a 100% locked plate interface eastwards of the trench. This result points to a conditionally stable frictional regime and excludes the possibility of substantial aseismic slip during the last decade. Therefore the aseismic zone in the working area is interpreted as being in a frictional conditionally stable regime. Furthermore I suggest that the pronounced seismicity cluster below the coast of Chiloé Island exhibits the transition from a conditionally stable to unstable (seismic) frictional regime as outlined by BILEK & LAY (2002). Figure 7.2 shows the extent of the seismogenic zone and the suggested location of the frictional regimes.

As possible mechanisms for the changeover from aseismic to seismic behaviour near Chiloé Island the following ones are suggested:

- Change of the physical properties of the plate interface with depth (e.g. pore pressure or sediment properties)
- Temperature-dependent changes of the material, especially the dehydration of stable sliding clays (HYNDMAN et al., 1993)
- Deformation of the slab (e.g. bending of the oceanic plate with its interface)
- The relation of the seismicity to a so far unknown fault. Such crustal faults have been described in other subduction zones (e.g. Nankai: PARK et al., 2007, Sumatra: SEEBER et al., 2007)

Since one has little information on the in-situ properties of the thrust plane (e.g. OLESKEVICH et al., 1999) and no evidence for bending or the existence of a crustal fault like in Japan (PARK et al., 2002), the processes behind the turnover from an aseismic to seismic regime remains unresolved.
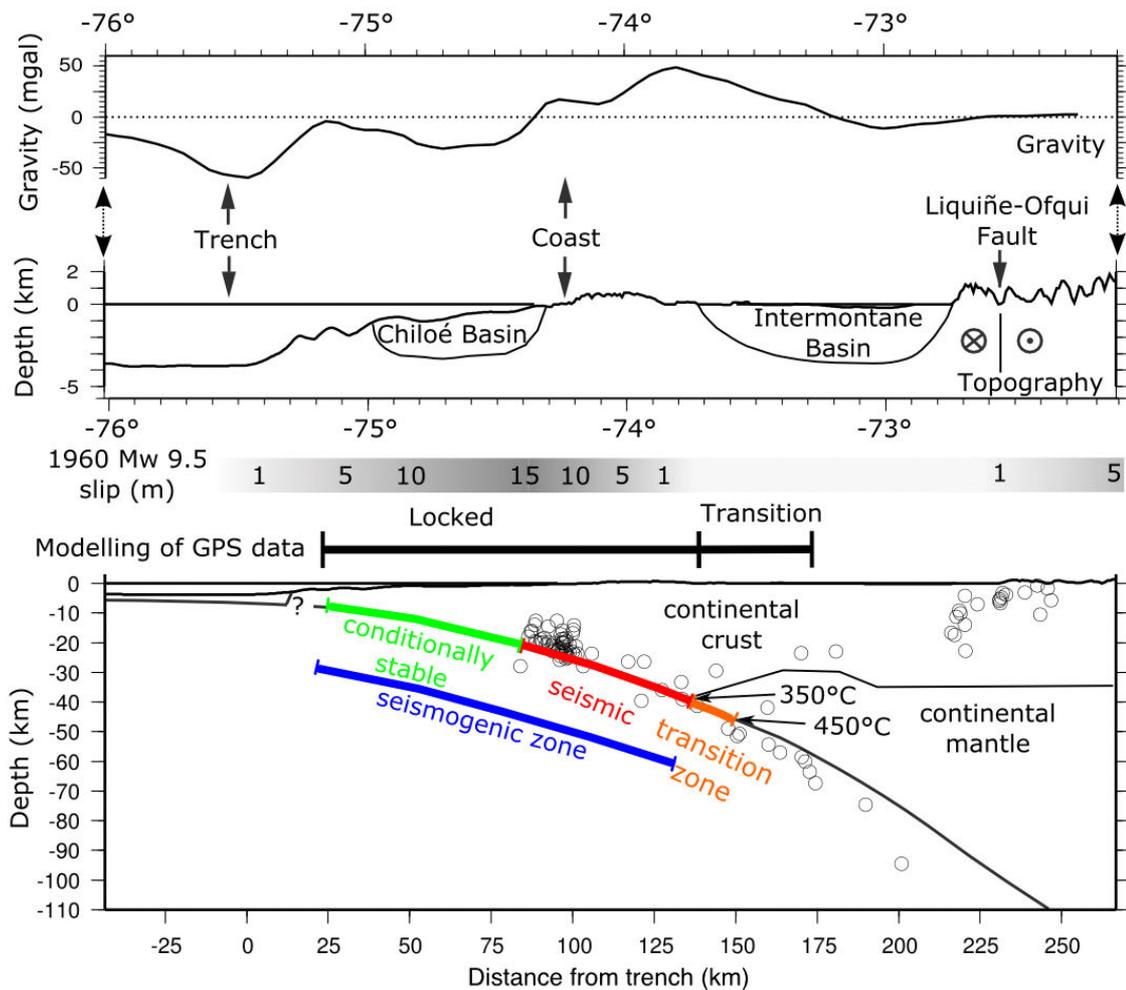
Figure 7.2: Extent of the seismogenic zone and its frictional regimes. Top: Gravity profile (Free Air anomaly offshore/Bouguer anomaly onshore, SCHMIDT & GÖTZE, 2006) and topographic profile along 42.5°S with sedimentary basins (GONZÁLEZ, 1990). Middle: Slip of the 1960 earthquake (BARRIENTOS & WARD, 1990) inferred from topographic levelling, Elastic Dislocation Model from GPS data (KHAZARADZE & KLOTZ, 2003). Bottom: Interpreted location of the seismogenic zone and frictional regimes. Only events inside the network are shown. The down-dip end of the seismogenic zone is inferred from temperature modelling (VÖLKER et al., 2007). See text for more information.

7.3   Seismogenic zone: Down-dip End

Although the seismicity rate drops at a depth below 30 km depth (Figure 5.9, bottom), a clear down-dip end of the seismogenic zone based on the seismicity distribution can hardly be defined. Taking only into account events with GAP≤180° (circles in Figure 5.9), one would place the down dip-end at about 25–30 km depth. The sparse events with depths of between 30 and 50 km (region 4 in Figure 5.9) are most likely associated to intra-plate (intermediate depth) seismicity as further north in Chile (CAMPOS et al., 2002, HABERLAND et al., 2006). However, it should be noted that two events (at 42 and 55 km depth) show thrust-type mechanisms actually not anticipated for intra-plate events at this depth range in the South American subduction zone where down-dip extension along the slab is mostly observed. Since both events are clearly located within the subducting slab, they could be indicative of dehydration processes in the subducting mantle, which is thought to be the cause for the occurrence of a double seismic zone in northern Chile (COMTE et al., 1999, RIETBROCK & WALDHAUSER, 2004). Nevertheless, the seismicity diminishes significantly at a depth below 70 km. Further to the north, at 38°S, intermediate depth (micro-)seismicity terminates at 120 km depth (HABERLAND et al., 2006) and reaches down to depths of 200 km in northern Chile (e. g. COMTE et al., 1999). It has been previously proposed that intermediate-depth earthquakes are related to phase transformations and dehydration reactions and are thus strongly temperature-dependent (KIRBY et al., 1996, HACKER et al., 2003). We therefore associate the diminishing of the seismicity at a depth below 70 km to reflect the relatively high temperature of the downgoing slab at this latitude.

The down-dip limit of thrust earthquakes is generally considered to be a function of the temperature at the plate interface (e. g. SCHOLZ, 1990) and is presumably a transition from unstable to stable sliding along the plate interface (e. g. TICHELAAR & RUFF, 1993) or limited by the intersection of the subduction thrust with hydrated minerals (serpentinite) from the forearc mantle (HYNDMAN et al., 1997, PEACOCK & HYNDMAN, 1999). HYNDMAN et al. (1997) estimate the maximum temperature for seismic behaviour regardless of the presence of water to be 350°C, while large earthquakes may propagate with decreasing slip down to the 450°C isotherm. Recently VÖLKER et al. (2007) calculated the temperature field for the study area by using the geometry of the slab from LANGE et al. (2007) and the position of the continental MOHO (inferred by gravity modelling) from TASSARA et al. (2006). VÖLKER et al. (2007) allocate the 350°C and 450°C isotherm to 40 km and 45 km depth, respectively. According to the temperature model from VÖLKER et al. (2007), the seismogenic zone is located entirely beneath the forearc and is much narrower than proposed by OLESKEVICH et al. (1999).

The shallowest few kilometres of the plate interface are often observed to be aseismic

(YOSHII, 1979, CHEN et al., 1982, BYRNE et al., 1992, PACHECO et al., 1993, SUYE-HIRO & NISHIZAWA, 1994) and have been attributed to underplating of semi-consolidated and unconsolidated sediments (BYRNE et al., 1988) or to a conditionally stable regime in conjunction with an aseismic zone (BILEK & LAY, 2002). Recent studies from Japan and Cascadia using GPS and seismological broadband networks reveal energy release radiated in long frequency and tremor activity in subduction zones. Occasionally, the downgoing tectonic plate moves slowly and almost silently under the overriding plate, accompanied by weak tremors (HEKI et al., 1997, MELBOURNE & WEBB, 2003, ROGERS & DRAGERT, 2003, IDE et al., 2007). These episodes of tremors and slow slip are sometimes associated with as much deformation as caused by a magnitude M_w 8.2 earthquake (HIROSE & OBARA, 2006, HSU et al., 2006). Recent works describe these slow movements to occur on the up-dip limit of the coupled zone (HSU et al., 2006) but also directly below the asperities of mega-thrust earthquakes (ITO et al., 2007). In contrast to the upper part of the Benioff zone, the possibility of aseismic slip cannot be excluded for the deeper part of the area under investigation. Westward moving GPS sites south of 38°S, located 300–400 km landward of the 1960 rupture region, suggest a post-seismic mantle stress relaxation or silent slip events on the plate interface at large depths (KHAZARADZE et al., 2002). All waveforms covering the 11-month observation period were visually revised for signs of slow slip events or tremor activity, but no evidence for this kind of seismic activity could be identified for the area under investigation.

7.4 Recent Deformation along the LOFZ

With the temporary seismic network seismicity with magnitudes of up to M_w 3.8 occurring in several distinct spatial clusters along the LOFZ and the volcanic arc were detected. The main cluster of seismicity is spatially located within the LOFZ which indicates the ongoing activity at this prominent intra-arc shear zone. Strike-slip mechanisms support the hypothesis of stress partitioning due to oblique subduction (BECK JR et al., 1993) or ridge subduction (NELSON et al., 1994). Focal mechanisms derived from teleseismic and local data show similar strike-slip mechanisms for the whole extension of the LOFZ. Location and the strike-slip mechanism of events in two other clusters suggest that NE-SW trending secondary faults related with the LOFZ are currently active (Figure 6.6). This direction and mapped NE-SW trending faults, which are observed at the surface, suggest the possibility of a local duplex structure as indicated in Figure 7.3. The observed deformation along the LOFZ suggests a confirmation for the proposed northward movement of the forearc sliver acting as a detached continental micro-plate as outlined by FORSYTHE & NELSON (1985) and BECK JR et al. (1993). The recent activity in the central part of the LOFZ revealed by local seismicity together with the recent strong event (M_w=6.2) from
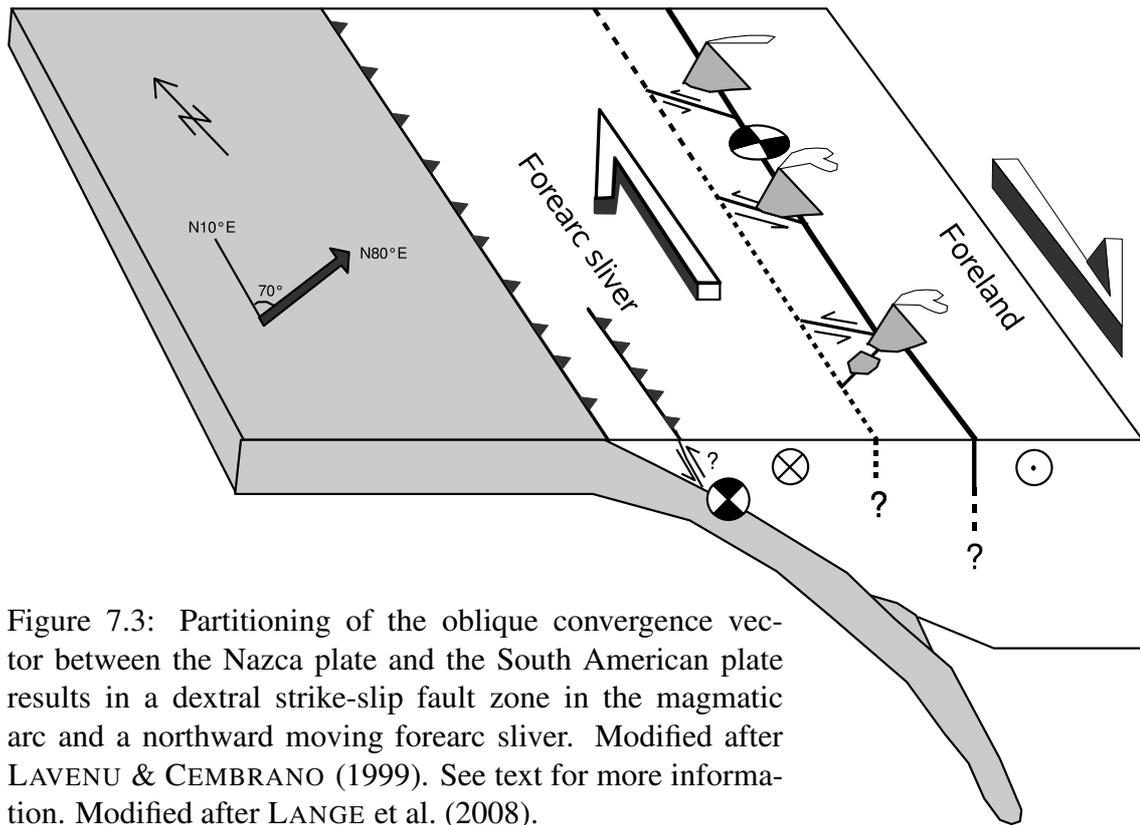
Figure 7.3: Partitioning of the oblique convergence vector between the Nazca plate and the South American plate results in a dextral strike-slip fault zone in the magmatic arc and a northward moving forearc sliver. Modified after LAVENU & CEMBRANO (1999). See text for more information. Modified after LANGE et al. (2008).

April 21, 2007 at the southern part of the LOFZ should be taken into account for future hazard analysis.

7.5 2-D Subduction Zone Structure

The 2-D local earthquake inversion was carried by out using SIMULPS (EVANS et al., 1994). Sedimentary basins like the Chiloé basin and the longitudinal valley emerge with low velocities in the v_p model. The deeper parts of the v_p model show inclined contour lines in the western part of the model following the course of downgoing slab. While in the western part of the model the contour line is inclined following the downgoing course of the slab in the the eastern part of the model the contour lines shows a "bulge". Following the assumption that the 7.8 km/s contourline follows the continental crustal/mantle boundary below Chiloé Island, the bulge suggests an indication for a shallow position from approximately 30 km below the eastern side of Chiloé Island and a slightly deeper location of 35 km in the direction of the magmatic arc with the LOFZ. Recent v_p models from the northern TIPTEQ study areas (38°S) derived from local earthquake tomography (BOHM, 2004, HABERLAND et al., 2006) indicate a similar high velocity feature below the longitudinal valley (Figure 5.19). The velocity models from these two sections suggests that the mantle bulge is a local feature along the southern Chilean subduction zone. Following the proposed model for the temperature dependence of the seismogenic zone

(HYNDMAN et al., 1997, OLESKEVICH et al., 1999) which locates the down-dip limit be-
low the 350° isotherm, and above the crustal mantle/slab intersection, the down-dip limit
would be at approximately 40 km depth (Figure 7.2) adjacent to a ∼20 km wide transition
zone down to the 450° isotherm at 45 km depth (VÖLKER et al., 2007).

Chapter 8

Conclusion

The southern TIPTEQ passive seismic experiment acquired a high-quality data set during an eleven months observation period. Since subduction starts at the trench, a combined on-/offshore network was deployed. A seismological picture of the shallow structure of a previously unknown segment of the southern Chilean subduction zone is presented.

The distribution of micro-seismicity reveal the inclination ($\sim$30°) of the shallow (12–70 km) part of the Benioff zone where thrust mechanisms dominate the stronger events. Therefore the seismicity is interpreted as occurring near the plate interface between continental forearc and oceanic crust. In accordance with petrophysical models (HACKER et al., 2003) the relatively high temperature of the oceanic plate at this latitude seems to control the occurrence (and the down-dip end) of the intermediate depth seismicity. Intense shallow seismicity can be associated with a lower or central part of the seismogenic zone (the interface between upper and lower plate rupturing in large earthquakes).

The subduction zone below the trench and the eastern part of Chiloé Island seems to be in two different frictional regimes. The western part of the current aseismic region between the trench and the seismic cluster near the coast of Chiloé Island which ruptured during the 1960 earthquake is suggested to be in a conditionally frictional region, while the pronounced coastal-parallel seismicity cluster marks a changeover to a seismically frictional regime at higher depths. A high-quality subset of 117 events was used for the 2-D local earthquake tomography of v_p which resolves the Chiloé basin, the sedimentary basin of the longitudinal valley, and yields high velocities below the longitudinal valley suggesting a mantle "bulge".

Moderate seismicity in the continental crust is spatially related with young volcanoes and indicates recent activity of the LOFZ. Events with magnitudes of up to M_l 3.8 occurring near the city of Hornopirén indicate actual seismic activity of the fault zone for the first time. Moment tensor inversion for these shallow, weak events could be successfully inverted. The focal mechanisms show mainly strike-slip mechanisms and SW-NE orientated σ_1. This direction and the stress field determined by stress tensor inversion are in line

with the stress inversion from mylonitic lineaments (CEMBRANO et al., 2000) suggesting a stable tectonic strike-slip regime along the fault zone at this latitude. The seismicity distribution and the focal mechanisms of the shallow crustal events support the model of the forearc acting as a northward moving crustal sliver.

Bibliography

ADRIASOLA, A., THOMSON, S., BRIX, M., HERVÉ, F. AND STÖCKHERT, B. (2006). Postmagmatic cooling and late Cenozoic denudation of the North Patagonian Batholith in the Los Lagos region of Chile, 41°–42°15'S. International Journal of Earth Sciences, **95**(3), 504–528.

AKI, K. AND LEE, W. H. K. (1976). Determination of three-dimensional velocity anomalies under a seismic array using first P arrival times from local earthquakes, 1. a homogeneous initial model. J. Geophys. Res., **81**, 4.381–4.399.

AKI, K. AND RICHARDS, P. G. (2002). Quantitative Seismology - Theory and Methods. University Science Books, second edition, Sausalito, California.

AKI, K., CHRISTOFFERSEN, A. AND HUSEBYE, E. S. (1976). Three-dimensional seismic structure of the lithosphere under Montana LASA. Bull. Seismol. Soc. Am., **66**, 501–524.

ANGERMANN, D., KLOTZ, J. AND REIGBER, C. (1999). Space-geodetic estimation of the Nazca-South America Euler vector. Earth Plan. Sci. Lett., **171**(3), 329–334.

ASCH, G. (1998). Präzise und schnelle Herdparameterbestimmung - eine Herausforderung an die moderne Seismologie. Habilitationsschrift, Freie Universität Berlin.

BACHMANN, R. (2007). Anatomy of an ancient subduction channel in the depth range of its seismogenic coupling zone – insights from field studies in the Swiss Alps and Southern Chile. Ph.D. thesis, Freie Universität Berlin. submitted.

BACKUS, G. AND MULCAHY, M. (1976). Moment Tensors and other Phenomenological Descriptions of Seismic Sources–I. Continuous Displacements. Geophys. J. R. Astr. Soc., **46**, 341–361.

BAKUN, W. H. AND JOYNER, W. B. (1984). The M_L scale in central California. Bull. Seismol. Soc. Am., **75**(5), 1.827–1.843.

BANGS, N. L. AND CANDE, S. C. (1997). Episodic development of a convergent margin inferred from structures and processes along the southern Chile margin. Tectonics, **16**(3), 489–503.

BARAZANGI, M. AND ISACKS, B. L. (1976). Spatial distribution of earthquakes and subduction of the Nazca Plate beneath South America. Geology, **4**(11), 686–692.

BAROUX, E., AVOUAC, J.-P., BELLIER, O. AND SÉBRIER, M. (1998). Slip-partitioning and fore-arc deformation at the Sunda Trench, Indonesia. Terra Nova, **10**(3), 139–144.

BARRIENTOS, S., VERA, E., ALVARADO, P. AND MONFRET, T. (2004). Crustal seismicity in central Chile. J. of South Am. Earth Sci., **16**(8), 759–768.

BARRIENTOS, S. E. AND ACEVEDO-ARANGUIZ, P. S. (1992). Seismological aspects of the 1988-1989 Lonquimay (Chile) volcanic eruption. Journal of Volcanology & Geothermal Research, **53**(1-4), 73–87.

BARRIENTOS, S. E. AND WARD, S. N. (1990). The 1960 Chile earthquake: inversion for slip distribution from surface deformation. Geophys. J. Int., **103**, 589–598,.

BARRIENTOS, S. E., PLAFKER, G. AND LORCA, E. (1992). Postseismic coastal uplift in southern Chile. Geophys. Res. Lett., **19**(7), 701–704.

BECK JR., M. E. (1983). On the mechanism of tectonic transport in zones of oblique subduction. Tectonophysics, **93**(1-2), 1–11.

BECK JR, M. E., ROJAS, C. AND CEMBRANO, J. (1993). On the nature of buttressing in margin-parallel strike-slip fault systems. Geology, **21**(8), 755–758.

BECK JR., M. E., BURMESTER, R., CEMBRANO, J., DRAKE, R., GARCIA, A., HERVÉ, F. AND MUNIZAGA, F. (2000). Paleomagnetism of the North Patagonian batholith, southern Chile. An exercise in shape analysis. Tectonophysics, **326**(1-2), 185–202.

BILEK, S. L. AND LAY, T. (2002). Tsunami earthquakes possibly widespread manifestations of frictional conditional stability. Geophys. Res. Lett., **29**(14). doi:10.1029/2002GL015215.

BILEK, S. L., CONRAD, C. P. AND LITHGOW-BERTELLONI, C. (2005). Slab pull, slab weakening, and their relation to deep intra-slab seismicity. Geophys. Res. Lett., **32**. L14305, doi:10.1029/2005GL022922.

BOHM, M. (2004). 3-D Lokalbebentomographie der südlichen Anden zwischen 36°und 40°S. Ph.D. thesis, Freie Universität Berlin.

BOHM, M., LÜTH, S., ECHTLER, H., ASCH, G., BATAILLE, K., BRUHN, C., RIETBROCK, A. AND WIGGER, P. (2002). The Southern Andes between 36°and 40°S latitude: seismicity and average seismic velocities. Tectonophysics, **356**(4), 275–289.

BOURGOIS, J., MARTIN, H., LAGABRIELLE, Y., LE MOIGNE, J. AND FRUTOS JARA, J. (1996). Subduction erosion related to spreading-ridge subduction: Taitao peninsula (Chile margin triple junction area). Geology, **24**(8), 723–726.

BRUHN, C. (2003). Momententensoren hochfrequenter Ereignisse in Südchile. Ph.D. thesis, Universität Potsdam.

BYRNE, D. E., DAVIS, D. M. AND SYKES, L. R. (1988). Loci and maximum size of thrust earthquakes and the mechanics of the shallow region of subduction zones. Tectonics, **7**(4), 833–857.

BYRNE, D. E., SYKES, L. R. AND M.DAVIS, D. (1992). Great Thrust Eearthquakes and Aseismic Slip Along the Plate Boundary of the Makran Subduction Zone. J. Geophys. Res., **91**(B1), 449–478.

CAMPOS, J., HATZFELD, D., MADARIAGA, R., LOPEZ, G., KAUSEL, E., ZOLLO, A., IANNACONE, G., FROMM, R., BARRIENTOS, S. AND LYON-CAEN, H. (2002). A seismological study of the 1835 seismic gap in south-central Chile. Phys. Earth Planet. Inter., **132**, 177–195.

CANDE, S. C. AND LESLIE, R. B. (1986). Late Cenozoic tectonics of the southern Chile Trench. J. Geophys. Res., **91**(B1), 471–496.

CARLSON, R. L. AND MILLER, D. J. (2003). Hydrous minerals in the mantle wedge and the maximum depth of subduction thrust earthquakes. Geophys. Res. Lett., **30**(5). doi:10.1029/2002GL016600.

CASERTANO, L. (1963). General characteristics of active Andean volcanoes and a summary of their activities during recent centuries. Bulletin of the Seismological Society of America, **53**(6), 60–631.

CEMBRANO, J., HERVÉ, F. AND LAVENU, A. (1996). The Liquiñe Ofqui fault zone: A long-lived intra-arc fault system in southern Chile. Tectonophysics, **259**, 55–66.

CEMBRANO, J., SCHERMER, E., LAVENU, A. AND SANHUEZA, A. (2000). Contrasting nature of deformation along an intra-arc shear zone, the Liquiñe-Ofqui fault zone, southern Chilean Andes. Tectonophysics, **319**, 129–149.

CEMBRANO, J., LAVENU, A., REYNOLDS, P., ARANCIBIA, G., LÓPEZ, G. AND SAN-
HUEZA, A. (2002). Late Cenozoic transpressional ductile deformation north of the
Nazca-South America-Antarctica triple junction. Tectonophysics, **354**(3-4), 289–314.

CEMBRANO, J., LAVENU, A., YAÑEZ, G., RIQUELME, R., GARCÍA, M., GONZÁLEZ,
G. AND HÉRAIL, G. (2007). Neotectonics. In T. Moreno and W. Gibbons (Eds.), The
Geology of Chile, 231–261. Geologyical Society, London.

CESCA, S., BUFORN, E. AND DAHM, T. (2006). Amplitude spectra moment ten-
sor inversion of shallow earthquakes in Spain. Geophys. J. Int., **166**(2), 839–854.
doi:10.1111/j.1365-246X.2006.03073.x.

CHEN, A. T., FROHLICH, C. AND LATHAM, G. V. (1982). Seismicity of the forearc
marginal wedge (accrertionary prism). J. Geophys. Res., **87**, 3.679–3.690.

CHINN, D. S. AND ISACKS, B. L. (1983). Accurate source depths and focal mechanisms
of shallow earthquakes in western South America and in the New Hebrides island arc.
Tectonics, **2**(6), 529–563.

CHRISTOVA, C. (2004). Stress field in the Ryukyu-Kyushu Wadati-Benioff zone by in-
version of earthquake focal mechanisms. Tectonophysics, **384**(1–2), 175–189.

CHRISTOVA, C. AND SCHOLZ, C. H. (2003). Stresses in the Vanuatu subducting slab:
A test of two hypotheses. Geophys. Res. Lett., **30**(15). doi:10.1029/2003GL017701.

CIFUENTES, I. L. (1989). The 1960 Chilean Earthquakes. J. Geophys. Res., **94**(B1),
665–680.

CIFUENTES, I. L. AND SILVER, P. G. (1989). Low-frequency source characteristics of
the great 1960 Chilean earthquake. J. Geophys. Res., **94**(B1), 643–663.

CISTERNAS, M., ATWATER, B. F., TORREJÓN, F., SAWAI, Y., MACHUA, G., LAGOS,
M., EIPERT, A., YOULTON, C., SALGADO, I., KAMATAKI, T., SHISHIKURA, M.,
RAJENDRAN, C., MAILIK, J. K., RIZAL, Y. AND HUSNI, M. (2005). Predecessors of
the giant 1960 Chile earthquake. Nature, **437**(15), 404–407. doi:10.1038/nature03943.

COMTE, D., PARDO, M., DORBATH, L., DORBATH, C., HAESSLER, H., RIVERA, L.,
CISTERNAS, A. AND PONCE, L. (1992). Crustal seismicity and subduction morphol-
ogy around Antofagasta, Chile: preliminary results from a microearthquake survey.
Tectonophysics, **205**, 13–22.

COMTE, D., DORBATH, L., PARDO, M., MONFRET, T., HAESSLER, H., RIVERA, L.,
FROGNEUX, M., GLASS, B. AND MENESES, C. (1999). A Double-Layered Seismic
Zone in Arica, Northern Chile. Geophys. Res. Lett., **26**(13), 1.965–1.968.

COMTE, D., HAESSLER, H., DORBATH, L., PARDO, M., MONFRET, T., LAVENU, A., PONTOISE, B. AND HELLO, Y. (2002). Seismicity and stress distribution in the Copiapo, northern Chile subduction zone using combined on- and off-shore seismic observations. Phys. Earth Planet. Inter., **132**(1-3), 197–217.

CONRAD, C. P., BILEK, S. AND LITHGOW-BERTELLONI, C. (2004). Great earthquakes and slab pull: interaction between seismic coupling and plate-slab coupling. Earth Plan. Sci. Lett., **218**, 109–122.

CONTRERAS-REYES, E., GREVEMEYER, I., FLUEH, E. R., SCHERWATH, M. AND HEESEMANN, M. (2007). Alteration of the subducting oceanic lithosphere at the southern central Chile trench–outer rise. Geochem. Geophys. Geosyst., **8**(7). doi:10.1029/2007GC001632.

CORVALÁN, J. (1990). Geologic-Tectonic Framework of the Andean Region. In G. E. Ericksen, M. T. Pinochet and J. A. Reinemund (Eds.), Geology of the Andes and its relation to hydrocarbon and mineral resources, 1–12. Earth Science Series, Houston, Texas, USA.

DAHM, T. (1993). Relativmethoden zur Bestimmung der Abstrahlcharakteristik von seismischen Quellen . Ph.D. thesis, University of Karlsruhe.

DAHM, T., MANTHEI, G. AND EISENBLÄTTER, J. (1999). Automated moment tensor inversion to estimate source mechanisms of hydraulically induced micro-seismicity in salt rock. Tectonophysics, **306**(1), 1–17.

DE SAINT BLANQUAT, M., TIKOFF, B., TEYSSIER, C. AND VIGNERESSE, J. L. (1998). Transpressional kinematics and magmatic arcs. Geological Society Special Publication, **135**, 327–340.

DELOUIS, B., CISTERNAS, A., DORBATH, L., RIVERA, L. AND KAUSEL, E. (1996). The Andean subduction zone between 22 and 25°S (northern Chile): Precise geometry and state of stress. Tectonophysics, **259**, 81–100.

DESHON, H. R. AND SCHWARTZ, S. Y. (2004). Evidence for serpentinization of the forearc mantle wedge along the Nicoya Peninsula, Costa Rica. Geophys. Res. Lett., **31**. doi:10.1029/2004GL021179s.

DESHON, H. R., SCHWARTZ, S. Y., BILEK, S. L., DORMAN, L. M., GONZALEZ, V., PROTTI, J. M., FLUEH, E. R. AND DIXON, T. H. (2003). Seismogenic zone structure of the southern Middle America Trench, Costa Rica. J. Geophys. Res., **108**(B10). doi:10.1029/2002JB002294.

DEWEY, J. F. AND LAMB, S. H. (1992). Active tectonics of the Andes. Tectonophysics, **205**(1-3), 79–95.

DEWEY, J. F., HOLDSWORTH, R. E. AND STRACHAN, R. A. (1998). Transpression and transtension zones. Geological Society Special Publication, **135**, 1–14.

Dixon, T. H. and Moore, J. C. (Eds.) (2007). The Seismogenic Zone of Subduction Thrust Faults. Theoretical and Experimental Earth Science Series. Columbia University Press, New York. ISBN: 978-0-231-13866-6.

DZIEWONSKI, A. M., CHOU, T. AND WOODHOUSE, J. (1981). Determination of earthquake source parameters from waveform data for studies of global and regional seismicity. J. Geophys. Res., **86**, 2.825–2.852.

DZIEWONSKI, A. M., EKSTRÖM, G., WOODHOUSE, J. H. AND ZWART, G. (1990). Centroid-moment tensor solutions for January–March 1989 . Phys. Earth Planet. Inter., **59**(4), 233–242.

DZIEWONSKI, A. M., EKSTRÖM, G. AND MATERNOVSKAYA, N. N. (2000a). Centroid-moment tensor solutions for April–June 1999 . Phys. Earth Planet. Inter., **119**, 161–171.

DZIEWONSKI, A. M., EKSTRÖM, G. AND MATERNOVSKAYA, N. N. (2000b). Centroid-moment tensor solutions for January–March 1999. Phys. Earth Planet. Inter., **118**, 1–11.

EBERHART-PHILLIPS, D. (1986). Three-dimensional structure in northern California coast ranges from inversion of local earthquake arrival times. Bull. Seismol. Soc. Am., **76**, 1.025–1.052.

EBERHART-PHILLIPS, D. (1990). Three-dimensional P and S velocity structure in the Coalinga region, California. J. Geophys. Res., **95**(B10), 15.343–15.363.

EBERHART-PHILLIPS, D. (1993). Local earthquake tomography: earthquake source regions. In H. M. Iyer and K. Hirahara (Eds.), Seismic Tomography: Theory and practice. Chapman and Hall, London.

EVANS, J. R., EBERHART-PHILLIPS, D. AND THURBER, C. H. (1994). User's Manual for SIMULPS12 for Imaging V_P and V_P/V_S: A derivative of the "Thurber" tomographic inversion SIMUL3 for local earthquakes and Explosions. U. S. Geological Survey. Open File Report 94–431.

FITCH, T. J. (1972). Plate convergence, Transcurrent faults, and Internal Deformation Adjacent to Southeast Asia and the Western Pacific. J. Geophys. Res., **77**, 4.432–4.461.

FOLGUERA, A., RAMOS, V. A., HERMANNS, R. L. AND NARANJO, J. (2004). Neo-tectonics in the foothills of the southernmost central Andes (37°–38°S): Evidence of strike-slip displacement along the Antiñir-Copahue fault zone. Tectonics, **23**(5), 541–566.

FORSYTHE, R. AND NELSON, E. (1985). Geological manifestations of ridge collision: evidence from the Golfo de Penas–Taitao basin, southern Chile. Tectonics, **4**(5), 477–495.

FOSSEN, H. AND TIKOFF, B. (1998). Extended models of transpression and transtension, and application to tectonic settings. Geological Society Special Publication, **135**, 15–33.

FOSSEN, H., TIKOFF, B. AND TEYSSIER, C. (1994). Strain modeling of transpressional and transtensional deformation. Norsk Geologisk Tidsskrift, **74**(3), 134–145.

FUENZALIDA, A., PARDO, M., CISTERNAS, A., DORBATH, L., DORBATH, C., COMTE, D. AND KAUSEL, E. (1992). On the geometry of the Nazca Plate subducted under Central Chile (32–34.5°S) as inferred from microseismic data. Tectonophysics, **205**, 1–11.

GANSSER, A. (1973). Facts and theories on the Andes: Twenty-sixth William Smith Lecture. Journal of the Geological Society, **129**(2), 93–131.

GEPHARD, J. W. (1990). FMSI: A fortran program for inverting fault/slickenside and earthquake focal mechanism data to obtain the regional stres tensor . Computers and Geosciences, **16**(7), 953–989.

GEPHART, J. W. AND FORSYTH, D. W. (1984). Improved method for determining the regional stress tensor using earthquake focal mechanism data: Application to the San Fernando earthquake sequence. J. Geophys. Res., **89**(B11), 9.305–9.320.

GILBERT, F. (1970). Research Note: Excitation of the Normal Modes of the Earth by Earthquake Sources . Geophys. J. R. Astr. Soc., **22**, 223–226.

GONZÁLEZ, E. (1990). Hydrocarbon Resources in the Coastal Zone of Chile. In G. E. Ericksen, M. T. Pinochet and J. A. Reinemund (Eds.), Geology of the Andes and its relation to hydrocarbon and mineral resources, 383–404. Earth Science Series, Houston, Texas, USA.

GRAEBER, F. (1997). Seismische Geschwindigkeiten und Hypozentren in den südlichen Anden aus der simultanen Inversion von Laufzeitdaten des seismologischen Experiments PISCO 94 in Nordchile. Ph.D. thesis, Freie Universität Berlin. Scientifical Technical Report STR97/17, GeoForschungsZentrum Potsdam.

GRAEBER, F. AND ASCH, G. (1999). Three-dimensional models of P wave velocity and P-to-S velocity ratio in the southern central Andes by simultaneous inversion of local earthquake data. J. Geophys. Res., **104**(B9), 20.237–20.256.

GROSS, K., MICKSCH, U. AND TIPTEQ RESEARCH GROUP, SEISMICS TEAM (2007). The reflection seismic survey of project TIPTEQ – the inventory of the Chilean subduction zone at 38.2°S. Geophys. J. Int. doi:10.1111/j.1365-246X.2007.03680.x, in print.

GUDMUNDSSON, Ó. AND SAMBRIDGE, M. (1998). A regionalized upper mantle (RUM) seismic model. J. Geophys. Res., **103**(B4), 7.721–7.136.

GUIRAUD, M., LABORDE, O. AND PHILIP, H. (1989). Characterization of various types of deformation and their corresponding deviatoric stress tensor using microfault analysis. Tectonophysics, **170**(3–4), 289–316.

HABERLAND, C. (1999). Die Verteilung der Absorption seismischer Wellen in den westlichen Zentralen Anden. Ph.D. thesis, Freie Universität Berlin. Berliner Geowissenschaftliche Abhandlungen, Reihe B, Band 35.

HABERLAND, C. AND RIETBROCK, A. (2001). Attenuation tomography in the western central Andes: a detailed insight into the structure of a magmatic arc. J. Geophys. Res., **106**(B6), 11.151–11.167.

HABERLAND, C., RIETBROCK, A., LANGE, D., BATAILLE, K. AND HOFMANN, S. (2006). Interaction between forearc and oceanic plate at the south-central Chilean margin as seen in local seismic data. Geophys. Res. Lett., **33**. L233023, doi:10.1029/2006GL028189.

HACKER, B. R., PEACOCK, S. M., ABERS, G. A. AND HOLLOWAY, S. D. (2003). Subduction factory 2. Are intermediate-depth earthquakes in subducting slabs linked to metamorphic dehydration reactions? J. Geophys. Res., **108**(B1). doi:10.1029/2001JB001129.

HACKNEY, R., ECHTLER, H., FRANZ, G., GÖTZE, H.-J., LUCASSEN, F., D. M., MELNICK, D., MEYER, U., SCHMIDT, S., TÁŠROVÁ, Z., TASSARA, A. AND WIENECKE, S. (2006). The Segmented Overriding Plate and Coupling at the South-Central Chilean Margin (36°and 42°S). In O. Oncken, G. Chong, G. Franz, P. Giese, H.-J. Götze, V. A. Ramos, M. Strecker and P. Wigger (Eds.), The Andes – Active Subduction Orogeny, 355–374. Springer. doi:10.1007/978-3-540-48684-8_17.

HARDEBECK, J. L. AND HAUKSSON, E. (2001). Stress Orientations Obtained from Earthquake Focal Mechanisms: What Are Appropriate Uncertainty Estimates? Bulletin of the Seismological Society of America, **91**(2), 250–262.

HEKI, K., MIYAZAKI, S. AND TSUJI, H. (1997). Silent fault slip following an interplate thrust earthquake at the Japan Trench. Nature, **386**, 595–598.

HERRON, E. M., CANDE, S. C., AND HALL, B. R. (1981). An active spreading center collides with a subduction zone: A geophysical survey of the Chile margin triple junction. Geol. Soc. Am. Mem., **154**, 683–701.

HERVÉ, F. (1988). Late Paleozoic subduction and accretion in southern Chile. Episodes, **11**(3), 183–188.

HERVÉ, F., GREENE, F. AND PANKHURST, R. J. (1994). Metamorphosed fragments of oceanic crust in the Upper Paleozoic Chonos accretionary complex, southern Chile. J. of South Am. Earth Sci., **7**(3-4), 263–270.

HERVÉ, F., DEMANT, A., RAMOS, V. A., PANKHURST, R.-J. AND SUÁREZ, M. (2000). The Southern Andes. In Cordani, U. G. and Milani, E. J. and Thomaz Filho, A. and Campos, D. A. (Eds.), Tectonic Evolution of South America, 605–634. 31st International Geological Congress, vol. 1, Rio de Jainero – Brazil.

HIROSE, H. AND OBARA, K. (2006). Short-term slow slip and correlated tremor episodes in the Tokai region, central Japan. Geophys. Res. Lett., **33**(17). doi:10.1029/2006GL026579.

HOFFMANN-ROTHE, A., KUKOWSKI, N., DRESEN, G., ECHTLER, H., ONCKEN, O., KLOTZ, J., SCHEUBER, E. AND KELLNER, A. (2006). Oblique convergence along the Chilean margin: Partitioning, margin-parallel faulting and force interaction at the plate interface. In O. Oncken, G. Chong, G. Franz, P. Giese, H.-J. Götze, V. A. Ramos, M. Strecker and P. Wigger (Eds.), The Andes – Active Subduction Orogeny, 125–146. Springer. doi:10.1007/978-3-540-48684-8_6.

HOUSE, L. S. AND JACOB, K. H. (1983). Earthquakes, plate subduction, and stress reversals in the eastern Aleutian arc. J. Geophys. Res., **88**(B11), 9.347–9.373.

HSU, Y.-J., SIMONS, M., AVOUAC, J.-P., GALETZKA, J., SIEH, K., CHLIEH, M., NATAWIDJAJA, D., PRAWIRODIRDJO, L. AND BOCK, Y. (2006). Frictional Afterslip Following the 2005 Nias-Simeulue Earthquake, Sumatra. Science, **312**(5782), 1.921–1.926. doi:10.1126/science.1126960.

HUSEN, S. (1999). Local Earthquake Tomography of a Convergent Margin, North Chile. Ph.D. thesis, Mathematisch-Naturwissenschaftliche Fakultät, Universität Kiel.

HUSEN, S., KISSLING, E., FLUEH, E. AND ASCH, G. (1999). Accurate hypocentre determination in the seismogenic zone of the subducting Nazca Plate in Northern Chile using a combined on-/offshore network. Geophys. J. Int., **138**(3), 687–701.

HUSEN, S., KISSLING, E. AND FLUEH, E. R. (2000). Local earthquake tomography of shallow subduction in north Chile: A combined onshore and offshore study. J. Geophys. Res., **105**(B12), 28.183–28.198.

HYNDMAN, R. D. AND WANG, K. (1993). Thermal constraints on the zone of major thrust earthquake failure: the Cascadia Subduction Zone. J. Geophys. Res., **98**(B2), 2.039–2.060.

HYNDMAN, R. D., WANG, K., YUAN, T. AND SPENCE, G. D. (1993). Tectonic sediment thickening, fluid expulsion, and the thermal regime of subduction zone accretionary prisms: the Cascadia margin off Vancouver Island. J. Geophys. Res., **98**(B12), 21.865–21.876.

HYNDMAN, R. D., YAMANO, M. AND OLESKEVICH, D. A. (1997). The seismogenic zone of subduction thrust faults. Island Arc, **6**(3), 244–260. doi:10.1111/j.1440-1738.1997.tb00175.x.

IDE, S., BEROZA, G. C., SHELLY, D. R. AND UCHIDE, T. (2007). A scaling law for slow earthquakes. Nature, **447**, 76–79. doi: 10.1038/nature05780.

ITO, Y., OBARA, K., SHIOMI, K., SEKINE, S. AND HIROSE, H. (2007). Slow earthquakes coincident with episodic tremors and slow slip events. Science, **315**(5811), 503–506. doi:10.1126/science.1134454.

JAILLARD, E., HÉRAIL, G., MONFRET, T., DÍAZ-MARTÍNEZ, E., BABY, P., LAVENU, A. AND DUMONT, J. F. (2000). Tectonic Evolution of the Andes of Ecuador, Peru, Bolivia and Northermost Chile. In Cordani, U. G. and Milani, E. J. and Thomaz Filho, A. and Campos, D. A. (Eds.), Tectonic Evolution of South America, 481–560. 31st International Geological Congress, vol. 1, Rio de Jainero – Brazil.

JARRARD, R. D. (1986a). Relations among subduction parameters. Rev. of Geophys., **24**(2), 217–284.

JARRARD, R. D. (1986b). Terrane motion by strike-slip faulting of forearc slivers. Geology, **14**(9), 780–783.

JORDAN, T. E., BURNS, W. M., VEIGA, R., PÁNGARO, F., COPELAND, P., KELLEY, S. AND MPODOZIS, C. (2001). Extension and basin formation in the southern Andes caused by increased convergence rate: A mid-Cenozoic trigger for the Andes. Tectonics, **20**(3), 308–324.

JOST, M. AND HERRMANN, R. (1989). A Student's Guide to and Review of Moment Tensors. Seismol. Res. Lett., **60**, 37–57.

JULIAN, B. R., MILLER, A. D. AND FOULGER, G. R. (1998). Non-double-couple earthquakes 1. Theory. Rev. of Geophys., **36**, 525–550.

KANAMORI, H. (1971). Great earthquakes at island arcs and the lithosphere. Tectonophysics, **12**, 187–198.

KANAMORI, H. (1977). The energy release in great earthquakes. J. Geophys. Res., **82**, 2.981–2.988.

KENDRICK, E., BEVIS, M., SMALLEY, R., BROOKS, B., VARGAS, R. B., LAURÍA, E. AND FORTES, L. P. S. (2003). The Nazca-South America Euler vector and its rate of change. J. of South Am. Earth Sci., **16**(2), 125–131.

KENNETT, B. L. N., ENGDAHL, E. R. AND BULAND, R. (1995). Constraints on seismic velocities in the Earth from traveltimes. Geophys. J. Int., **122**, 108–124.

KHAZARADZE, G. AND KLOTZ, J. (2003). Short- and long-term effects of GPS measured crustal deformation rates along the south central Andes. J. Geophys. Res., **108**(B6). doi:10.1029/2002JB001879.

KHAZARADZE, G., WANG, K., KLOTZ, J., HU, Y. AND HE, J. (2002). Prolonged post-seismic deformation of the 1960 great Chile earthquake and implications for mantle rheology. Geophys. Res. Lett., **29**(22). doi:10.1029/2002GL015986.

KIMURA, G. (1986). Oblique subduction and collision: Forearc tectonics of the Kuril arc. Geology, **14**(5), 404–407.

KIRBY, S., ENGDAHL, E. R. AND DENLINGER, R. (1996). Intermediate-Depth Intraslab Earthquakes and Arc Volcanism as Physical Expressions of Crustal and Uppermost Mantle Metamorphism in Subducting Slabs. In G. E. Bebout, D. W. Scholl, S. H. Kirby and J. P. Platt (Eds.), Subduction Top to Bottom, Geophysical Monograph Series 195–214. American. Geophysical Union, Washington D.C.

KISSLING, E. (1988). Geotomography with local earthquake data. Rev. of Geophys., **26**, 659–698.

KISSLING, E., ELLSWORTH, W. L., EBERHART-PHILLIPS, D. AND KRADOLFER, U. (1994). Initial reference models in local earthquake tomography. J. Geophys. Res., **99**(B10), 19.635–19.646.

KISSLING, E., KRADOLFER, U. AND MAURER, H. (1995). Program VELEST USER'S GUIDE – Short Introduction. Second draft version 5th October 1995,Tech. rep., ETH Zürich, unpublished.

KLOTZ, J., KHAZARADZE, G., ANGERMANN, D., REIGBER, C., PERDOMO, R. AND CIFUENTES, O. (2001). Earthquake cycle dominates contemporary crustal deformation in Central and Southern Andes. Earth Plan. Sci. Lett., **193**(3–4), 437–446.

KRAWCZYK, C. ET AL. (2003). Amphibious seismic survey images plate interface at 1960 Chile earthquake. EOS Trans. Am. Geophys. Union, **84**(32), 301–305.

KRAWCZYK, C. M., MECHIE, J., LÜTH, S., TAVŠÁROVÁ, Z., WIGGER, P., STILLER, M., BRASSE, H., ECHTLER, H. P., ARANEDA, M. AND BATAILLE, K. (2006). Geophysical Signatures and Active Tectonics at the South-Central Chilean Margin. In O. Oncken, G. Chong, G. Franz, P. Giese, H.-J. Götze, V. A. Ramos, M. Strecker and P. Wigger (Eds.), The Andes – Active Subduction Orogeny, 171–192. Springer. doi:10.1007/978-3-540-48684-8_8.

LAGABRIELLE, Y., SUÁREZ, M., ROSSELLO, E. A., HÉRAIL, G., MARTINOD, J., RÉGNIER, M. AND DE LA CRUZ, R. (2004). Neogene to Quaternary tectonic evolution of the Patagonian Andes at the latitude of the Chile Triple Junction. Tectonophysics, **385**, 211–241.

LANGE, D., RIETBROCK, A., HABERLAND, C., BATAILLE, K., DAHM, T., TILMANN, F. AND FLÜH, E. (2007). Seismicity and geometry of the south Chilean subduction zone (41.5°S–43.5°S): Implications for controlling parameters. Geophys. Res. Lett., **34**. L06311, doi:10.1029/2006GL029190.

LANGE, D., CEMBRANO, J., RIETBROCK, A., HABERLAND, C., DAHM, T. AND BATAILLE, K. (2008). First seismic record for intra-arc strike-slip tectonics along the Liquiñe-Ofqui fault zone at the obliquely convergent plate margin of the southern Andes. Tectonophysics. doi: 10.1016/j.tecto.2008.04.014, in press.

LANGER, H., RAFFAELE, R., SCALTRITO, A. AND SCARFI, L. (2007). Estimation of an optimum velocity model in the Calabro-Peloritan mountains – assessment of the variance of model parameters and variability of earthquake locations. Geophys. J. Int., **170**(3), 1.151–1.164. doi: 10.1111/j.1365-246X.2007.03459.x.

LAVENU, A. AND CEMBRANO, J. (1999). Compressional- and transpressional-stress pattern for Pliocene and Quaternary brittle deformation in fore arc and intra-arc zones (Andes of Central and Southern Chile). Journal of Structural Geology, **21**(12), 1.669–1.691.

LAY, T. AND WALLACE, T. C. (1995). Modern global seismology, volume 58 in International geophysics series. Academic Press, San Diego.

LINDO, R., DORBATH, C., CISTERNAS, A., DORBATH, L., OCOLA, L. AND MORALES, M. (1992). Subduction geometry in central Peru from a microseismicity survey: first results. Tectonophysics, **205**, 23–29.

LOMNITZ, C. (1970). Major earthquakes and tsunamis in Chile during the period 1535 to 1955. Geologische Rundschau, **59**, 938–960.

LOMNITZ, C. (2004). Major Earthquakes of Chile: A Historical Survey, 1535-1960. Seismol. Res. Lett., **75**(3), 368–378.

LÓPEZ-ESCOBAR, L., KILIAN, R., KEMPTON, P. D. AND TAGIRI, M. (1993). Petrography and geochemistry of Quaternary rocks from the Southern Volcanic Zone of the Andes between 41° and 46°S, Chile. Revista Geológica de Chile, **20**(1), 33–55.

LÓPEZ-ESCOBAR, L., CEMBRANO, J. AND MORENO, H. (1995). Geochemistry and tectonics of the Chilean Southern Andes basaltic Quaternary volcanism (37-46°S). Revista Geológica de Chile, **22**(2), 219–234.

LÜTH, S., WIGGER, P. AND ISSA RESEARCH GROUP (2003). A crustal model along 39°S from a seismic refraction profile – ISSA 2000. Revista Geológica de Chile, **30**(1), 83–101.

MCCAFFREY, R. (1992). Oblique plate convergence, slip vectors, and forearc deformation. J. Geophys. Res., **97**(B6), 8.905–8.915.

MCCAFFREY, R., ZWICK, P. C., BOCK, Y., PRAWIRODIRDJO, L., GENRICH, J. F., STEVENS, C. W., PUNTODEWO, S. S. O. AND SUBARYA, C. (2000). Strain partitioning during oblique plate convergence in northern Sumatra: Geodetic and seismologic constraints and numerical modeling. J. Geophys. Res., **105**(B12), 28.363–28.376.

MELBOURNE, T. I. AND WEBB, F. H. (2003). Slow But Not Quite Silent. Science, **300**(5627), 1.886–1.887.

MELNICK, D. AND ECHTLER, H. (2006). Morphotectonic and Geologic Digital Map Compilations of the South-Central Andes (36°–42°S). In O. Oncken, G. Chong, G. Franz, P. Giese, H.-J. Götze, V. A. Ramos, M. Strecker and P. Wigger (Eds.), The Andes – Active Subduction Orogeny, 565–568. Springer. doi:10.1007/978-3-540-48684-8_30.

MENKE, W. (1989). Geophysical data analysis: Discrete inverse theory, volume 45. International geophysics series, Academic Press, San Diego.

MICHAEL, A. J. (1984). Determination of stress from slip data: Faults and folds. J. Geophys. Res., **89**(B13), 11.517–11.526.

MICHAEL, A. J. (1987). Use of focal mechanisms to determine stress: A control study. J. Geophys. Res., **92**(B1), 357–369.

MICHELINI, A. AND McEVILLY, T. V. (1991). Seismological studies at Parkfield I: Simultaneous inversion for velocity structure and hypocenters using cubic B-spline parameterization. Bull. Seismol. Soc. Am., **81**, 524–552.

MOORES, E. M. AND TWISS, R. J. (1995). Tectonics. W.H. Freeman and Company, New York. ISBN: 0-7167-2437-5.

MORDOJOVICH, C. (1981). Sedimentary Basins of Chilean Pacific Offshore. in Energy Resources of the Pacific Region: American Association of Petroleum Geologists, Studies in Geology, **12**, 732–749.

MPODOZIS, C. AND RAMOS, V. A. (1990). The Andes of Chile and Argentina. In G. E. Ericksen, M. T. Pinochet and J. A. Reinemund (Eds.), Geology of the Andes and its relation to hydrocarbon and mineral resources, 59–90. Earth Science Series, Houston, Texas, USA.

MÜLLER, G. (1985). The reflecticity method: a tutorial. J. Geophys., **58**, 153–174.

MÜLLER, R. D., ROEST, W. R., ROYER, J.-Y., GAHAGAN, L. M. AND SCLATER, J. G. (1997). Digital isochrons of the world's ocean floor. J. Geophys. Res., **102**(B2), 3211–3214. `ftp://ftp.es.usyd.edu.au/pub/agegrid/`.

MUÑOZ, A. (2003). Low temperature Thermal History and Denudation along the Liquiñe-Ofqui Fault Zone in the southern Chilean Andes, 41–42°S. Ph.D. thesis, Ruhr-Universität Bochum.

MURDIE, R. E. AND RUSSO, R. M. (1999). Seismic anisotropy in the region of the Chile margin triple junction. J. of South Am. Earth Sci., **12**(3), 261–270.

MURDIE, R. E., PRIOR, D. J., STYLES, P., FLINT, S. S., PEARCE, R. G. AND AGAR, S. M. (1993). Seismic responses to ridge-transform subduction: Chile triple junction. Geology, **21**(12), 1.095–1.098.

NARANJO, J. A. AND STERN, C. R. (2004). Holocene tephrochronology of the southernmost part (42°30'–45°S) of the Andean Southern Volcanic Zone. Revista Geológica de Chile, **31**(2), 225–240.

NELSON, E., FORSYTHE, R. AND ARIT, I. (1994). Ridge collision tectonics in terrane development. J. of South Am. Earth Sci., **7**(3-4), 271–278.

OBANA, K., KODAIRA, S. AND KANEDA, Y. (2005). Seismicity in the incoming/subducting Philippine Sea plate off the Kii Peninsula, central Nankai trough. J. Geophys. Res., **110**(B11311). doi:10.1029/2004JB003487.

OLESKEVICH, D. A., HYNDMAN, R. D. AND WANG, K. (1999). The updip and downdip limits to great subduction earthquakes: Thermal and structural models of Cascadia, south Alaska, SW Japan, and Chile. J. Geophys. Res., **104**(B7), 14.965–14.991.

ORTIZ, R., MORENO, H., GARCÍA, A., FUENTEALBA, G., ASTIZ, M., PEÑA, P., SÁNCHEZ, N. AND TÁRRAGA, M. (2003). Villarrica volcano (Chile): Characteristics of the volcanic tremor and forecasting of small explosions by means of a material failure method. Journal of Volcanology & Geothermal Research, **128**, 247–259.

PACHECO, J. F., SYKES, L. R. AND SCHOLZ, C. H. (1993). Nature of seismic coupling along simple plate boundaries of the subduction type. J. Geophys. Res., **98**(B8), 14.133–14.159.

PANKHURST, R. J., HERVE, F., ROJAS, L. AND CEMBRANO, J. (1992). Magmatism and tectonics in continental Chiloé, Chile (42°–42°30'S). Tectonophysics, **205**(1-3), 283–294.

PANKHURST, R. J., WEAVER, S. D., HERVÉ, F. AND LARRONDO, P. (1999). Mesozoic-Cenozoic evolution of the North Patagonian Batholith in Aysen, southern Chile. J. of the Geol. Soc., **156**(4), 673–694. doi:10.1144/gsjgs.156.4.0673.

PARDO, M., COMTE, D. AND MONFRET, T. (2002). Seismotectonic and stress distribution in the central Chile subduction zone. J. of South Am. Earth Sci., **15**(1), 11–22.

PARDO-CASAS, F. AND MOLNAR, P. (1987). Relative motion of the Nazca (Farallon) and South American plates since late Cretaceous time. Tectonics, **6**(3), 233–248.

PARK, J.-O., TSURU, T., KODAIRA, S., CUMMINS, P. R. AND KANEDA, Y. (2002). Splay Fault Branching Along the Nankai Subduction Zone. Science, **297**. doi:10.1126/science.1074111.

PEACOCK, S. M. AND HYNDMAN, R. D. (1999). Hydrous minerals in the mantle wedge and the maximum depth of subduction thrust earthquakes. Geophys. Res. Lett., **26**, 2.517–2.520.

PEZZO, E. D. AND PETROSINO, S. (2001). A local-magnitude scale for Mt. Vesuvius from synthetic Wood-Anderson seismograms. J. of Seismology, **5**(2), 207–215. doi:10.1023/A:1011470601970.

PLAFKER, G. (1972). Alaska earthquake of 1964 and Chilean Earthquake of 1960: Implications for arc tectonics . J. Geophys. Res., **77**, 901–925.

PLAFKER, G. AND SAVAGE, J. C. (1970). Mechanism of the Chilean Earthquakes of May 21 and 22, 1960. Geol. Soc. Am. Bull., **81**, 1.001–1.030.

RAMOS, V. A. (2000). The southern Central Andes. In Cordani, U. G. and Milani, E. J. and Thomaz Filho, A. and Campos, D. A. (Eds.), Tectonic Evolution of South America, 561–604. 31st International Geological Congress, vol. 1, Rio de Jainero – Brazil.

RAMOS, V. A. (2005). Seismic ridge subduction and topography: Foreland deformation in the Patagonian Andes. Tectonophysics, **399**, 73–86. doi:10.1016/j.tecto.2004.12.016.

RAMOS, V. A. AND AGUIRRE-URRETA, M. B. (2000). Patagonia. In Cordani, U. G. and Milani, E. J. and Thomaz Filho, A. and Campos, D. A. (Eds.), Tectonic Evolution of South America, 369–380. 31st International Geological Congress, vol. 1, Rio de Jainero – Brazil.

RAMOS, V. A. AND ALEMAN, A. (2000). Tectonic evolution of the Andes. In Cordani, U. G. and Milani, E. J. and Thomaz Filho, A. and Campos, D. A. (Eds.), Tectonic Evolution of South America, 635–685. 31st International Geological Congress, vol. 1, Rio de Jainero – Brazil.

REASENBERG, P. A. AND OPPENHEIMER, D. (1985). Fpfit, fpplot, and fppage: Fortran computer programs for calculating and displaying earthquake fault-plane solutions. Open-File Rep. 85-739, U.S. Geol. Surv.

RICHTER, C. F. (1958). Elementary Seismology. Freeman and Co., San Francisco.

RIETBROCK, A. AND WALDHAUSER, F. (2004). A narrowly spaced double-seismic zone in the subducting Nazca plate. Geophys. Res. Lett., **31**(10). doi:10.1029/2004GL019610.

RIETBROCK, A., SCHERBAUM, F. AND MALONE, S. (1998). The GIANT analysis system (Graphical interactive aftershock network toolbox). Seismol. Res. Lett., **69**(1), 40–45.

RIETBROCK, A., HABERLAND, C., BATAILLE, K., DAHM, T. AND ONCKEN, O. (2005). Studying the Seismogenic Coupling Zone with a Passive Seismic Array. EOS Trans. Am. Geophys. Union, **86**(32), 293–300.

ROGERS, G. AND DRAGERT, H. (2003). Episodic Tremor and Slip on the Cascadia Subduction Zone: The Chatter of Silent Slip. Science, **300**(5627), 1.942–1.943. doi:10.1126/science.1084783.

ROJAS, C., BECK JR, M. E., BURMESTER, R. F., CEMBRANO, J. AND HERVE, F. (1994). Paleomagnetism of the Mid-Tertiary Ayacara Formation, southern Chile: counterclockwise rotation in a dextral shear zone. J. of South Am. Earth Sci., **7**(1), 45–56.

ROSENAU, M., MELNICK, D. AND ECHTLER, H. (2006). Kinematic constraints on intra-arc shear and strain partitioning in the Southern Andes between 38°S and 42°S latitude. Tectonics, **25**, TC4013. doi:10.1029/2005TC001943.

RÖSSLER, D. (2006). Retrieval of Earthquake Source Parameters in Inhomogeneous Anisotropic Media with Application to Swarm Events in West Bohemia in 2000. Ph.D. thesis, University of Potsdam. Scientific Technical Report STR06/09, GeoForschungsZentrum Potsdam.

RÖSSLER, D., KRÜGER, F. AND RÜMPKER, G. (2007). Inversion for seismic moment tensors in anisotropic media using standard techniques for isotropic media. Geophys. J. Int., **169**, 136–148. doi:10.1111/j.1365-246X.2006.03243.x.

RUDLOFF, A. (1998). Bestimmung von Herdflächenlösungen und detaillierte Spannungsinversionen aus ausgewählten Ereignissen des seismologischen Netzes PISCO '94 (Nord-Chile). Ph.D. thesis, Freie Universität Berlin. Scientific Technical Report STR98/01, GeoForschungsZentrum Potsdam.

RUFF, L. J. AND KANAMORI, H. (1988). Introduction to Subducion Zones. Pure Appl. Geophys., **128**(3/4), 459–453.

SANDERSON, D. J. AND MARCHINI, W. R. D. (1984). Transpression. Journal of Structural Geology, **6**(5), 449–458.

SANDWELL, D. T. AND SMITH, W. H. F. (1997). Marine Gravity from Geosat and ERS-1 Altimetry. J. Geophys. Res., **102**, 10.039–10.054.

SCHERWATH, M., FLÜH, E. R., GREVEMEYER, I., TILMANN, F., CONTRERAS-REYES, E. AND WEINREBE, R. W. (2006). Investigating Subduction Zone Processes in Chile. EOS Trans. Am. Geophys. Union, **87**(27), 265–272.

SCHMIDT, S. AND GÖTZE, H.-J. (2006). Bouguer and Isostatic Maps of the Central Andes. In O. Oncken, G. Chong, G. Franz, P. Giese, H.-J. Götze, V. A. Ramos, M. Strecker and P. Wigger (Eds.), The Andes – Active Subduction Orogeny, 559–562. Springer. doi:10.1007/978-3-540-48684-8_28.

SCHOLZ, C. (1990). The mechanics of earthquakes and faulting. Cambridge Univ. Press.

SCHOLZ, C. H. (1998). Earthquakes and friction laws. Nature, **391**, 37–42.

SCHOLZ, C. H. (2002). The Mechanics of Earthquakes and Faulting, 2nd Edition. University Press, Cambridge, UK.

SCHURR, B. (2000). Seismic structure of the central Andean subduction zone from local earthquake data. Ph.D. thesis, Freie Universität Berlin. Scientific Technical Report 01/01, GeoForschungsZentrum Potsdam.

SCHURR, B. AND NÁBĚLEK, J. (1999). New techniques for the analysis of earthquake sources from local array data with an application to the 1993 Scotts Mills, Oregon aftershock sequence. Geophys. J. Int., **137**, 585–600.

SCHURR, B., ASCH, G., RIETBROCK, A., KIND, R., PARDO, M., HEIT, B. AND MONFRET, T. (1999). Seismicity and Average Velocities beneath the Argentine Puna Plateau. Geophys. Res. Lett., **26**(19), 3.025–3.028.

SEEBER, L., MUELLER, C., FUJIWARA, T., ARAI, K., SOH, W., DJAJADIHARDJA, Y. S. AND CORMIER, M.-H. (2007). Accretion, mass wasting, and partitioned strain over the 26 Dec 2004 M_w 9.2 rupture offshore Aceh, northern Sumatra. Earth Plan. Sci. Lett., **263**, 16–31. doi:10.1016/j.epsl.2007.07.057.

SERNAGEOMIN (2003). Mapa Geológico de Chile: versión digital, N°4, CD-ROM, versión 1.0. Servicio Nacional de Geología y Minería, Publicación Geológica Digital, Santiago, Chile.

SIEBERT, L. AND SIMKIN, T. (2002). Volcanoes of the World: An Illustrated Catalog of Holocene Volcanoes and their Eruptions. Smithsonian Institution, Global Volcanism Program Digital Information Series. GVP-3. `http://www.volcano.si.edu/world/`.

SILVER, P. G. AND JORDAN, T. H. (1982). Optimal estimation of scalar seismic moment. Geophys. J. R. Astr. Soc., **70**, 755–787.

SIPKIN, S. A. (1982). Estimation of earthquake source parameters by the inversion of waveform data: synthetic waveforms. Phys. Earth Planet. Inter., **30**, 242–259.

SIPKIN, S. A. AND ZIRBES, M. D. (2004). Moment-tensor solutions estimated using optimal filter theory: global seismicity, 2002. Phys. Earth Planet. Inter., **145**, 203–217.

SMITH, W. H. F. AND SANDWELL, D. T. (1997). Global Sea Floor Topography from Satellite Altimetry and Ship Depth Soundings. Science, **277**(5334), 1.956–1.962. doi:10.1126/science.277.5334.1956.

SNOKE, J. A., MUNSEY, J. W., TEAGUE, A. G. AND BOLLINGER, G. A. (1984). A program for focal mechanism determination by combined use of polarity and SV-P amplitude ratio data. Earthquake Notes, **55**(3), 15.

SOBIESIAK, M. (2004). Fault Plane Structure of the 1995 Antofagasta Earthquake (Chile) Derived From Local Seismological Parameters. Ph.D. thesis, Universität Potsdam.

SOMOZA, R. (1998). Updated Nazca (Farallon)-South America relative motions during the last 40 My: Implications for mountain building in the central Andean region. J. of South Am. Earth Sci., **11**(3), 211–215.

STERN, C. R. (2004). Active Andean volcanism: Its geologic and tectonic setting. Revista Geológica de Chile, **31**(2), 161–206.

STICH, D., AMMON, C. J. AND MORALES, J. (2003). Moment tensor solutions for small and moderate earthquakes in the Ibero-Maghreb region. J. Geophys. Res., **108**(B3), 2148. doi:10.1029/2002JB002057.

SUAREZ, G. AND COMTE, D. (1993). Comment on "Seismic Coupling along the Chilean Subduction Zone" by B.W. Tichelaar and L.R. Ruff. J. Geophys. Res., **98**(B9), 15.825–15.828.

SUÁREZ, G., GAGNEPAIN, J., CISTERNAS, A., HATZFELD, D., MOLNAR, P., OCOLA, L., ROECKER, S. W. AND VIODÉ, J. P. (1990). Tectonic deformation of the Andes and the configuration of the subducted slap in central Peru – Results from a microseismic experiment. Geophys. J. Int., **103**, 1–12.

SUYEHIRO, K. AND NISHIZAWA, A. (1994). Crustal structure and seismicity beneath the forearc off northeastern Japan. J. Geophys. Res., **99**(B11), 22.331–22.347.

TÁRRAGA, M., CARNIEL, R., ORTIZ, R., GARCÍA, A. AND MORENO, H. (2006). A dynamical analysis of the seismic activity of Villarrica volcano (Chile) during September-October 2000. Chaos, Solitons & Fractals. doi:10.1016/j.chaos.2006.10.062.

TASSARA, A., GÖTZE, H.-J., SCHMIDT, S. AND HACKNEY, R. (2006). Three-dimensional density model of the Nazca plate and the Andean continental margin. J. Geophys. Res., **111**, doi:10.1029/2005JB003976.

TEBBENS, S. F. AND CANDE, S. C. (1997). Southeast Pacific tectonic evolution from early Oligocene to present. J. Geophys. Res., **102**(B6), 12.061–12.084.

TEYSSIER, C., TIKOFF, B. AND MARKLEY, M. (1995). Oblique plate motion and continental tectonics. Geology, **23**(5), 447–450.

THIERER, P. O., FLUEH, E. R., KOPP, H., TILMANN, F., COMTE, D. AND CONTRERAS, S. (2005). Local earthquake monitoring offshore Valparaiso, Chile. Neues Jahrbuch fur Geologie und Palaontologie - Abhandlungen, **236**(1-2), 173–183.

THOMSON, S. N. (2002). Late Cenozoic geomorphic and tectonic evolution of the Patagonian Andes between latitudes 42°S and 46°S: An appraisal based on fission-track results from the transpressional intra-arc Liquiñe-Ofqui fault zone. Geol. Soc. Am. Bull., **114**(9), 1.159–1.173.

THOMSON, S. N. AND HERVÉ, F. (2002). New time constraints for the age of metamorphism at the ancestral Pacific Gondwana margin of southern Chile (42–52°S). Revista Geológica de Chile, **29**(2), 255–271.

THORNBURG, T. M. AND KULM, L. D. (1987a). Sedimentation in the Chile Trench: Depositional morphologies, lithofacies, and stratigraphy. Geol. Soc. Am. Bull., **98**(1), 33–52.

THORNBURG, T. M. AND KULM, L. D. (1987b). Sedimentation in the Chile Trench: Petrofacies and provenance. Journal of Sedim. Petro., **57**(1), 55–74.

THURBER, C. AND EBERHART-PHILLIPS, D. (1999). Local earthquake tomography with flexible gridding. Comput. & Geosci., **25**, 809–818.

THURBER, C. H. (1983). Earthquake locations and three-dimensional crustal structure in the Coyote Lake area, Central California. J. Geophys. Res., **88**, 8.226–8.236.

THURBER, C. H. (1993). Local earthquake tomography: velocities and V_P/V_S-theory. In H. M. Iyer and K. Hirahara (Eds.), Seismic Tomography: Theory and practicechapter 20, 563–583. Chapman and Hall, London.

TICHELAAR, B. W. AND RUFF, L. J. (1993). Depth of seismic coupling along subduction zones. J. Geophys. Res., **98**(B2), 2.017–2.037.

TIKOFF, B. AND GREENE, D. (1997). Stretching lineations in transpressional shear zones: An example from the Sierra Nevada Batholith, California. Journal of Structural Geology, **19**(1), 29–39.

TILLOTSON, E. (1962). Earthquake Swarm in Chile Beginning in May 1960. Nature, **195**(4843), 763–764. doi:10.1038/195763a0.

TILMANN, F. J., GREVEMEYER, I., FLUEH, E. R., DAHM, T. AND GOSSLER, J. (2007). Seismicity in the outer rise offshore southern Chile: indication of fluid effects in crust and mantle. submitted to Earth Plan. Sci. Lett.

TOOMEY, D. R. AND FOULGER, G. R. (1989). Tomographic inversion of local earthquake data from the Hengill-Grensdalur central volcano complex, Iceland. J. Geophys. Res., **94**, 17.497–17.510.

UM, J. AND THURBER, C. H. (1987). A fast algorithm for two-point ray tracing. Bull. Seismol. Soc. Am., **77**, 972–986.

VÖLKER, D., GREVEMEYER, I., HE, J., WANG, K. AND HEESEMANN, M. (2007). Thermal Regime of the Chilean Subduction Zone at 38°S and 43°S: modeling Results and Implications for Seismicity. In Geophysical Research Abstracts, Vol. 9 (General Assembly Vienna, Austria, April 2007, EGU2007-A-06274). European Geosciences Union.

VON HUENE, R., CORVALÁN, J., FLUEH, E. R., HINZ, K., KORSTGARD, J., RANERO, C. R., WEINREBE, W. AND CONDOR SCIENTISTS (1997). Tectonic control of the subducting Juan Fernandez Ridge on the Andean margin near Valparaiso, Chile. Tectonics, **16**(3), 474–488.

WANG, K., HU, Y., BEVIS, M., KENDRICK, E., SMALLEY JR., R., VARGAS, R. B. AND LAURÍA, E. (2007). Crustal motion in the zone of the 1960 Chile earthquake: Detangling earthquake-cycle deformation and forearc-sliver translation. Geochem. Geophys. Geosyst., **8**. doi:10.1029/2007GC001721.

WESSEL, P. AND SMITH, W. H. F. (1998). New, improved version of the Generic Mapping Tools released. suppl. to EOS, Transactions, AGU, **79**, 579.

WIEMER, S. (2001). A Software Package to Analyze Seismicity: ZMAP. Seismol. Res. Lett., **72**, 373–382. http://www.earthquake.ethz.ch/software/zmap.

WIEMER, S. AND ZÚÑIGA, F. (1994). ZMAP – a software package to analyze seismicity. EOS, Transactions, Fall Meeting, AGU, **75**, 456. http://www.earthquake.ethz.ch/software/zmap.

WWW-BODC (2003). IOC, IHO and BODC, 2003. Centenary Edition of the GEBCO Digital Atlas, published on CD-ROM on behalf of the Intergovernmental Oceanographic Commission and the International Hydrographic Organization as part of the General Bathymetric Chart of the Oceans, British Oceanographic Data Centre, Liverpool, U.K.. http://www.ngdc.noaa.gov/mgg/gebco/.

WWW-NGDC (2007). Surface of the Earth (ETOPO2) 2 minute color relief images. http://www.ngdc.noaa.gov/mgg/global/seltopo.html.

WWW-PDE (2007). Preliminary Determinations of Epicenters, Monthly Listing. http://neic.usgs.gov/neis/epic/epic.html.

WWW-SRTM (2007). SRTM 90m Digital Elevation Data. http://srtm.csi.cgiar.org/SELECTION/inputCoord.asp.

WWWCMT (2007). Global Centroid Moment Tensor database (CMT). `http://www.globalcmt.org/CMTsearch.html`.

YÁÑEZ, G. A., RANERO, C. R., VON HUENE, R. AND DÍAZ, J. (2001). Magnetic anomaly interpretation across the southern central Andes (32°S-34°S): The role of the Juan Fernandez Ridge in the late Tertiary evolution of the margin. J. Geophys. Res., **106**(B4), 6.325–6.345.

YÁÑEZ, G. A., CEMBRANO, J., PARDO, M., RANERO, C. AND SELLES, D. (2002). The Challenger-Juan Fernández-Maipo major tectonic transition of the Nazca-Andean subduction system at 33-34°S: geodynamic evidence and implications. J. of South Am. Earth Sci., **15**, 23–38.

YOSHII, T. (1979). A detailed cross-section of the deep seismic zone beneath northeastern Honshu, Japan. Tectonophysics, **55**, 349–360.

ZEIL, W. (1986). Südamerika. Ferdinand Enke Verlag, Stuttgart. ISBN: 3-432-95861-7.

ZHAO, D. AND KAYAL, J. R. (2000). Impact of seismic tomography on Earth sciences. Current Science, **79**(9), 1.208–1.214.

List of Tables

List of Figures

Appendix A

Appendix

A.1 Distribution of Local Seismic Networks Along the South American Margin

Figure A.1: Distribution of local seismic networks (numbers) along the Chilean/Peruvian subduction zone and TIPTEQ seismic refraction profiles (letters).

Legend:

Local seismic studies:

1 Suarez et al.1990
2 Lindo et al. 1992
3 Comte et al. 1999
4 Delouis et al. 1996
5 Schurr et al. 1999
6 Husen et al. 1999
7 Comte et al. 1992
8 Haberland & Rietbrock 2001
9 Graeber & Asch 1999
10 Pardo et al. 2002
11 Comte et al. 2002
12 Thierer et al. 2005
13 Barrientos et al. 2004
14 Fuenzalida et al. 1992
15 Campos et al. 2002
16 Bohm et al. 2002
17 Haberland et al. 2006
18 Lange et al. 2007
19 Tilmann et al. 2007
20 Tilmann et al. 2007
21 Murdie et al. 93

TIPEQ refraction profiles:

A Contreras–Reyes et al. 07
B Scherwath et al. 2005
C Scherwath et al. 2005
D Krawczyc et al. 2003

A.2 Temporal Distribution of Magnitudes
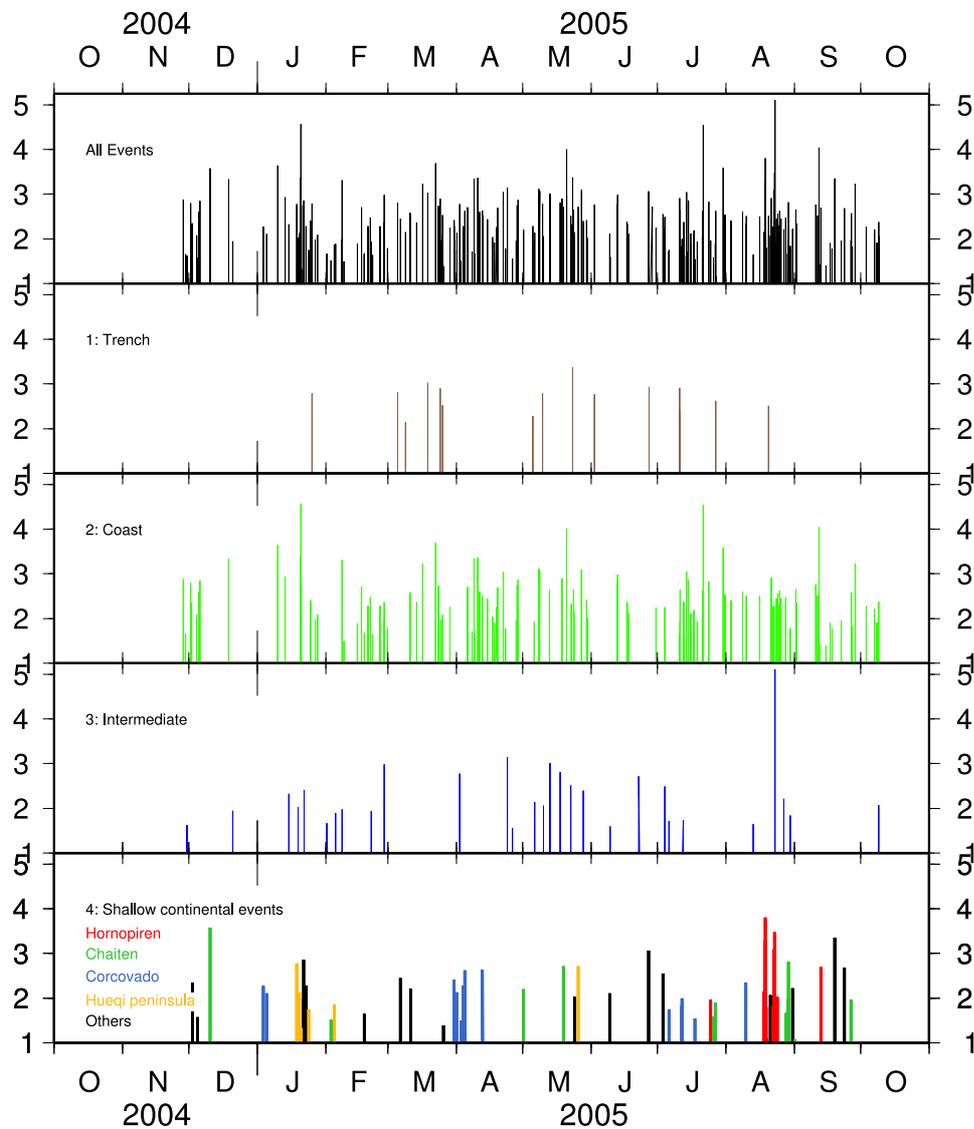
Figure A.2: Magnitudes versus time plotted for different regions. Events below the trench are located west of 74.5°; coastal events have longitudes between -74.5° and -74°; intermediate events are east of -74° and located at depths >30 km.

A.3 Seismicity of 38°S vs. 42°S
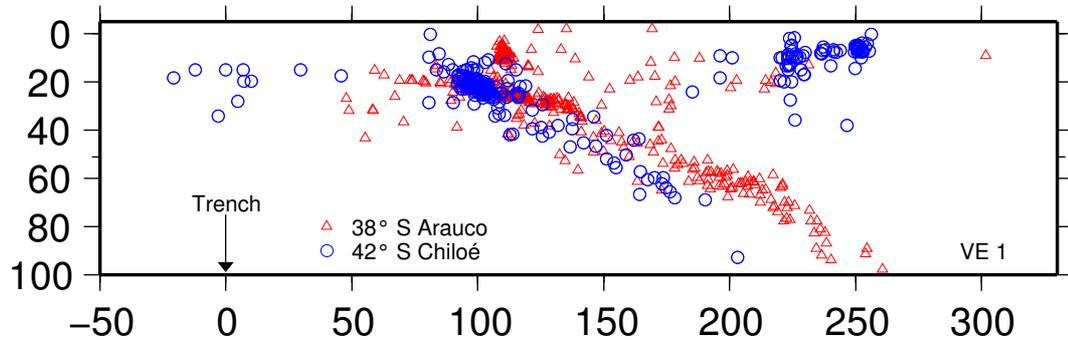
Figure A.3: West-east cross section of seismicity from northern (38°S, HABER-LAND et al. (2006)) versus the seismicity of the southern (42°S, this study) TIPTEQ network. The inclination of the Benioff zone seismicity at 42°S is higher than at 38°S.

A.4 Station Corrections

Table A.1: Station corrections from final joint inversion of 1-D velocity model, hypocentres and station delays. Station S05 was chosen as reference station. Only stations with at least 15 P-arrivals are listed.

station name	P corr. (s)	S corr. (s)	station name	P corr. (s)	S corr. (s)
S05	0.00	0.35	S16	-0.70	-0.90
S01	-0.10	0.06	S18	-0.04	0.30
S02	-0.29	-0.14	S19	-0.67	-0.72
S03	0.04	0.05	S20	-0.45	-0.13
S04	-0.12	0.34	S21	-0.46	-0.51
S06	-0.55	-0.59	202	-0.92	0.00
S08	0.12	1.10	204	0.38	2.17
S09	-0.46	-0.23	208	0.10	0.00
S10	-0.22	-0.07	209	-0.35	0.00
S11	-0.23	-0.05	210	0.43	0.00
S12	-0.47	-0.75	212	-1.30	0.00
S13	0.19	-0.52	213	-1.95	-1.77
S14	-0.47	-0.29	219	-2.29	0.00
S15	-0.43	-0.19	–	–	–

A.5   Focal Mechanism from First-Motion Polarities

Table A.2: Focal mechanism from first-motion polarities.

Date	Time	Latitude	Longitude	Depth	M_l	Strike	Dip	Rake
YYYY-MM-DD	HH:MM:SS.S	(°)	(°)	(km)		(°)	(°)	(°)
2005-01-10	03:36:43.4	-42.4827	-74.2142	27.21	3.64	55	55	100
2005-01-15	07:05:09.5	-42.7231	-73.3841	64.00	2.33	45	85	-100
2005-02-15	05:46:44.3	-42.7246	-74.2770	22.44	1.89	190	5	-90
2005-02-20	02:29:26.6	-42.6505	-74.2662	20.20	2.29	175	50	100
2005-02-25	10:47:52.9	-42.8769	-74.2306	23.53	2.29	150	55	50
2005-02-27	08:47:39.7	-42.4197	-73.9029	38.01	2.98	50	85	50
2005-03-16	18:57:43.3	-43.1029	-74.3099	20.89	3.23	60	70	100
2005-03-22	17:39:03.3	-42.7105	-74.2654	25.47	3.69	145	30	60
2005-04-10	17:27:44.7	-42.7108	-74.3624	23.13	3.36	50	45	160
2005-04-17	10:27:45.2	-42.7161	-74.2657	24.95	2.04	40	70	-160
2005-04-19	10:00:55.0	-42.6604	-74.2456	25.31	2.26	215	75	130
2005-05-06	13:12:58.2	-42.7113	-73.5090	57.16	2.14	35	40	60
2005-05-13	03:51:14.9	-42.8076	-74.2494	23.36	2.64	40	45	-180
2005-05-13	09:08:11.1	-42.9510	-73.6255	55.64	3.02	20	20	100
2005-05-24	04:49:09.7	-42.4390	-74.2777	23.43	2.66	340	50	60
2005-05-24	06:06:09.9	-42.4500	-74.2597	23.27	2.15	50	25	120
2005-06-13	01:47:40.8	-42.6281	-74.2175	25.31	2.98	355	35	60
2005-07-17	16:11:17.2	-42.5925	-74.2298	24.40	2.19	35	25	130
2005-07-21	12:11:44.0	-42.4946	-74.2755	23.90	2.62	345	40	60
2005-07-21	20:24:30.1	-42.6318	-74.3878	20.64	4.55	210	85	120
2005-07-30	17:49:53.0	-42.6239	-74.3780	18.57	3.59	45	40	140
2005-08-08	15:21:41.5	-42.6745	-74.4523	15.95	2.60	0	70	-130
2005-08-10	13:40:11.9	-42.6422	-74.2291	24.46	2.59	200	85	40
2005-08-23	08:44:18.6	-42.4972	-73.9783	42.53	5.11	325	35	110
2005-08-28	02:14:37.8	-42.9013	-74.2439	21.61	2.47	140	65	30
2005-09-12	04:49:22.9	-42.4625	-74.2940	22.72	4.04	180	65	100

A.6   Station List

Table A.3: Summary of the seismic stations (Southern TIPTEQ network).

Station	Data logger	Sensor	Latitude	Longitude	Depth	Start – End	
name	Type/ID/Gain	Type/ID	(°)	(°)	(km)	(YYMMDD)	
S01	EDL/3118/01	L4-3D/1831	-41.96666	-74.03010	158	2004.11.26	2005.03.19
S01	EDL/3036/10	L4-3D/1831	-41.96666	-74.03010	158	2005.03.19	2005.06.24
S01	EDL/3194/01	L4-3D/1831	-41.96666	-74.03010	158	2005.06.24	2005.10.09
S02	EDL/3152/01	L4-3D/1869	-41.93590	-73.68643	50	2004.11.26	2005.10.09
S03	EDL/3084/01	L4-3D/1182	-42.20420	-73.45317	146	2004.11.24	2005.10.09
S04	EDL/3045/01	L4-3D/1172	-42.31655	-73.14535	12	2004.11.25	2005.10.09
S05	EDL/3052/01	L4-3D/1877	-42.12763	-73.76997	131	2004.11.25	2005.10.09
S06	EDL/3085/01	L4-3D/1827	-42.39260	-73.87851	135	2004.11.24	2005.03.20
S06	EDL/3085/10	L4-3D/1827	-42.39260	-73.87851	135	2005.03.20	2005.07.02
S06	EDL/3085/01	L4-3D/1827	-42.39260	-73.87851	135	2005.07.02	2005.10.12
S08	EDL/3151/01	L4-3D/1868	-42.56545	-73.40878	135	2004.11.24	2005.10.09
S09	EDL/3075/01	L4-3D/13621	-42.65171	-74.05378	18	2004.11.24	2005.10.10
S10	EDL/3042/01	L4-3D/1016	-42.87230	-73.51289	31	2004.11.24	2005.03.22

Table continuing on next page ⌒

Table A.3: (continued)

Station	Data logger	Sensor	Latitude	Longitude	Depth	Start – End	
S10	EDL/3042/10	L4-3D/1016	-42.87230	-73.51289	31	2005.03.22	2005.07.03
S10	EDL/3042/01	L4-3D/1016	-42.87230	-73.51289	31	2005.07.03	2005.10.10
S11	EDL/3026/01	L4-3D/1009	-42.70123	-73.78910	155	2004.11.25	2005.09.11
S12	EDL/3077/01	L4-3D/1823	-42.98445	-73.69388	113	2004.11.25	2005.10.10
S13	EDL/3050/01	L4-3D/1188	-43.11391	-73.65999	163	2004.11.25	2005.02.12
S14	EDL/3048/01	L4-3D/1177	-42.01857	-72.68689	23	2004.11.28	2005.02.17
S14	EDL/3048/10	L4-3D/1177	-42.01857	-72.68689	23	2005.02.17	2005.06.30
S14	EDL/3048/01	L4-3D/1177	-42.01857	-72.68689	23	2005.06.30	2008.10.11
S15	EDL/3096/01	L4-3D/1830	-42.08578	-72.45390	40	2004.11.28	2005.02.16
S15	EDL/3096/10	L4-3D/1830	-42.08578	-72.45390	40	2005.02.16	2005.07.01
S15	EDL/3096/01	L4-3D/1830	-42.08578	-72.45390	40	2005.07.01	2005.10.12
S16	EDL/3022/01	L4-3D/1007	-42.56224	-72.59992	10	2004.11.30	2005.10.11
S18	EDL/3073/01	L4-3D/13571	-42.94117	-72.38772	405	2004.12.01	2005.06.29
S18	EDL/3073/10	L4-3D/13571	-42.94117	-72.38772	405	2005.06.29	2005.10.12
S19	EDL/3064/01	L4-3D/13541	-42.85438	-72.79647	15	2004.11.30	2005.02.15
S19	EDL/3050/10	L4-3D/13541	-42.85438	-72.79647	15	2005.02.15	2005.06.28
S19	EDL/3050/01	L4-3D/13541	-42.85438	-72.79647	15	2005.06.28	2005.10.11
S20	EDL/3040/01	L4-3D/1166	-42.73921	-73.00508	16	2004.12.01	2005.02.15
S20	EDL/3040/10	L4-3D/1166	-42.73921	-73.00508	16	2005.02.15	2005.06.29
S20	EDL/3040/01	L4-3D/1166	-42.73921	-73.00508	16	2005.06.29	2005.10.11
S21	EDL/3082/01	L4-3D/2828	-43.10263	-73.69677	10	2004.02.12	2005.03.21
S21	EDL/3082/10	L4-3D/2828	-43.10263	-73.69677	10	2005.03.21	2005.06.26
S21	EDL/3188/01	L4-3D/2831	-43.10263	-73.69677	10	2005.06.26	2005.10.10
202	OBH/0202/01	OAS/74	-43.1328	-75.0827	-1013	2005.02.13	2005.10.04
204	OBS/0204/01	Webb/74	-43.0992	-74.7160	-118	2005.02.13	2005.10.04
207	OBS/0207/01	Webb/2398	-42.3500	-74.5166	-176	2005.02.13	2005.10.02
208	OBH/0208/01	HTI/76	-42.4166	-74.8001	-272	2005.02.13	2005.10.02
209	OBH/0209/01	HTI/53	-42.5498	-74.6668	-908	2005.02.13	2005.10.02
210	OBH/0210/01	HTI/59	-42.7337	-74.7995	-201	2005.02.13	2005.10.03
211	OBS/0211/01	Owen/63	-42.6004	-75.0163	-1079	2005.02.13	2005.04.10
212	OBH/0212/01	HTI/63	-42.7832	-75.1667	-1186	2005.02.13	2005.10.04
213	OBS/0213/01	Owen/62	-43.0004	-75.3333	-2169	2005.02.13	2005.10.04
214	OBS/0214/01	Owen/25	-43.1666	-75.4500	-2641	2005.02.14	2005.10.03
215	OBS/0215/01	Webb/2329	-42.9999	-75.6668	-3740	2005.02.14	2005.10.03
216	OBS/0216/01	Owen/56	-42.8999	-75.8828	-3730	2005.02.14	2005.10.03
217	OBS/0217/01	Owen/54	-42.6848	-75.7341	-3751	2005.02.14	2005.10.03
218	OBS/0218/01	Owen/61	-42.8332	-75.5333	-3741	2005.02.14	2005.10.03
219	OBH/0219/01	HTI/66	-42.6501	-75.3830	-2714	2005.02.14	2005.10.03
220	OBH/0220/01	OAS/6	-42.4335	-75.2493	-2209	2005.02.14	2005.10.03
221	OBS/0221/01	Webb/2352	-42.4835	-75.4999	-3734	2005.02.14	2005.04.08
253	OBS/0253/01	PMD/4	-37.8490	-73.9507	-610	2005.02.20	2005.10.07
254	OBS/0254/01	PMD/0	-37.9008	-74.4003	-2956	2005.02.21	2005.10.07
255	OBH/0255/01	OAS/36	-38.1001	-74.5005	-4125	2005.02.21	2005.10.07
258	OBH/0258/01	HTI/39	-38.3500	-74.5001	-3335	2005.02.21	2005.10.07
259	OBH/0259/01	HTI/27	-38.1502	-74.6338	-4669	2005.02.21	2005.10.07
260	OBH/0260/01	HH/0	-37.9006	-74.6364	NN	2005.02.21	2005.10.07

*   *End of Table A.3: Summary of the seismic stations (Southern TIPTEQ network).*   *

A.7 Event Catalogue

Table A.4: List with local events detected by the network.

Date	Time	Latitude	Longitude	Depth	GAP	RMS	M$_1$
YYMMDD	HH:MM:SS.SS	(°)	(°)	(km)	(°)	[s]	
2004-11-28	13:16:54.00	-41.6056	-74.0953	26.44	323	0.45	2.9
2004-11-29	10:55:00.76	-41.9958	-74.2393	21.24	294	0.19	1.7
2004-11-30	01:28:48.80	-41.7420	-73.5417	44.12	263	0.13	1.6
2004-12-01	18:31:55.22	-41.5460	-74.0916	27.67	300	0.26	2.8
2004-12-02	04:37:50.40	-42.9023	-74.3346	20.68	274	0.19	2.4
2004-12-02	14:49:12.48	-42.0905	-72.8355	19.40	132	0.39	2.4
2004-12-04	10:53:53.13	-41.3680	-73.4114	19.27	295	0.88	2.2
2004-12-04	12:46:09.12	-42.7169	-74.3612	15.63	305	0.53	2.1
2004-12-05	01:11:23.27	-42.2890	-72.4463	9.94	204	0.14	1.6
2004-12-05	10:01:57.39	-42.4983	-74.2882	24.49	237	0.16	2.6
2004-12-06	01:07:53.67	-43.5140	-74.4798	14.76	302	0.49	2.9
2004-12-07	14:52:44.21	-41.1453	-73.0661	15.00	302	0.96	2.4
2004-12-10	17:03:44.95	-42.8437	-72.6369	8.43	134	0.29	3.6
2004-12-14	04:35:49.98	-44.2888	-73.4382	15.00	321	0.40	2.5
2004-12-18	22:02:03.73	-42.0797	-74.1942	30.89	238	0.20	3.3
2004-12-20	14:17:42.71	-43.2948	-74.1217	41.72	289	0.56	2.3
2004-12-20	19:44:36.10	-42.7229	-73.3659	65.50	109	0.18	1.9
2004-12-24	08:44:05.40	-41.0185	-73.6853	17.71	304	0.58	2.2
2004-12-25	08:14:29.02	-41.5993	-73.3106	20.28	251	0.34	1.2
2005-01-01	23:50:24.06	-42.4330	-73.2585	24.02	132	0.10	1.3
2005-01-03	18:11:22.66	-43.1802	-72.7910	1.97	225	0.51	2.3
2005-01-05	03:19:04.80	-43.1723	-72.7684	1.79	236	0.19	2.1
2005-01-08	09:02:07.68	-41.2175	-73.1097	17.49	287	0.97	3.0
2005-01-10	03:36:43.02	-42.4827	-74.2142	27.21	228	0.26	3.6
2005-01-11	05:36:00.58	-42.9152	-75.4168	15.00	314	0.33	2.7
2005-01-13	13:26:35.85	-42.6482	-74.2326	26.43	234	0.27	2.9
2005-01-15	07:05:08.59	-42.7231	-73.3841	64.00	102	0.37	2.3
2005-01-18	21:22:29.19	-42.3806	-72.8002	10.13	099	0.46	2.8
2005-01-19	12:41:21.04	-42.5050	-73.5159	43.63	075	0.78	2.0
2005-01-19	23:29:02.08	-42.4078	-72.7866	27.59	101	0.75	2.1
2005-01-20	07:32:05.68	-40.9583	-73.0455	15.00	302	1.13	2.3
2005-01-20	15:11:31.71	-42.7232	-74.3039	25.58	245	0.28	4.6
2005-01-20	15:23:08.08	-42.7232	-74.3047	24.24	245	0.21	3.4
2005-01-20	16:22:44.45	-42.7308	-74.2699	21.14	261	0.26	2.2
2005-01-20	19:51:47.07	-42.7225	-74.2638	25.17	242	0.29	2.8
2005-01-21	22:13:27.57	-43.2616	-73.0853	8.49	232	1.01	2.9
2005-01-21	23:05:11.04	-43.1815	-73.1246	9.02	242	0.69	2.0
2005-01-22	06:10:15.97	-42.0624	-73.8337	35.43	108	0.41	2.4
2005-01-22	21:58:32.00	-43.3288	-73.0681	10.03	245	0.49	2.3
2005-01-23	21:36:00.44	-42.3908	-72.8174	19.98	110	0.26	1.9
2005-01-24	03:56:16.80	-42.3689	-72.7992	9.09	100	0.22	1.8
2005-01-25	03:01:38.59	-42.9637	-74.3423	18.04	280	0.25	2.4
2005-01-25	19:41:57.33	-42.4541	-74.9463	17.53	310	0.16	2.8
2005-01-27	06:36:40.70	-42.7996	-74.3329	20.42	252	0.29	2.0
2005-01-28	03:29:29.26	-43.1669	-74.3191	14.04	297	0.38	2.1
2005-02-01	08:12:12.36	-42.0401	-72.6024	110.57	194	0.26	1.7
2005-02-03	08:08:57.63	-42.8563	-72.4759	14.39	159	0.19	1.5
2005-02-04	16:42:13.24	-42.3806	-72.7800	19.95	104	0.14	1.9
2005-02-05	08:54:27.86	-41.9032	-73.5756	50.22	199	0.32	1.9
2005-02-08	06:41:39.22	-41.6981	-73.7314	34.36	252	0.52	2.0
2005-02-08	08:57:55.78	-43.1869	-74.4112	15.00	290	0.55	3.3
2005-02-09	05:47:21.60	-42.7280	-74.2860	21.38	269	0.14	1.5

Table continuing on next page ⟿

Table A.4: (continued)

Date	Time	Latitude	Longitude	Depth	GAP	RMS	M_1
2005-02-13	15:57:00.29	-41.1934	-72.9627	17.12	290	1.11	2.4
2005-02-15	05:46:43.98	-42.7246	-74.2770	22.44	090	0.21	1.9
2005-02-17	01:16:26.27	-40.9759	-74.0805	15.00	315	0.13	2.7
2005-02-18	09:11:08.19	-42.0445	-74.2730	19.72	269	0.20	1.7
2005-02-18	09:19:20.04	-41.6861	-72.5926	13.38	291	0.43	1.6
2005-02-20	02:29:26.39	-42.6505	-74.2662	20.20	123	0.16	2.3
2005-02-21	04:16:55.88	-42.6148	-74.2126	26.26	090	0.25	2.5
2005-02-22	06:09:40.63	-42.9318	-74.0266	39.38	232	0.09	1.6
2005-02-25	10:47:52.70	-42.8769	-74.2306	23.53	120	0.18	2.3
2005-02-27	05:20:39.78	-43.0280	-74.3382	20.51	286	0.12	2.0
2005-02-27	08:47:39.23	-42.4197	-73.9029	38.01	090	0.21	3.0
2005-02-27	11:33:30.78	-42.7096	-74.3246	20.81	104	0.18	2.4
2005-02-28	02:05:58.13	-41.5956	-73.4526	19.32	253	0.73	1.8
2005-02-28	18:44:28.28	-41.2949	-73.3656	18.26	282	1.06	2.0
2005-02-28	19:03:35.90	-42.3429	-74.2073	34.28	230	0.16	1.8
2005-03-05	10:41:20.67	-42.4184	-75.4133	19.67	253	0.55	2.8
2005-03-06	15:54:56.02	-42.5201	-72.6385	127.41	217	0.15	2.5
2005-03-08	17:24:22.34	-40.5326	-73.3599	15.00	324	0.22	1.8
2005-03-09	02:07:07.13	-41.8628	-75.1396	15.00	318	0.36	1.7
2005-03-09	03:17:24.24	-42.1170	-75.6467	15.00	284	0.14	2.1
2005-03-10	05:55:49.54	-42.9513	-75.5389	34.03	262	0.51	2.6
2005-03-10	20:29:57.02	-42.7139	-74.2721	23.32	113	0.12	2.6
2005-03-11	05:49:45.99	-43.2721	-74.3589	17.42	208	0.40	2.6
2005-03-11	06:50:39.10	-42.1313	-72.4445	3.89	185	0.25	2.2
2005-03-12	02:05:11.64	-43.0119	-73.6693	42.27	284	0.41	1.7
2005-03-14	03:33:28.22	-41.7822	-74.1066	24.86	253	0.46	2.4
2005-03-16	18:57:42.79	-43.1029	-74.3099	20.89	185	0.27	3.2
2005-03-22	17:39:03.06	-42.7105	-74.2654	25.47	089	0.17	3.7
2005-03-22	17:44:08.95	-42.7220	-74.2950	15.00	272	0.45	1.6
2005-03-23	21:23:31.85	-43.3394	-74.1548	12.51	214	0.30	2.7
2005-03-24	20:45:21.23	-42.1764	-75.3789	19.84	259	0.35	2.9
2005-03-25	01:42:44.74	-43.1934	-74.2860	20.50	198	0.08	2.0
2005-03-25	21:41:45.98	-42.7167	-74.3449	22.20	129	0.14	2.1
2005-03-26	03:11:03.76	-42.1422	-72.3993	0.13	235	0.04	1.4
2005-03-29	06:03:42.95	-43.4658	-74.3114	11.70	303	0.63	2.2
2005-03-30	23:07:20.39	-43.2175	-72.7808	4.61	234	0.65	2.3
2005-03-30	23:18:41.30	-43.1891	-72.7197	16.82	269	0.39	2.0
2005-03-31	00:36:54.69	-43.1924	-72.7222	16.95	234	0.38	2.0
2005-03-31	00:59:36.60	-43.1901	-72.7833	4.94	229	0.41	2.4
2005-03-31	10:18:33.98	-43.2027	-72.7574	9.86	233	0.27	1.8
2005-04-01	08:41:12.60	-43.1904	-72.7780	7.26	229	0.52	2.1
2005-04-02	15:25:53.53	-43.5482	-73.7115	52.56	235	0.87	2.8
2005-04-03	04:40:52.71	-43.2037	-72.7356	15.00	270	0.46	1.5
2005-04-04	08:18:56.21	-43.1959	-72.7542	9.49	232	0.34	2.3
2005-04-04	23:16:24.08	-43.1656	-72.7604	8.35	226	0.57	2.6
2005-04-06	02:09:25.52	-42.6470	-74.2346	24.72	121	0.13	2.7
2005-04-08	07:40:15.93	-42.7968	-74.3325	19.03	277	0.12	1.7
2005-04-09	00:07:21.43	-43.1444	-74.3183	21.10	188	0.24	3.3
2005-04-09	07:16:02.02	-42.7971	-74.3281	17.99	276	0.17	1.7
2005-04-09	07:43:05.05	-42.7981	-74.3378	15.00	277	0.22	1.4
2005-04-10	17:27:44.46	-42.7108	-74.3624	23.13	086	0.15	3.4
2005-04-11	16:03:53.58	-41.8513	-74.0606	21.64	235	0.41	2.6
2005-04-11	17:39:56.67	-43.0781	-74.2904	23.47	220	0.16	2.3
2005-04-12	18:29:23.09	-41.8363	-75.7516	18.38	289	0.46	3.4
2005-04-12	20:34:11.52	-41.7032	-74.1057	15.00	299	0.30	2.5
2005-04-12	22:31:25.80	-43.2025	-72.7433	9.78	234	0.37	2.6

Table continuing on next page ↷

Table A.4: (continued)

Date	Time	Latitude	Longitude	Depth	GAP	RMS	M_l
2005-04-15	01:41:21.05	-41.5033	-74.2905	18.36	312	0.15	2.4
2005-04-17	03:37:57.54	-41.5944	-72.2542	12.40	290	0.77	2.6
2005-04-17	10:27:44.98	-42.7161	-74.2657	24.95	168	0.29	2.0
2005-04-18	07:14:58.03	-42.2338	-74.3282	20.96	180	0.14	1.9
2005-04-18	11:23:05.92	-41.3189	-73.5953	28.85	266	0.49	3.6
2005-04-19	10:00:54.72	-42.6604	-74.2456	25.31	123	0.19	2.3
2005-04-19	18:28:17.58	-41.6563	-74.3511	18.91	306	0.47	2.7
2005-04-21	07:10:43.17	-41.6471	-74.3457	15.00	299	0.91	1.6
2005-04-22	04:46:48.00	-43.1573	-74.1594	33.96	193	0.39	3.0
2005-04-23	05:24:32.41	-41.1825	-73.9507	15.00	304	0.28	2.0
2005-04-23	08:45:33.76	-42.2758	-74.2821	20.22	235	0.14	1.8
2005-04-24	01:20:24.13	-43.5106	-73.6534	49.12	232	0.62	3.1
2005-04-25	22:17:38.50	-42.8726	-73.9788	29.45	111	0.25	2.5
2005-04-26	08:27:12.60	-42.4541	-73.6335	53.73	084	0.18	1.6
2005-04-28	04:04:04.55	-42.7870	-74.4900	15.00	280	0.12	2.0
2005-04-28	15:13:20.64	-43.1312	-74.3520	21.05	184	0.22	2.8
2005-04-29	01:11:24.94	-42.0330	-74.1801	24.35	188	0.24	2.9
2005-04-29	09:00:09.37	-44.0977	-73.3154	15.00	326	1.04	2.7
2005-05-01	10:34:07.85	-42.8396	-72.6306	6.85	133	0.28	2.2
2005-05-06	05:32:26.14	-41.7029	-73.7209	46.62	251	0.24	1.5
2005-05-06	08:08:11.44	-42.4128	-74.4063	28.56	156	0.19	1.9
2005-05-06	13:12:57.45	-42.7113	-73.5090	57.16	076	0.25	2.1
2005-05-08	02:58:24.72	-42.0906	-73.6692	52.06	111	0.18	1.9
2005-05-08	08:01:41.94	-43.3452	-74.2540	11.90	217	0.43	3.1
2005-05-08	10:55:26.46	-41.3259	-73.4283	18.79	298	0.88	2.2
2005-05-08	18:00:42.87	-43.3297	-74.2391	10.77	214	0.34	3.1
2005-05-10	10:21:04.90	-43.7131	-73.2454	13.56	322	0.24	2.6
2005-05-10	11:50:00.51	-42.0686	-73.4717	60.42	141	0.08	2.1
2005-05-13	03:51:14.84	-42.8076	-74.2494	23.36	105	0.20	2.6
2005-05-13	09:08:10.16	-42.9510	-73.6255	55.64	110	0.29	3.0
2005-05-17	23:12:39.80	-41.9078	-73.4414	59.65	199	0.19	2.8
2005-05-18	20:35:09.98	-43.1769	-74.4315	12.86	194	0.27	2.9
2005-05-19	11:44:42.50	-42.8001	-72.5458	6.92	135	0.25	2.7
2005-05-20	21:14:37.32	-41.7479	-74.0862	21.99	296	0.18	3.0
2005-05-20	21:25:06.63	-41.7321	-74.0931	24.58	239	0.28	4.0
2005-05-22	23:01:50.71	-41.9459	-73.1979	68.97	188	0.13	2.5
2005-05-23	04:02:10.80	-42.4613	-74.2653	26.62	114	0.09	2.3
2005-05-23	16:28:27.19	-41.8658	-74.5251	28.56	237	0.28	3.4
2005-05-24	04:49:09.40	-42.4390	-74.2777	23.43	106	0.15	2.7
2005-05-24	06:06:09.72	-42.4500	-74.2597	23.27	104	0.13	2.1
2005-05-24	11:45:17.09	-42.4929	-72.4182	4.25	221	0.56	2.0
2005-05-27	17:46:36.03	-43.1307	-74.3236	19.16	184	0.23	3.1
2005-05-28	13:06:29.60	-42.8522	-73.3964	59.83	132	0.30	2.4
2005-05-29	22:41:41.16	-43.3695	-74.2925	18.70	219	0.34	2.4
2005-05-30	09:24:01.59	-42.7146	-74.3053	22.43	121	0.11	2.0
2005-06-02	12:23:51.53	-41.5033	-75.1631	15.00	339	0.26	2.8
2005-06-09	17:22:37.09	-42.5221	-73.0419	92.74	120	0.01	1.6
2005-06-12	17:17:27.36	-42.6244	-74.2278	24.09	077	0.19	2.8
2005-06-13	01:47:40.57	-42.6281	-74.2175	25.31	092	0.20	3.0
2005-06-16	16:04:46.24	-41.3366	-75.2398	15.00	344	0.35	2.8
2005-06-17	04:48:30.26	-43.0751	-74.2545	19.58	172	0.32	2.4
2005-06-17	08:33:34.38	-42.5100	-74.2490	21.90	093	0.18	2.3
2005-06-18	00:10:55.81	-42.6562	-74.2576	24.54	124	0.16	2.1
2005-06-27	08:19:25.88	-41.8461	-75.5004	15.00	321	0.18	2.9
2005-06-28	19:00:29.37	-43.2786	-73.9851	38.98	217	0.24	2.7
2005-06-30	08:57:13.29	-43.2549	-74.1878	33.40	225	0.02	2.2

Table continuing on next page ↷

Table A.4: (continued)

Date	Time	Latitude	Longitude	Depth	GAP	RMS	M_1
2005-07-01	21:46:21.38	-44.2112	-73.7703	40.00	325	0.66	3.2
2005-07-03	00:25:48.04	-40.7830	-75.2269	15.00	300	0.57	2.8
2005-07-03	12:36:28.01	-42.1749	-72.4090	7.34	230	0.27	2.5
2005-07-04	10:34:34.59	-42.6486	-74.1867	28.41	083	0.16	2.2
2005-07-04	11:10:10.03	-42.8885	-73.7796	45.34	091	0.36	2.5
2005-07-04	16:44:00.13	-42.7725	-74.3310	21.73	097	0.25	2.6
2005-07-06	06:28:32.21	-42.0215	-73.8351	39.31	121	0.26	1.7
2005-07-06	07:12:49.87	-43.2383	-72.7766	9.75	238	0.23	1.8
2005-07-11	00:18:32.35	-42.2310	-75.4442	28.10	263	0.26	2.9
2005-07-11	05:01:09.92	-42.7068	-74.5176	0.19	103	0.61	2.4
2005-07-11	06:25:41.19	-42.7810	-74.3379	22.02	115	0.13	2.6
2005-07-11	09:04:49.81	-42.7761	-74.3466	22.11	191	0.13	1.7
2005-07-11	09:27:54.34	-41.7342	-74.0938	25.91	298	0.18	1.9
2005-07-12	04:02:43.87	-43.2239	-72.8251	9.96	233	0.30	1.8
2005-07-12	04:25:06.23	-43.8186	-74.3359	10.36	260	0.87	3.4
2005-07-12	04:49:26.76	-43.2335	-72.7910	9.81	237	0.43	2.0
2005-07-13	00:45:17.10	-41.6766	-74.1429	19.46	323	0.13	2.4
2005-07-14	01:42:39.70	-42.5009	-74.2566	24.48	146	0.06	1.6
2005-07-14	07:00:43.40	-42.8109	-73.3418	68.19	126	0.10	1.7
2005-07-14	13:36:20.16	-43.7007	-74.2756	15.00	307	0.58	2.8
2005-07-14	17:47:22.96	-41.1127	-73.0102	16.82	304	1.03	2.3
2005-07-15	02:52:09.16	-44.3112	-73.6999	15.00	327	0.11	2.9
2005-07-15	23:34:08.53	-43.8205	-74.2665	18.13	307	1.01	2.5
2005-07-16	04:28:20.90	-43.2668	-74.1747	24.77	217	0.29	2.1
2005-07-16	07:19:30.46	-42.7901	-74.2808	21.54	101	0.18	1.9
2005-07-17	09:46:26.48	-41.8961	-74.3064	29.10	289	0.20	2.1
2005-07-17	16:11:16.92	-42.5925	-74.2298	24.40	111	0.14	2.2
2005-07-18	01:41:01.97	-43.2290	-72.8367	10.07	233	0.25	1.5
2005-07-18	04:55:05.32	-42.6591	-72.5158	37.91	255	0.73	1.4
2005-07-19	01:24:18.56	-43.5175	-74.3040	11.93	319	0.02	1.9
2005-07-21	11:12:09.73	-41.7036	-74.1491	22.84	291	0.17	2.0
2005-07-21	12:11:43.90	-42.4946	-74.2755	23.90	096	0.18	2.6
2005-07-21	18:19:56.29	-42.4937	-74.2751	21.81	106	0.14	2.1
2005-07-21	20:24:29.94	-42.6318	-74.3878	20.64	076	0.27	4.5
2005-07-25	02:55:41.45	-42.0599	-72.4383	7.39	271	0.17	2.0
2005-07-25	12:23:20.54	-41.1079	-73.8838	11.41	290	0.53	3.4
2005-07-26	03:40:00.07	-42.8304	-72.6347	8.39	130	0.29	1.6
2005-07-27	06:54:05.62	-42.8293	-72.6420	8.01	131	0.38	1.9
2005-07-30	17:49:52.89	-42.6239	-74.3780	18.57	077	0.21	3.6
2005-07-31	13:36:52.78	-42.7136	-74.3249	22.11	138	0.11	2.5
2005-08-03	08:35:49.01	-42.4978	-74.2683	22.84	136	0.14	2.4
2005-08-07	11:16:26.19	-41.2224	-73.1653	18.98	299	0.45	2.0
2005-08-07	13:58:35.13	-43.4166	-73.9469	40.70	244	0.27	2.7
2005-08-08	15:21:41.49	-42.6745	-74.4523	15.95	087	0.13	2.6
2005-08-10	01:56:55.52	-43.1816	-72.7935	13.40	265	0.27	2.0
2005-08-10	02:35:08.29	-43.1717	-72.7978	15.00	263	0.33	2.4
2005-08-10	03:41:39.75	-43.1805	-72.7978	12.74	264	0.46	2.3
2005-08-10	05:46:33.49	-43.1750	-72.8068	13.24	264	0.23	1.5
2005-08-10	08:33:14.13	-41.0981	-73.9043	16.24	277	0.49	4.1
2005-08-10	08:36:36.35	-41.1429	-73.7187	16.33	298	0.94	2.2
2005-08-10	09:03:32.18	-41.1060	-74.0038	13.08	309	0.25	2.5
2005-08-10	09:03:33.27	-41.1538	-73.8928	12.84	303	0.42	2.5
2005-08-10	13:40:11.87	-42.6422	-74.2291	24.46	085	0.20	2.6
2005-08-12	17:13:09.71	-43.2079	-72.7147	7.86	237	0.28	2.1
2005-08-13	09:36:27.26	-43.1987	-72.7869	12.71	267	0.41	2.5
2005-08-13	09:39:51.03	-43.1747	-72.7986	8.68	264	0.19	1.9

Table A.4: (continued)

Date	Time	Latitude	Longitude	Depth	GAP	RMS	M_1
2005-08-13	11:06:22.99	-42.2919	-72.7632	35.70	173	0.31	1.6
2005-08-16	10:14:50.07	-42.5795	-74.2116	25.39	108	0.20	2.5
2005-08-18	03:42:19.06	-42.0197	-72.4747	4.99	250	0.28	1.9
2005-08-18	05:17:13.84	-42.0101	-72.4676	6.52	257	0.44	2.1
2005-08-18	08:27:54.11	-42.0088	-72.4632	4.68	259	0.11	1.6
2005-08-18	10:22:10.04	-42.0055	-72.4512	5.51	267	0.27	1.8
2005-08-18	10:23:53.42	-42.0040	-72.4402	6.63	273	0.19	1.8
2005-08-18	18:33:52.40	-42.0048	-72.4387	6.86	262	0.32	3.3
2005-08-18	21:26:36.51	-41.9968	-72.4393	7.43	263	0.44	3.8
2005-08-18	21:28:20.32	-42.0033	-72.4515	5.90	262	0.32	3.1
2005-08-18	21:47:33.63	-42.0145	-72.4585	6.36	261	0.36	2.5
2005-08-19	01:17:02.39	-42.0145	-72.4589	5.56	262	0.29	2.0
2005-08-19	01:38:37.36	-42.2864	-72.4492	7.57	176	0.07	1.6
2005-08-19	02:39:12.55	-42.0250	-72.4725	5.68	251	0.06	1.5
2005-08-19	03:20:15.11	-41.9973	-72.4275	5.43	279	0.33	2.1
2005-08-19	07:33:24.11	-41.9954	-72.4266	5.54	279	0.26	1.8
2005-08-21	08:21:30.07	-43.4271	-74.3717	22.82	251	0.57	2.5
2005-08-21	12:09:24.48	-42.7097	-74.2508	24.67	089	0.17	2.9
2005-08-21	12:51:23.28	-42.7176	-74.2558	24.00	090	0.13	2.3
2005-08-22	04:19:38.03	-42.0066	-72.4630	5.66	260	0.04	1.8
2005-08-22	10:25:16.29	-42.6297	-74.5239	9.65	168	0.39	2.3
2005-08-22	21:29:05.59	-42.0058	-72.4705	6.07	256	0.51	3.1
2005-08-22	22:49:32.80	-42.0364	-74.2039	22.18	252	0.34	2.3
2005-08-23	01:15:21.48	-42.0024	-72.4645	6.11	259	0.44	3.5
2005-08-23	01:50:12.76	-41.9879	-72.4620	5.09	262	0.35	2.2
2005-08-23	03:38:59.95	-42.0271	-72.4780	7.48	246	0.05	1.7
2005-08-23	08:44:18.03	-42.4972	-73.9783	42.53	078	0.25	5.1
2005-08-23	21:54:12.12	-43.0711	-74.0287	31.61	169	0.36	2.5
2005-08-23	22:14:57.56	-42.0114	-72.4661	7.61	258	0.04	1.9
2005-08-24	06:15:59.79	-43.1443	-74.3322	18.41	196	0.18	1.9
2005-08-24	08:33:30.43	-42.0086	-72.4654	5.59	258	0.33	2.0
2005-08-24	14:50:17.84	-43.1846	-74.2912	19.52	197	0.21	2.6
2005-08-24	17:06:41.68	-42.6305	-74.3828	17.51	091	0.25	2.3
2005-08-24	23:10:48.98	-42.9022	-74.2475	20.81	125	0.09	2.2
2005-08-25	10:17:58.13	-42.5425	-74.2396	23.94	106	0.10	2.6
2005-08-25	23:54:53.79	-42.6326	-74.3855	17.23	076	0.17	2.5
2005-08-26	19:15:17.86	-39.4593	-73.2762	15.00	327	0.38	2.9
2005-08-27	07:39:05.17	-42.6520	-73.8446	46.92	200	0.12	2.2
2005-08-28	02:14:37.51	-42.9013	-74.2439	21.61	125	0.16	2.5
2005-08-28	05:22:32.02	-42.8424	-72.6295	5.62	142	0.16	1.7
2005-08-28	18:11:20.58	-40.8998	-75.1285	15.00	296	0.37	3.3
2005-08-29	06:21:30.71	-44.4493	-75.6448	15.00	328	0.76	2.9
2005-08-29	10:22:34.86	-42.7684	-72.5805	7.49	235	0.26	2.8
2005-08-29	10:25:07.78	-42.7788	-72.5663	7.73	241	0.25	2.0
2005-08-30	02:12:09.15	-41.1825	-73.5825	37.35	293	0.52	1.8
2005-08-30	05:37:58.23	-42.5288	-74.2629	23.15	130	0.14	1.8
2005-08-30	23:00:48.85	-41.2801	-73.5642	19.69	276	0.64	3.6
2005-08-31	06:31:10.88	-41.7156	-73.1242	18.45	236	0.47	2.2
2005-08-31	18:00:17.40	-41.1248	-73.8758	13.49	303	0.38	2.6
2005-09-01	05:34:08.69	-42.8704	-72.7268	9.19	156	0.08	1.1
2005-09-01	16:22:53.45	-42.7121	-74.3662	21.91	086	0.25	2.7
2005-09-02	00:37:01.96	-43.1470	-74.2986	18.80	188	0.23	2.4
2005-09-04	09:56:50.82	-44.3254	-73.5373	11.62	324	0.42	2.9
2005-09-04	22:07:44.91	-41.2070	-75.2038	15.00	343	0.85	4.0
2005-09-04	22:07:45.16	-41.1346	-75.0963	15.00	340	0.45	4.0
2005-09-10	17:35:01.47	-42.4346	-74.2921	22.49	109	0.22	2.8

Table continuing on next page ↝

Table A.4: (continued)

Date	Time	Latitude	Longitude	Depth	GAP	RMS	M_1
2005-09-11	14:02:24.27	-42.6212	-74.3815	18.90	077	0.24	2.5
2005-09-12	04:49:22.70	-42.4625	-74.2940	22.72	104	0.29	4.0
2005-09-12	05:27:15.51	-42.4724	-74.3116	15.01	128	0.35	1.4
2005-09-12	07:29:17.28	-42.4772	-74.3014	21.93	126	0.08	1.4
2005-09-12	22:20:31.77	-42.0215	-72.5811	6.64	208	0.36	2.7
2005-09-15	05:34:10.66	-42.7858	-74.3642	17.50	296	0.06	1.4
2005-09-17	04:13:35.68	-43.2115	-74.4767	8.26	305	0.20	1.9
2005-09-18	00:26:54.22	-43.5307	-73.5167	19.19	289	0.80	2.2
2005-09-18	00:33:43.09	-41.8573	-74.1353	41.90	315	0.04	1.8
2005-09-21	05:17:43.37	-42.7466	-73.5111	66.70	189	0.07	1.6
2005-09-23	18:31:28.52	-41.4924	-72.6724	17.54	284	0.43	2.7
2005-09-25	11:15:37.80	-41.1009	-73.1294	15.00	294	1.09	2.5
2005-09-26	12:52:03.87	-42.8397	-72.6185	6.68	132	0.28	2.0
2005-09-26	22:34:08.10	-43.1463	-74.3431	20.57	188	0.26	2.6
2005-09-27	07:37:07.70	-42.5070	-74.2735	21.15	118	0.23	1.8
2005-09-28	11:15:49.15	-43.0346	-74.1512	26.39	161	0.23	3.2
2005-09-29	01:07:59.65	-42.7076	-74.3342	22.56	087	0.21	2.3
2005-10-03	11:02:12.74	-43.2293	-74.2441	22.67	201	0.29	2.3
2005-10-07	08:42:30.31	-42.7806	-74.3276	22.53	250	0.20	2.2
2005-10-08	08:55:25.77	-41.4473	-74.1157	5.46	305	0.24	1.9
2005-10-09	04:41:15.30	-41.9238	-73.4049	62.35	193	0.16	2.1
2005-10-09	05:19:46.76	-42.5116	-74.2724	23.04	234	0.34	2.4

*   *End of Table A.4: List with local events detected by the network.*   *

A.8 Publications

Peer-Reviewed Articles:

LANGE, D., CEMBRANO, J., RIETBROCK, A., HABERLAND, C., DAHM, T., AND BATAILLE, K. (2008). First seismic record for intra-arc strike-slip tectonics along the Liquiñe-Ofqui fault zone at the obliquely convergent plate margin of the southern Andes, Tectonophysics, doi: 10.1016/j.tecto.2008.04.014, in press.

LANGE, D., RIETBROCK, A., HABERLAND, C., BATAILLE, K., DAHM, T., TILMANN, F., AND FLÜH, E. R. (2007). Seismicity and geometry of the south Chilean subduction zone (41.5°S–43.5°S): Implications for controlling parameters. Geophys. Res. Lett., **34**, L06311, doi:10.1029/2006GL029190.

HABERLAND, C., RIETBROCK, A., LANGE, D., BATAILLE, K., AND HOFMANN, S. (2006). Interaction between forearc and oceanic plate at the south-central Chilean margin as seen in local seismic data. Geophys. Res. Lett., **33**, L233023, doi:10.1029/2006GL028189.

Congress Contributions:

LANGE, D., CEMBRANO, J., RIETBROCK, A., HABERLAND, C., DAHM, T., AND BATAILLE, K. (2007). The Southern Chilean Subduction Zone: Local Earthquake Tomography and State of Stress, AGU Fall Meeting 10–14 December 2007, San Francisco/USA, T31A-0268.

LANGE, D., RIETBROCK, A., HABERLAND, C., DAHM, T., BATAILLE, K., AND TIPTEQ RESEARCH GROUP (2007). Seismicity, focal mechanisms, and the state of stress of the Chilean subduction Zone at 42°S, EGU General Assembly 2007, Vienna, Austria, 15–20 April 2007, EGU2007-A-03900.

RIETBROCK, A., HABERLAND, CH., LANGE, D., DAHM, T., LODGE, A., BATAILLE, K., TILMANN, F., FLUEH, E., AND TIPTEQ RESEARCH GROUP (2007). Studying the Seismogenic Coupling Zone with a Passive Seismic Array: The TIPTEQ experiment in Southern Chile EGU General Assembly 2007, Vienna, Austria, 15–20 April 2007, EGU2007-A-06466.

LANGE, D., HABERLAND, C., RIETBROCK, A., DAHM, T., BATAILLE, K., AND TIPTEQ RESEARCH GROUP (2007). Seismicity, focal mechanisms, and the state of stress of the Chilean subduction Zone at 42°S, 67 General Assembly of the DGG, March 2007, Aachen, Germany, Poster: SO 121.

LANGE, D., HABERLAND, C., RIETBROCK, A., BATAILLE, K., AND DAHM, T. (2006). Seismicity and Geometry of the Southern Chilean Subduction Zone Between 41.5°S and 43.5°S (Project TIPTEQ), AGU Fall Meeting 11–15 December, San Francisco/USA.

LANGE, D., HOFMANN, S.D., RIETBROCK, A., HABERLAND, C., BATAILLE, K., DAHM,T., AND TIPTEQ RESEARCH GROUP (2006). The TIPTEQ seismic network covering the Chilean forearc between 41.5°and 43.5°S – Seismicity and velocity model, XI Congreso Geológico Chileno, Antofagasta, 7–11 August 2006.

LANGE, D., HOFMANN, S.D., RIETBROCK, A., HABERLAND, C., BATAILLE, K., AND DAHM, T. (2006). The TIPTEQ seismic network covering the Chilean forearc between 41.5°and 43.5°S – Seismicity and velocity model, EGU General Assembly 2006, Vienna, Austria, 02–07 April 2006, EGU06-A-0732.

HABERLAND, C., RIETBROCK, A., LANGE, D., BATAILLE, K., HOFMANN, S., DAHM, T., SCHERBAUM, F., AND HERMOSILLA, G. (2006). Seismicity and velocity structure in Southern Chile (between 37°and 39°S): First results from the TIPTEQ network, EGU General Assembly 2006, Vienna, Austria, 02–07 April 2006, EGU06-A-06334.

RIETBROCK, A., HABERLAND, CH., DAHM, T., BATAILLE, K., TILMANN, F., FLUEH, E., LANGE, D., AND HOFMANN, S. (2006). The TIPTEQ seismological network in Southern Chile - Studying the Seismogenic Coupling Zone, EGU General Assembly 2006, Vienna, Austria, 02–07 April 2006, EGU06-A-07897.

LANGE, D., HABERLAND, C., RIETBROCK, A., HOFMANN, S.D., BATAILLE, K., AND TIPTEQ RESEARCH GROUP (2006). The TIPTEQ seismic network covering the Chilean forearc between 41.5°and 43.5°S – Seismicity and velocity model, 66. General Assembly of the DGG, 6–9 March 2006, Bremen.

LANGE, D., RIETBROCK, A., HABERLAND, C., BATAILLE, K., HOFMANN, S.D., DAHM, T., AND SCHERBAUM, F. (2005). The Southern TIPTEQ Seismic Network Covering the Chilean Forearc Between 41.5°and 43.5°S – Status, Geotechnologien – Science Report, Continental Margins – Earth's Focal Points of Usage and Hazard Potential, Status Seminar, GFZ Potsdam, Germany, 9–10 June 2005.

LANGE, D., RIETBROCK, A., HABERLAND, C., BATAILLE, K., HOFMANN, S., DAHM, T., TILMANN, F., AND THE TIPTEQ RESEARCH GROUP (2005). The Southern TIPTEQ Seismic Network Covering the Chilean Forearc Between 41.5°and 43.5°S – Status, 19th Colloquium on Latin American Geosciences, GeoForschungsZentrum Potsdam, Germany, April 18–20, 2005.

A.9   Glossary

Table A.5: Abbreviations used in this work

ART	Approximate Ray Tracing
CLVD [%]	Strength of the compensated linear vector dipole
CMT	Centroid-Moment Tensor Catalogue
DC [%]	Strength of the double-couple moment tensor
EDL	Earth Data Logger
FMSI	Focal Mechanism Stress Inversion
GFZ	GeoForschungsZentrum Potsdam
GAP [°]	Largest azimuth range with no observations
ISO [%]	Strength of the isotropic moment tensor
LET	Local earthquake tomography (KISSLING, 1988)
LOFZ	Liquiñe-Ofqui fault zone
LTA/STA	Short-Term Averaging / Long-Term Averaging
MTI	Moment tensor inversion
MOHO	Mohorovičić discontinuity
NEIC	National Earthquake Information Center
OBS	Ocean bottom seismometer
OBH	Ocean bottom hydrophone
RUM	Regionalized Upper Mantle project
SIMULPS	Tomographic inversion programme (THURBER, 1983)
USGS	U.S. Geological Survey
VELEST	Programme for inverting 1-D velocity model
WBZ	Wadati-Benioff zone

Table A.6: Symbols and operators used in this work

A	$[m^2]$	Area of the fault plane
d	[km]	Distance
$\vec{n}$	[m]	Normal vector to the fault plane
m_i	[Nm]	Eigenvalues of the moment tensor
M_l	[dimensionless]	Local Magnitude
M	[dimensionless]	Magnitude
M_w	[dimensionless]	Moment Magnitude
M_0	[dyne * cm] or [Nm]	Seismic moment ($1Nm = 10^7 dyne \cdot cm$)
M_{ij}	[Nm]	Moment tensor element
$\vec{s}$	[m]	Slip vector
t	[s]	Time
u_n	[m]	n^{th} Component of displacement vector
v_p	[km/s]	P-wave velocity
v_s	[km/s]	S-wave velocity
v	[km/s]	Velocity
$\mathbf{x}$	[m]	Coordinate of observation
δ	[°]	Dip of the rupture plane
λ	[°]	Rake of the rupture plane
ξ	[m]	Source coordinate
μ	[Pa]	Shear modulus
ρ	$[kg/m^3]$	Density
τ	[s]	Source time
ϕ	[°]	Strike of the rupture plane
$*$	–	Convolution symbol

Acknowledgments